Dynamic modelling of a stented aortic valve

by

Karl van Aswegen

Thesis presented in partial fulfilment of the requirements for the degree of Master of Science in Mechanical Engineering at Stellenbosch University

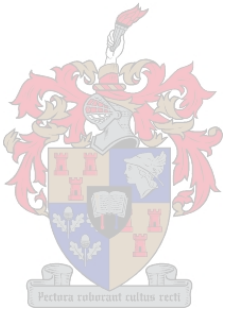

Department of Mechanical and Mechatronic Engineering,
Stellenbosch University,

Supervisors:
Prof. C. Scheffer Prof. A. Groenwold

December 2008

Declaration

By submitting this dissertation electronically, I declare that the entirety of the work contained therein is my own, original work, that I am the owner of the copyright thereof (unless to the extent explicitly stated otherwise) and that I have not previously in its entirety or in part submitted it for obtaining any qualification.

Date: December 2008

Abstract

Dynamic modelling of a stented aortic valve

K.H.J van Aswegen

Department of Mechanical and Mechatronic Engineering,
Stellenbosch University,
Private Bag X1, Matieland, South Africa 7602

Thesis: MScEng (Mech)

December 2008

Aortic valve replacements are frequently performed during heart surgery. However, since this is quite a stressful procedure, many patients are turned down for medical reasons. Stented valves, designed and manufactured for percutaneous insertion, eliminate many of the risks involved in open-heart surgery, thus providing a solution to patients not deemed strong enough for open-chest aortic valve replacements. The aortic valve is a complex structure, and therefore numerical simulation is necessary to obtain flow and stress data to support the design of a prosthetic heart valve in the absence of viable physical measuring methods.

To aid in the design of a prosthetic heart valve, various finite element valve models were created, and the fluid structure interaction (FSI) between the valves and the blood was simulated using commercial finite element software. The effect of the geometry of the leaflets on the haemodynamic behaviour over the cardiac cycle was investigated. It was found that leaflet dimensions should be chosen judiciously, because of their considerable effect on the stress distribution and performance of the valve. A simple leaflet geometry optimisation was done for a 20 mm and 26 mm valve, respectively, by means of existing geometry relationships found in the literature.

Simulations were done to obtain the maximum leaflet attachment forces that can be used by a stent designer for fatigue loading, or to investigate the structural strength of the stent. These simulations were numerically validated. The effect of leaflet thickness and stiffness on resistance to opening, stress distribution and strain were investigated. Results showed that leaflet thickness has a greater effect on the performance of the valve than leaflet stiffness, and thereby validated the results of similar tests contained in the literature. After simulating over-, as well as under-dilation of a stented valve, it was found that problems associated with over-dilation can be minimised to a certain extent by increasing the coaptation[1] region of the leaflets.

A simple pulse duplicator was designed based on a four-element *Windkessel* model. The pulse duplicator was used to study the performance of the prototype valves by means of high-speed photography, the results of which were fed into one of the numerical finite element models and compared to real valve performance. Some of the prototype valves showed efficiencies of 88%.

[1]This is the part of the leaflet that coapts or touches the adjusant leaflet.

Uittreksel

Dinamiese modellering van 'n gestente aorta klep

K.H.J van Aswegen

Departement Meganiese en Megatroniese Ingenieurswese,
Universiteit Stellenbosch,
Privaat Sak X1, Matieland, Suid Afrika 7602

Tesis: MScIng (Meg)

Desember 2008

Aortaklepvervangings word daagliks tydens hartchirugie uitgevoer. Dit is egter 'n baie spanningsvolle operasie, en talle pasiënte word weens mediese redes weggewys. Gestente kleppe wat ontwerp en vervaardig is om perkutaan aangebring te word, skakel die gevare verbonde aan opehartchirurgie uit en bied 'n welkome alternatief vir pasiënte wat te swak bevind word vir oopborskas-aortaklepvervangings. Weens die komplekse struktuur van die aortaklep en by gebrek aan uitvoerbare fisiese metingsmetodes, is numeriese simulasie gebruik om vloei- en spanningsdata te skep om die ontwerp van 'n prostetiese hartklep te ondersteun.

Om met die ontwerp van 'n prostetiese hartklep te help, is verskeie eindige-elementmodelle geskep, en is die vloeistofstruktuurinteraksie (VSI) tussen die kleppe en die bloed met behulp van kommersiële eindige-elementprogrammatuur gesimuleer. Die uitwerking van die grootte en vorm van die klepseile op die hemodinamiese gedrag oor die kardiese siklus is ondersoek. Resultate het getoon dat die grootte en vorm oordeelkundig gekies moet word weens die beduidende uitwerking daarvan op die werking sowel as die spanningsverspreiding van die klep. 'n Eenvoudige klepseiloptimisering is met behulp van

bestaande grootte-en-vormverhoudings in die literatuur vir onderskeidelik ’n 20 mm- en 26 mm-klep uitgevoer.

Simulasies is uitgevoer om die maksimum klepseilaanhegtingskragte te verkry wat ’n stentontwerper kan gebruik om hetsy die vermoeidheidslas of bloot die strukturele sterkte van die stent te toets. Hierdie simulasies is numeries bekragtig. Ondersoeke is gedoen om die uitwerking van klepseildikte en -styfheid op oopmaakweerstand, spanningsverspreiding en stremming te bestudeer. Resultate het getoon dat dikte ’n groter rol as styfheid by klepwerking speel, en het dus die bevindings van soortgelyke toetse in die literatuur bevestig. Oor- en onderdilatasie van die gestente klep is ondersoek, en daar is bevind dat die probleem van oordilatasie in ’n sekere mate beperk kan word deur die sluitingsoppervlakte van die klepseile te vergroot.

’n Eenvoudige hartnabootser is op grond van ’n vierelement-*Windkessel*-model ontwerp en gebou. Die nabootser is gebruik om die werking van prototipekleppe met behulp van hoëspoedfotografie te bestudeer. Datauitdrukke van die nabootser is by een van die numeriese eindige-elementmodelle ingevoer, en met die werking van ’n werklike klep vergelyk. Sommige van die prototipekleppe het ’n doeltreffendheidsyfer van 88% getoon.

Acknowledgements

I would like to express my sincere thanks to the following people and orginisations who have contributed to this project and help make this work possible.

- To my promotors, Prof. Cornie Scheffer and Prof. Albert Groenwold. Thank you for your valuable insets and advice. Thank you for granting me the freedom to use my own ideas and for helping me make this project possible.
- To Dr. Helmuth Weich and Dr. Anton Doubell from Tygerberg hospital. Thank you for giving us the opportunity to be part of this project. Also thank you for funding the project.
- To Anton Esterhuyze and Adriaan Smuts. Thank you for your valuable inputs and thank you for making this a interesting and fun project to do, it has been great working with you guys.
- To Riekert Leibbrandt from Esteq Engineering. Thank you for your valuable inputs and advice with MSC.Dytran.
- To Ferdie Zietsman and the guys in the workshop. Thank you for the manufacturing of the pulse duplicator on such short notice.
- To Danie Els. Thank you for all the help with Latex.
- Thank you to my family for supporting me in my efforts all the way.
- To Tanya and her family, thank you for all your moral support throughout this thesis, it is greatly appreciated.

Contents

List of Figures

List of Tables

Nomenclature

Variables

E	Young's modulus
v	Poison ratio
ρ_l	Density liquid
ρ_f	Density leaflet
μ	Dynamic viscosity
Rb	Radius of the base
Rc	Radius of the commissures
H	Valve height
Hs	Height of the commissures
β	Angle of the open leaflet
θ	Angle of leaflet flexion
Xs	Minimum coaption height
Cc	Coaption height
Ld	Leaflet length in diastole
Ls	Leaflet length in systole
Lf	Leaflet free edge length
P	Pressure
ΔP	Mean pressure difference over the aortic valve
A_{EO}	Effective orifice area
$q_{v_{RMS}}$	Root mean square of the forward flow

Abbreveations

FSI	Fluid structure interaction
CAD	Computer aided design
FEM	Finite element method
FEA	Finite element analysis
FE	Finite element
ISO	International organisation for standardization
RVOT	Rapid valve opening time
RVCT	Rapid valve closing time
ET	Ejection time
AVR	Aortic valve replacement
BLT	Belytschko-Lin-Tsay

Chapter 1

Introduction

1.1 Background and motivation

Aortic valve replacement with cardiopulmonary bypass (CBP) has been the only treatment modality that offers both symptomatic relief and the potential for improved long-term survival. It is thus the treatment of choice for patients with severe symptomatic degenerative aortic stenosis [1].

The aim of this project is to design and model a bioprosthetic aortic heart valve for percutaneous implantation. This project was done in conjunction with two other MScEng projects; one of them focuses on the stent to which the valve is attached [2], and the other focused on a new biomaterial for the valve and the attachment of the valve to the stent [3]. Together, the three projects have the goal to design a stented valve that is suitable for percutaneous implantation in humans.

This thesis focuses on the design and simulation of the aortic valve. Simulation of the valve mechanics is done with the use of multiphysics software, particularly software capable of simulating the fluid structure interaction (FSI) between the valve and the surrounding blood flow. By using multiphysics the structural and fluid domains are modelled simultaneously and the two have a direct effect on each other. These simulations give more insight into the valve behaviour than a purely structural simulation where pressures are applied directly onto the leaflet nodes. A computational fluid dynamic (CFD) simulation, even with a moving fluid mesh, will also not be sufficient because the leaflet motion is unknown prior to the simulation. Another important aspect of this project, apart from using FSI simulations, is simulating the valve

dynamically over time. A transient dynamic analysis will provide more insight into the valve mechanics when compared to a static analysis because actual boundary conditions in the heart changes over time.

Why use simulation during valve design?

"The aortic valve is a complex structure and there is a need for flow and stress data to support the design of a prosthetic heart valve in the absence of viable measurement methods" [4].

The perfect replacement valve would have a structural lifetime that exceeds that of the patient, an intrinsic gradient[1] of 0 mmHg, the haemodynamic profile[2] of the native valve, will carry no infective or thrombotic risk, must be economical, readily available, technically easy to implant and be silent during operation [5].

1.2 Objectives

As mentioned, this study was done in parallel to two other MScEng projects, with the common goal to design a stented valve for percutaneous implantation. Computational simulation of the valve not only helps in facilitating a better understanding of the valve mechanics but it can also minimize expensive design and manufacturing errors by predicting behaviour. This may eliminate costly design iterations.

The outcome of the thesis is to provide a better understanding of aortic valve behaviour with regards to designing a stented valve for percutaneous implantation. Although aortic valve prosthese have been developed by other groups and companies, limited literature is available on the topic. One of the main reasons for this may well be the high costs spent by companies to develop these valves and the patent rights involved.

To aid the other two MScEng projects in the design of the stent and valve, simulations are required to predict stresses that will act on the valve itself, as well as between the valve and the stent. Although similar work and finite element simulation results can be found in the literature, every new design

[1]The intrinsic pressure gradient of the aortic valve is the differential blood pressure across the valve during systole.

[2]The haemodynamic profile of the valve is its functional profile, thus excluding parts of the valve that will not affect functioning.

brings new problems and challenges. Some of the problems, like optimal leaflet geometry, attachment forces and over dilation can be solved with finite element structural and dynamic simulations.

The following objectives were set for this thesis:

- Conduct a literature study on the aortic valve and aortic valve numerical simulation.
- Compare the preferred FSI simulation method to other FSI simulation methods.
- Simulate various valve geometries and critically evaluate the results.
- Investigate the difference between using linear isotropic, non-linear isotropic and non-linear orthotropic material characteristics for finite element simulations.
- Calculate the leaflet attachment forces through finite element simulation.
- Optimise the geometry of a 20 mm and 26 mm diameter valve.
- Investigate over-dilation of a valve and possible solutions.
- Investigate Young's modulus and thickness of leaflets and the effect they have on valve haemodynamics, stress and strain.
- Evaluate the performance of a linear and curved shape leaflet attachment.
- Design and manufacture a simple pulse duplicator based on the 4-element Windkessel model to study the opening and closing behaviour of prototype valves.
- Test a prototype valve intended for implantation into sheep in the pulse duplicator.

Chapter 2

Background and literature review

2.1 Aortic valve replacement

Background and development

Aortic valvular disease is a very common disorder, especially in elderly patients. A study was done by Otto *et al.* [6] in the United States who took echocardiograms of 5621 men and women (65 years and older). Results showed that 70% of the patients had normal valves, 29% had sclerotic[1] valves and 2% had stenotic[2] valves.

It is estimated that approximately 200 000 patients worldwide receive aortic valve replacements annually [7]. In Germany alone, 10 000 patients annually receive an aortic valve replacement [8]. These figures are only an indication of the high demand for aortic valve replacement (AVR), excluding those patients who are turned down for the surgery. An European survey showed that a sizable proportion of patients with severe aortic stenosis may not undergo aortic valve replacement because of constraints related to age and comorbidities [7]. Today, aortic valve replacement is one of the most common open heart surgeries [9].

The first heart valve implantation was done by Hufnagel and Harvey in 1952 [10]. In 1960 Harken [11] performed the first sub-coronary implantation after the development of extra corporal circulation. The problem with these valve replacements were that they all required open heart surgery. Anderson

[1]Sclerotic valves are valves with hardened leaflets sometimes caused by calcification.

[2]Stenotic valves are not capable of fully opening due to fusion of the leaflets at their coaption region.

[12] saw the need for endoluminal implantation and was the first to publish reports of experimental endoluminal[1] heart valve implantation in 1992.

Bonhoeffer *et al.* [13] succeeded to do the first percutaneous implantation of a pulmonary valve into a human in 2000. To date more than 100 patients have been treated by Bonhoeffer and co-workers with only one procedure-related death [9]. In 2002 Cribier [14] followed to perform the first percutaneous implant of an aortic valve in a human.

Anatomy of the natural aortic valve

The heart consists of four chambers, each with its own valve. The aortic valve is situated in the descending aorta where it connects to the left ventricle. During systole, blood from the left ventricle is pumped through the aortic valve and during diastole, the valve closes and restricts blood in the aorta from entering the left ventricle. Figure 2.1 [15] shows where the aortic valve is situated in the heart. The figure also shows the mitral valve and coronary arteries. Both of these put a restriction on the percutaneous valve design because the valve is not allowed to restrict blood from entering the coronary artery and it should also not influence the functioning of the mitral valve.

A diagram of the normal aortic valve is shown in Figure 2.2 [16]. The valve consists of three leaflets (cusps) and is also called a tri-axial valve. An abnormal valve with just two cusps is sometimes found in patients. These valves are called bi-axial valves. The valve basically works as a check valve with minimal resistance to opening and closing.

The pressures in the left ventricle and aorta over the cardiac cycle are shown in Figure 2.3 [17]. An increase of pressure in the ventricle causes blood to flow into the aorta, thus opening the valve. This happens as soon as the ventricular pressure becomes more than the aortic pressure. During systole there is a difference between ventricular pressure and aortic pressure, this difference is known as the pressure drop over the valve. An increase in valve resistance causes an increase in the pressure drop. When the pressure in the ventricle drops below the pressure in the aorta, blood flows back into the ventricle causing the valve to close.

[1] Endoluminal procedures are minimally invasive and are carried out through arteries or veins in the body.

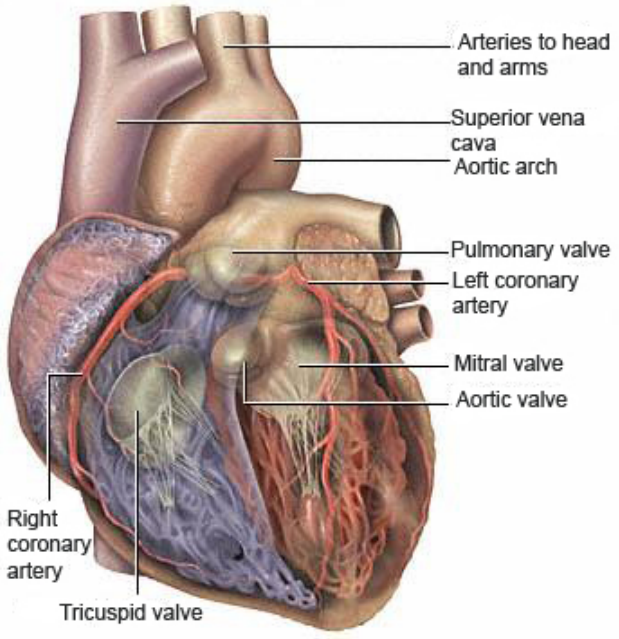

Figure 2.1: Section through a heart [15]

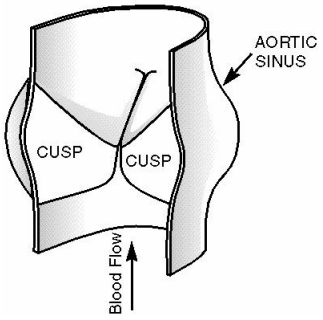

Figure 2.2: Aortic valve [16]

The cusp or leaflet geometry is shown in Figure 2.4 [18]. The free edge is the part of the cusp that flaps around during the opening and closing phase, the part of the free edge that touches the other cusps during closure is called the coaptation area. The curved part where the cusp connects to the aortic wall is called the commissure. The commissure ensures that the leaflets close tightly during diastole, preventing any leakage of blood into the ventricle. The corpus aranti is a mass in the coaptation region believed to help with valve closure. The two main structural layers of the cusp are called the fibrosa and

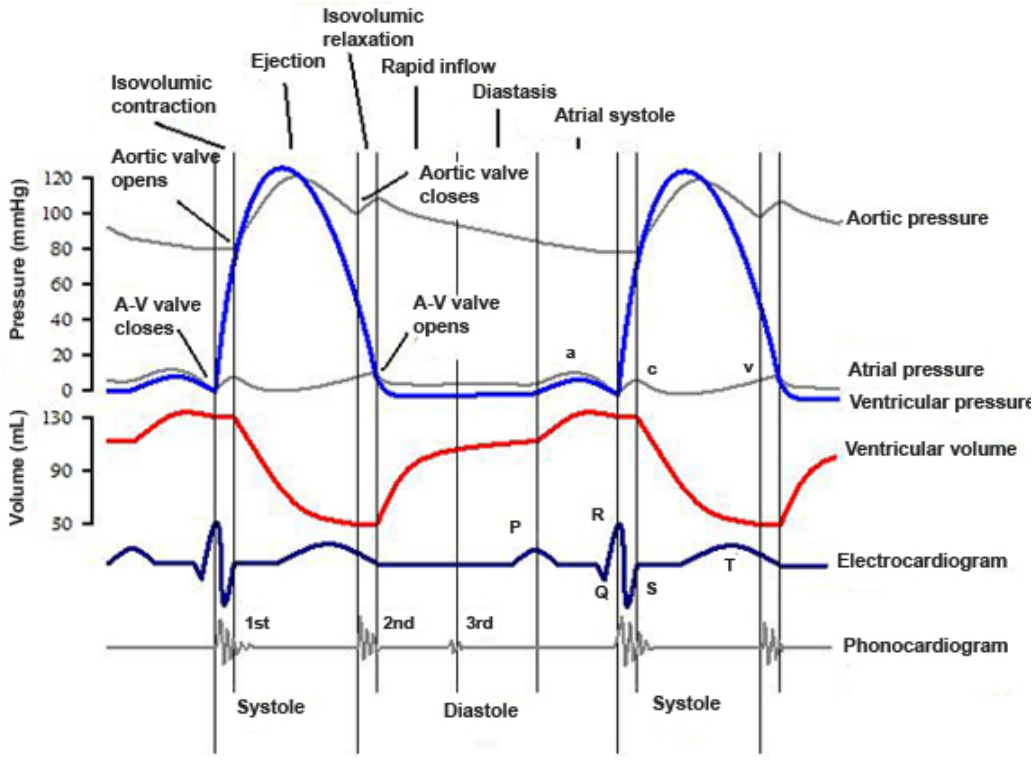

Figure 2.3: Cardiac cycle [17]

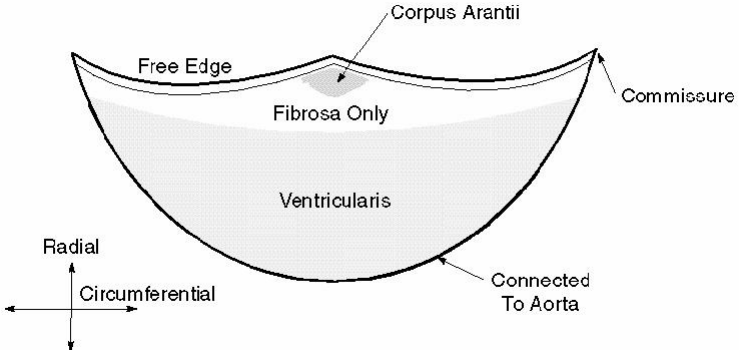

Figure 2.4: Leaflet [18]

the ventricularis.

Figure 2.5 [19] shows the cross-section of a cusp. The thickness of the cusp is between 300-700 μm. The main structural layer in the cross-section is the fibrosa. It is made from Collagen and takes up approximately 45% of the cross-section.

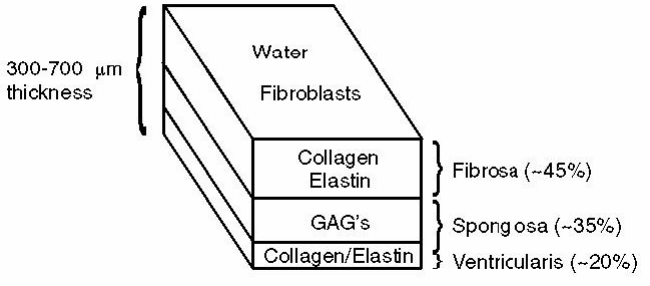

Figure 2.5: Leaflet section [19]

Replacement heart valves

Replacement heart valves can be divided into tissue and mechanical valves. Tissue or bioprosthetic valves can then be divided into autografts, homografts and xenografts. Autografts are made from a patient's own pulmonary valve which is then used to replace the aortic valve. Homografts are valves that are harvested from donor hearts and then preserved. Xenografts are valves made from chemically treated animal tissue, usually bovine or porcine.

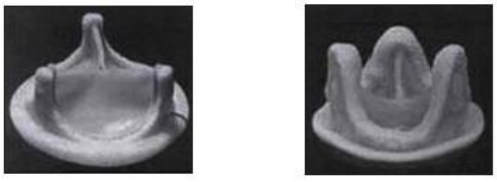

(a) Homograft (b) Xenograft

Figure 2.6: Bioprosthetic valves [5]

50 - 55% of valves used annually for implantation consist of mechanical valves, the rest are made from tissue [20]. The performances of these valves are measured by their ability to minimize the obstruction of blood flow as well as their durability.

Many different designs of mechanical valves are found on the market and all of them have certain advantages and disadvantages. As the name suggests, mechanical valves make use of mechanical interactions and are usually manufactured from some kind of metal. Tissue valves mimic the movement of the

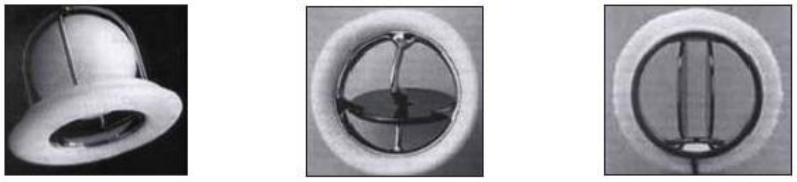

(a) Ball and Cage (b) Tilting-Disk (c) Bi-Leaflet

Figure 2.7: Mechanical valves [5]

native aorta more closely than the mechanical valves and they operate silently compared to mechanical valves that are sometimes associated with a ticking noise. Figure 2.6 shows examples of bioprosthetic valves and Figure 2.7 shows examples of selected mechanical valves [5].

Bioprosthetic valves can also be grown from cells, this method is however still in the early stages of development.

Although the above mentioned valves have proved to work effectively in patients that underwent aortic valve replacement, the procedures all require open heart surgery.

2.2 Percutaneous implantation

Background

Early experiments with percutaneous pulmonary valve replacement proved that the concept of implanting a valve with the use of a catheter is feasible [21; 22].

Percutaneous implantation involves the insertion of the valve through the femoral artery. Figure 2.8 [23] shows an example of percutaneous stent deployment. The procedure involves the insertion of a guide wire through the aortic arch into the left ventricle. After the wire has been inserted, a catheter with a crimped balloon is slid over the guide wire and the balloon is then used to dilate the native valve (A), the balloon is then deflated and removed. A stented valve crimped over a balloon on the end of the catheter is then slid over the guide wire (B). When the valve is in position the balloon inflates pushing the stent into position (C), after which the balloon deflates and the catheter

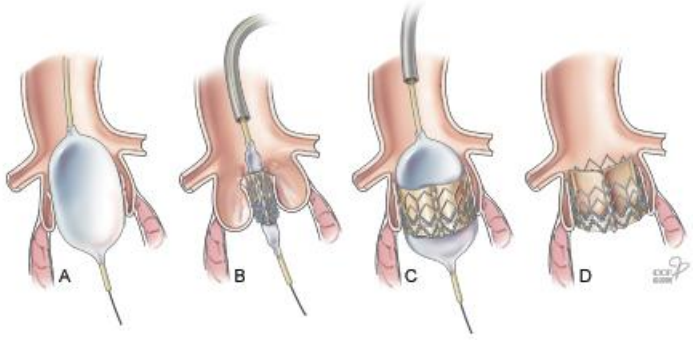

Figure 2.8: Percutaneous stent deployment [23]

is pulled out, leaving the new valve intact.

Another method to implant the stented valve is through the apex of the heart. This route will be followed when the patient's femoral artery is too narrow for the delivery system. A small incision is made through the apex of the heart and the catheter with the crimped valve is pushed into position. The balloon inflates and the new valve is fixed into position. This method has been proved to be successful in animal studies [12; 24], as well as human studies [25].

Figure 2.9: Corevalve prosthesis [26]

Figure 2.10: Edwards prosthesis [27]

There are two types of stented valves used for percutaneous implantation. The first type is a self-expanding Nitinol stent made by CoreValve [26] and the other one is the more traditional Edwards SAPIEN Transcatheter heart valve made by Edwards Lifesciences [27]. These valves are shown in Figures

2.9 and 2.10. Nitinol is a shape memory alloy, thus the stent is manufactured to maintain a certain shape. For insertion the Nitinol stent is crimped similar to the normal stent but a catheter sheath is fixed around the stent. When the stent is in the correct position the sheath is pulled back and the stent expands to its original shape without the help of a balloon. The Edwards valve is inserted the more "traditional" way, as shown in Figure 2.8.

2.3 Numerical simulation

Previous studies

Stress concentrations are thought to be one of the main reasons responsible for valve degradation [28] and tissue calcification tends to initiate at areas of high stress. These calcified sections weaken the valve, causing it to tear or form holes at the calcified areas, leaving a malfunctioning valve. Finite element simulation can be used to identify areas of high stresses. Research involving finite element simulation of the aortic valve has been going on for some time. The first models that were developed were called dry models. These models were simulated ignoring the interaction of the blood, and pressures were applied directly to the structure.

The problem with applying pressures directly onto the leaflets is that the actual pressures are non-uniform and in dry simulations the applied pressures are normally uniform. This becomes clear when simulating the FSI of the valve. Although uniform pressure boundaries might be applied to the fluid, the pressure that the fluid exerts on the leaflets vary with leaflet position. These pressure differences are relatively small from one area of the leaflet to another, but due to the nature of the material, small pressures have a great influence on opening and closing of the valve. The opening and closing of the valve involves a strong interaction between the blood and the valve [20].

Modelling the FSI in the valve is much more complicated than the dry model simulations, mostly due to the large non-linear deformation of the structure (leaflets) through the fluid (blood) domain and the coupling between the two. Several attempts to simulate the valve behaviour with the use of FSI methods have been conducted successfully. De Hart [20] has been successful in doing a detailed three-dimensional analysis of the valve kinematics, mechanics

and fluid dynamics during the systolic phase.

In 2005 van Loon [29] also achieved success in simulating the FSI in the aortic valve.

In 2003 Carmody *et al.* [4] used the explicit solver LS-DYNA to simulate aortic valve behaviour. The goal was to simulate the aortic valve using loading conditions from the simulation of the left ventricular outflow tract. This was achieved by simulating the contraction and expansion of the left ventricle and using the flow data as a boundary condition for the aortic valve simulation. In 2006 Ranga *et al.* [30] also simulated the FSI in the aortic valve using LS-DYNA. The goal of the research done by Ranga was to evaluate two different valve-sparing reconstructions on valve dynamics and haemodynamics.

De Hart *et al.* [31] simulated the effect that reinforcement fibres in the leaflets of stented valves have on the stress in the leaflet. The results showed that in peak stress areas of the leaflets, up to 60% of the principal stresses are taken up by the fibres. In some cases a more homogeneous stress distribution was also obtained. Cacciola *et al.* [32] showed that a stress reduction of up to 70% is possible in stentless valves because of fibre reinforcements.

Software

As mentioned in the previous section, explicit methods have proved to be successful in dealing with the large deformation of the aortic leaflets through the Euler domain. Although implicit methods have also proved successful, commercial FSI packages tend to use explicit formulations. Advantages of explicit methods over implicit methods are that explicit methods do not require inversion of the global stiffness matrix which takes up a lot of computational time [33]. Explicit methods however typically have a time-step that is a 1000 times smaller than implicit time steps.

For the task of finding a suitable multiphysics software package, many commercial software packages were considered. The two main competitors are LS-DYNA and MSC.Dytran. Both of these are explicit solvers which are capable of dealing with FSI problems. Although LS-DYNA proved to successfully simulate the aortic valve on a few occasions, MSC.Dytran was chosen. The main reason for this was because the University of Stellenbosch already uses various MSC products (including the pre-processor for MSC.Dytran, MSC.Patran). It was also easier to obtain technical support from MSC.Software.

It is however important to note that MSC.Dytran (like Ls-Dyna) does not support a turbulence model (it does however support viscosity) for modelling fluid, instead it assumes laminar flow. This is not unrealistic since blood flow remains largely laminar at all physiologically normal flow rates. Only when a valve exhibits malfunctioning, some turbulence might be expected [20]. A typical physiological value for Reynolds number is about 4500 [4].

As the goal of most of the simulations are to study valve behaviour through FSI simulation it was thought that a laminar flow model would be sufficient because the dominant forces in leaflet deformations are the pressure and momentum from the fluid. This assumption is supported by many authors including De Hart [20] and Carmody *et al.* [4]. The use of a laminar model also decreases the computational time of a simulation.

Introduction to FSI

FSI can best be modelled when the fluid is described within an Eulerian reference frame, whereas the structure is described within a Lagrange reference frame. This basically means the Euler material (fluid elements) moves through its computational frame while the structure's computational frame moves with the structure [20].

Lagrangian solver

With the Lagrangian solver grid points are fixed to the locations on the structure. These points move with the structure as it deforms, thus changing the boundary conditions of the Eulerian solver. Figure 2.11 [34] shows an example of a structural grid moving with a structure. The solid and dashed grid lines indicate the structure position before and after deformation respectively.

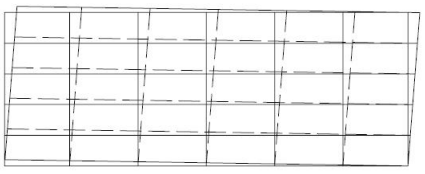

Figure 2.11: Lagrange grid points [34]

Eulerian solver

The grid points of the Eulerian domain are fixed in space and the elements are simply partitions of the space [35]. The material moves through the Eulerian mesh and the Eulerian solver calculates the mass, momentum and energy as it moves from one element to the next.

The two domains are then coupled at the structure surface. The surface acts as a boundary condition for the Euler domain, where the Euler material in turn exerts stresses onto the coupled surface.

There are various techniques to deal with FSI problems. The fluid and structure equations can be solved uncoupled, weakly coupled or coupled [29]. Other popular methods include boundary fitting methods like the arbitrary Lagrange Euler (ALE) method. Although ALE methods have proved to be accurate for large structural deformation, it is a very difficult method to implement on complex 3D geometries such as an aortic valve, because the fluid and structural grid points must coincide.

Chapter 3

FSI method comparison

3.1 Introduction

Early on in the project it was decided to use commercial software for the FSI simulations, rather than developing a customised code. Due to time constraints the development of a customised code would have taken up valuable time required for heart valve simulations. The use of commercial software has the disadvantage that one is limited to what the software is capable of. It however has the major advantage that it can be used from the onset and it has been proved to work adequately for many applications.

MSC.Dytran 2007r1 was used in all the FSI simulations. It is part of MSC.Software's range of finite element packages. MSC.Dytran supports shared memory parallel processing, which means that multiple CPUs on one machine can be used to speed up the simulation, but it does not support distributed parallel processing, where a cluster of machines are used. Most of the FSI simulations where run on a Dell Precision 690 workstation with eight CPUs and 8 Gb RAM using Open Suse Linux 10.3 as the operating system. Because of the time it takes for a simulation to finish (sometimes as long as 8 days), the stability of Linux was preferred over Windows. One reason for the simulations taking so long (even though parallel processing was used) is because MSC.Dytran 2007r1 does not support parallel processing of the fluid elements which make up the majority of the elements in a model.

MSC.Dytran is mostly used for airbag analysis and to simulate rapid deformations such as automobile crashes. In South Africa it is used in the defence industry e.g., simulating land mine explosions on the undercarriages of

armoured vehicles [36]. There is however a big list of applications. No publications could be found where MSC.Dytran was used to simulate a heart valve.

The aim of this chapter is to compare the FSI methods available in MSC.Dytran through the use of a simple example as well as to explain the principles of how they are implemented. Because of the difficulty experienced in obtaining an example problem with clear boundary conditions and results that would be easy to set up as well as reflect conditions similar to that in the aortic valve, an example problem had to be created.

3.2 Test problem formulation

MSC.Dytran 2007r1 supports three FSI methods, the first being the arbitrary Lagrange Euler (ALE) method, a general coupling method and a fast coupling method. This section compares the ALE method to the fast coupling method to find the most suitable method for simulating a heart valve. Because the fast coupling and general coupling are very similar, only the fast coupling method will be illustrated. The general and fast coupling methods differ slightly in the way the fluid mesh is described.

The ALE method is totally different from the general and fast coupling methods.

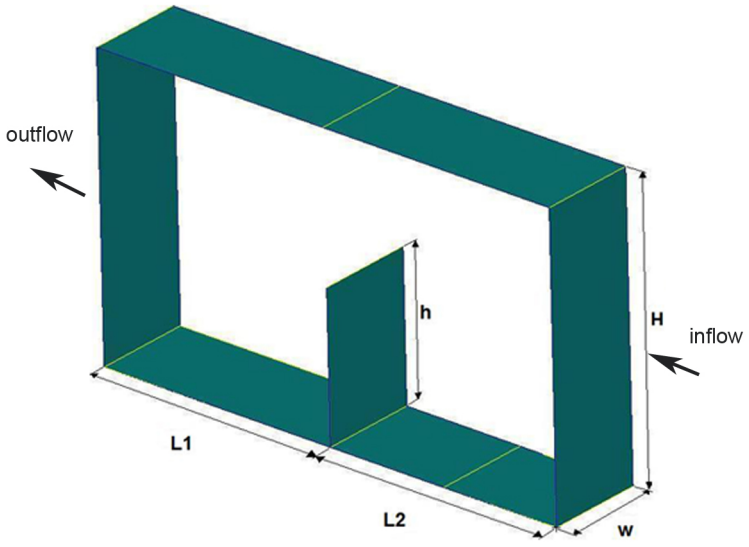

Figure 3.1: FSI problem

The model chosen for the comparison is shown in Figure 3.1 and the simulation parameters are shown in Table 3.1. The material parameters, including the linear elastic material model, are in a similar range of values to that of an aortic valve decribed by many authors including Thubrikar [37]. The model consists of a thin plate structure immerged in a fluid. The movement of the fluid causes the plate to deform much like the aortic leaflets.

Table 3.1: Problem parameters

E [N/m^2]	$10 \cdot 10^6$	w [mm]	20
ν[−]	0.35	h [mm]	30
ρ_l [kg/m^3]	$1 \cdot 10^3$	H [mm]	60
t_l [mm]	0.5	$L1$ [mm]	50
ρ_f [kg/m^3]	$1 \cdot 10^3$	$L2$ [mm]	50

The same boundary conditions were used for both the ALE and general coupling method. The pressure shown in Figure 3.2 was applied to the input while the output pressure was set to 10 kPa. Although it is not wrong, it was preferred to not work with zero boundary values, therefore the 10 kPa was added to the iput and output boundaries resulting in the figure as shown.

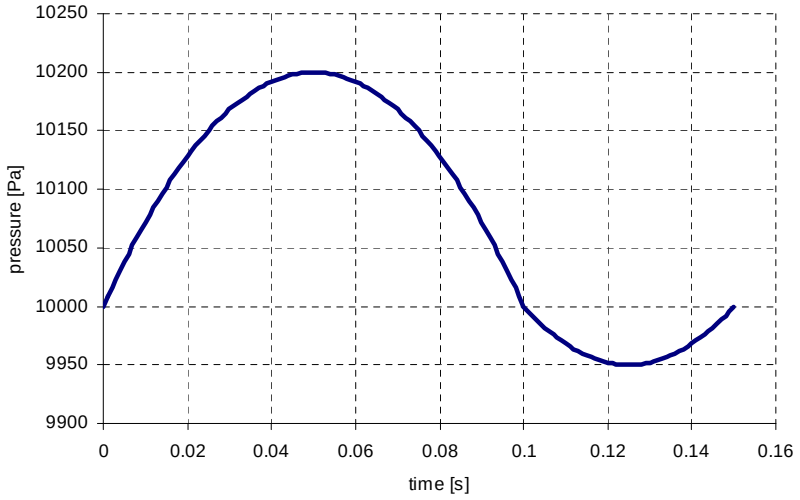

Figure 3.2: Input pressure

When only two pressure boundaries are used instead of the preferred flow boundary at the inlet and a pressure boundary at the outlet, Dytran requires an additional density input. The density values are calculated from the pressure input values with Equation 3.1, where P is the pressure at a specific time, a_1 is the bulk modulus of the fluid, $\rho_{(0)}$ is the reference density and $\rho_{(i)}$ is the input density.

$$P_{(i)} = a_1 \cdot \left(\frac{\rho_{(i)}}{\rho_{(0)}} - 1 \right) \tag{3.1}$$

3.3 ALE method

In ALE coupling the structure and fluid nodes must initially have the exact same coordinates at the coupling surface, in other words, the two meshes must have conformity. As the structure deforms under the pressure load from the fluid, the coupling nodes of the fluid moves along and the mesh is updated.

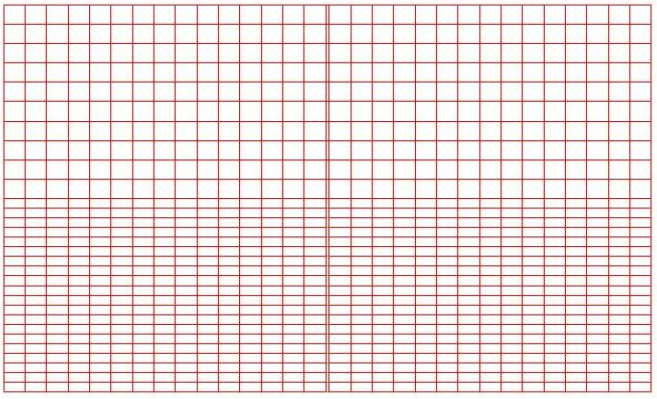

Figure 3.3: ALE mesh deformation: time = 0 s

Figures 3.3 and 3.4 show the ALE mesh at time 0 and time 0.15 seconds. For the given example ALE is easy to incorporate, but it will only work if the structure consists of solid elements. ALE coupling is possible with shell elements (for example in a bird strike analysis [34]) but in this case fluid coupling is necessary on both sides of the plate. The disadvantage of ALE coupling is that the fluid mesh gets distorted [38], as shown in Figure 3.4. As the structure geometry becomes more complicated (as in the case of a heart

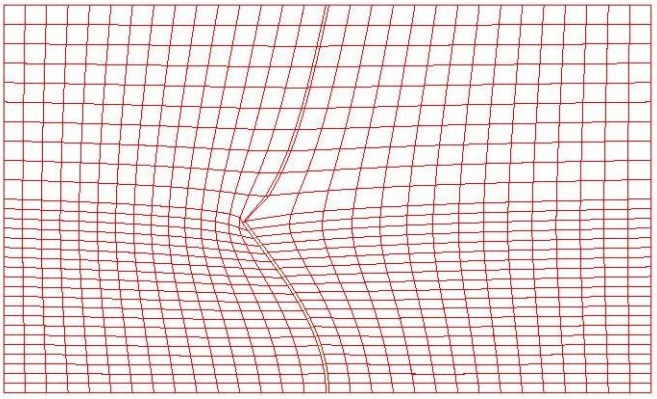

Figure 3.4: ALE mesh deformation: time = 0.15 s

valve), the difficulty of meshing the fluid so that the coupling nodes share the same coordinates also increases. Figure 3.5 shows the fluid vectors at time 0.15 seconds. Because the vectors are shown at time = 0.15 seconds, the fluid starts to reverse as can be seen on the right hand boundary.

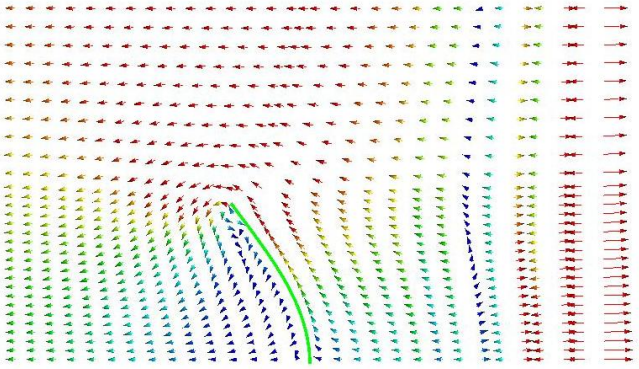

Figure 3.5: ALE velocity vectors

3.4 Fast coupling method

The fast coupling method is basically the same as the general coupling method. Both these methods make use of non-boundary-fitting algorithms to couple the structure to the fluid. This means that unlike the ALE method where conformity between the fluid and structure mesh is required, the fluid and

structure elements intersect each other. Figure 3.6 shows an example of a non-boundary fitting mesh. In the example the fluid elements are specified to lie within a box. The structure elements intersect the fluid elements inside the box. Where the intersection takes place the fluid elements are cut by the structure. The "white" part of the fluid elements are ignored for the particular time step but as the structure deforms the active fluid elements (grey elements) get updated.

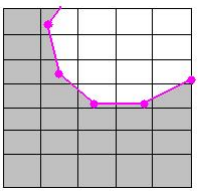

Figure 3.6: Non-boundary-fitting mesh

Both the general and fast coupling methods make use of closed coupling surfaces which must result in a positive volume. In other words, when a structure is coupled to a fluid, the structure must be a closed volume. Because of this closed volume method it is sometimes necessary to add dummy porous elements to the desired coupling surface in order to create a closed volume. For example: Figure 3.7 shows closed volume 1 (rigid b + dummy b + dummy porous + deformable) and volume 2 (dummy porous + dummy a + rigid a + deformable).

The green and black tri-elements are dummy elements which help to form the closed volumes. As they are needed to move along with the structure (deforming plate), the dummy element nodes must be connected to the plate. Except for the moving structure and the dummy elements, the rest of the closed coupling surface is made out of rigid elements; once again the rigid elements are only there to help form the closed volume, they are of no further interest. Rigid elements are used instead of normal elements to reduce the computational effort.

When using the fast coupling method, the fluid elements must be hexahedral and their local coordinates must be aligned with the global coordinate system axis. The fast coupling method makes use of this knowledge to in-

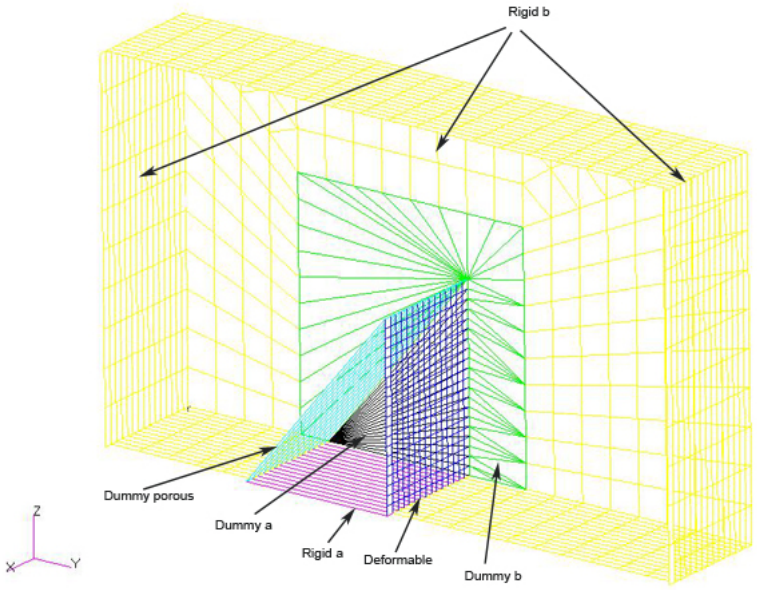

Figure 3.7: Closed volumes

crease the speed of calculations. The general coupling method can use any solid element.

Figure 3.8 shows how the closed surface construction can be implemented to construct a valve for FSI simulation.

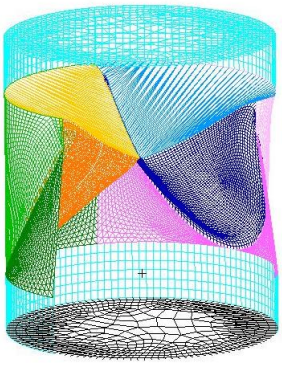

Figure 3.8: Closed volume implementation

Figure 3.9 shows the deformation of the two closed surfaces at time 0.15 seconds. The deformation was caused by the actual plate structure that de-

formed under the pressure load from the fluid. The parts of the closed volume that deformed with the plate are all dummy elements. This figure also illustrates how the closed volume deforms while with the ALE method it was the fluid mesh that deformed as it is the only "structure" in the ALE analysis. With the fast coupling method and with the general coupling method very large non-linear deformations are possible. The elements that get distorted are the dummy structure elements which are of no interest. In this case the only elements of interest are the plate and the fluid elements.

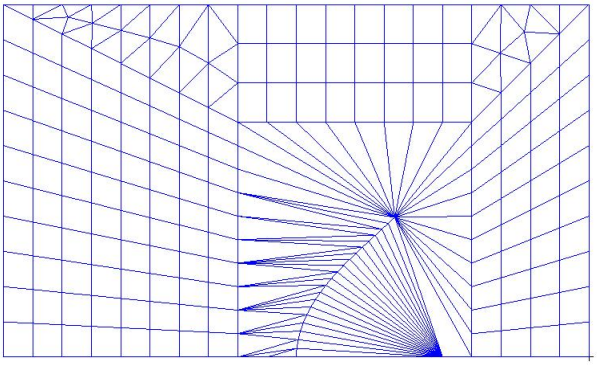

Figure 3.9: Box deformation for fast coupling method

Figure 3.10 shows the velocity vectors obtained from the fast coupling method. As with the ALE vectors, here they are shown at time = 0.15 seconds that is why the fluid direction is starting to reverse on the right hand boundary. By using 3D imaging the thin shell is clearly visible. The velocity vectors are comparable to the ones from the ALE solution.

3.5 Results

Figure 3.11 shows the deformation of the ALE method (solid red elements) and the fast coupling method (shell elements depicted by the black line).

Figures 3.12 and 3.13 show the displacement of a node at the top of the plate for both the ALE and fast coupling simulations. The X-displacements are 14.5 mm and 16 mm for the ALE and fast coupling methods respectively. The Z-displacements are 4.4 mm and 5.2 mm for the ALE and fast coupling methods respectively.

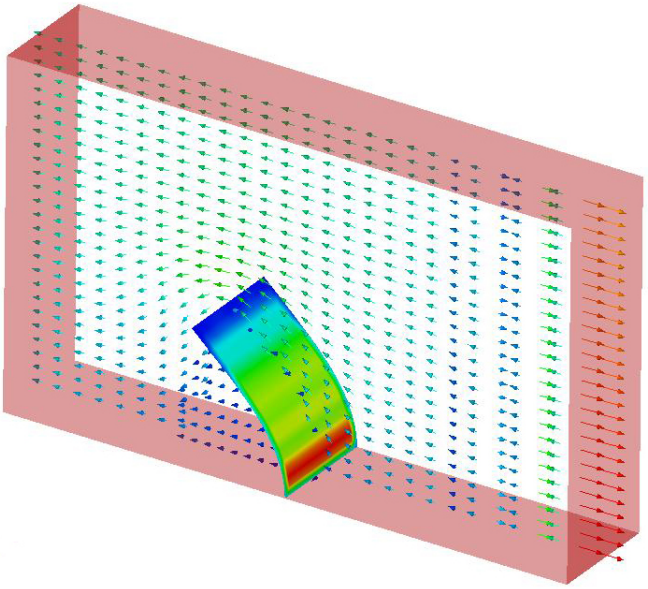

Figure 3.10: Velocity vectors for the fast coupling method

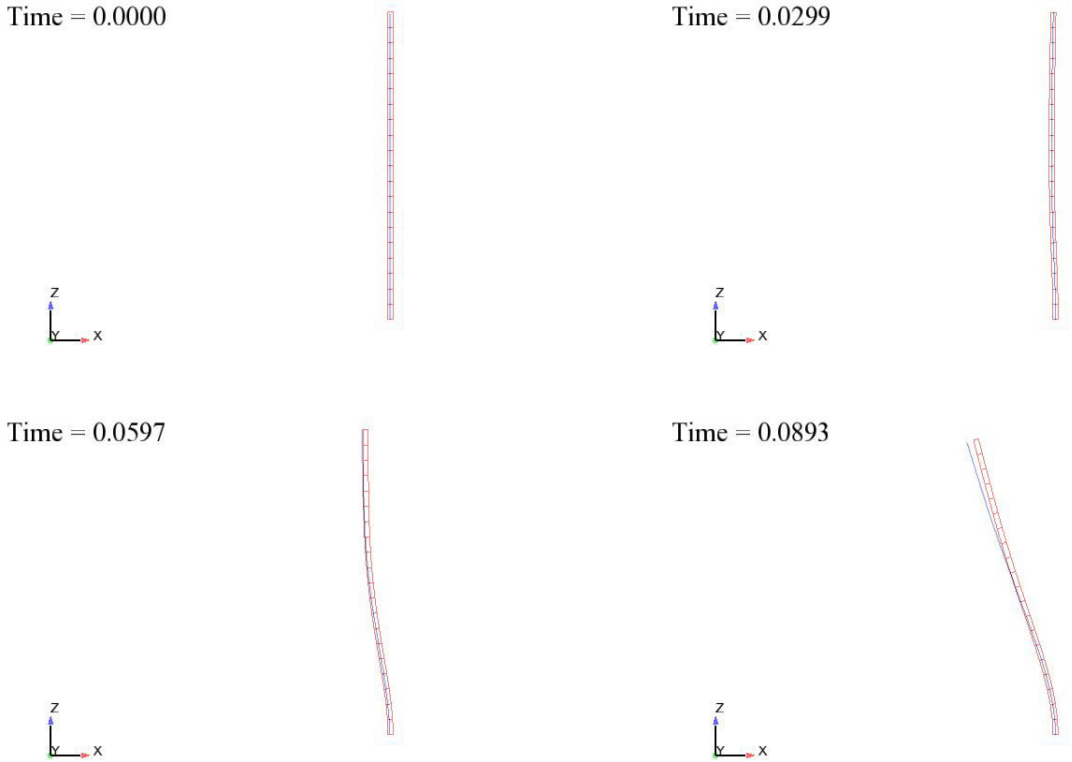

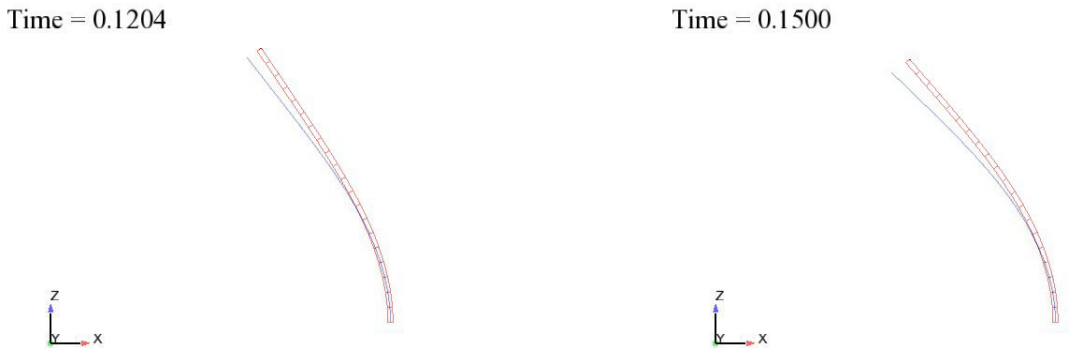

Figure 3.11: Plate deformation

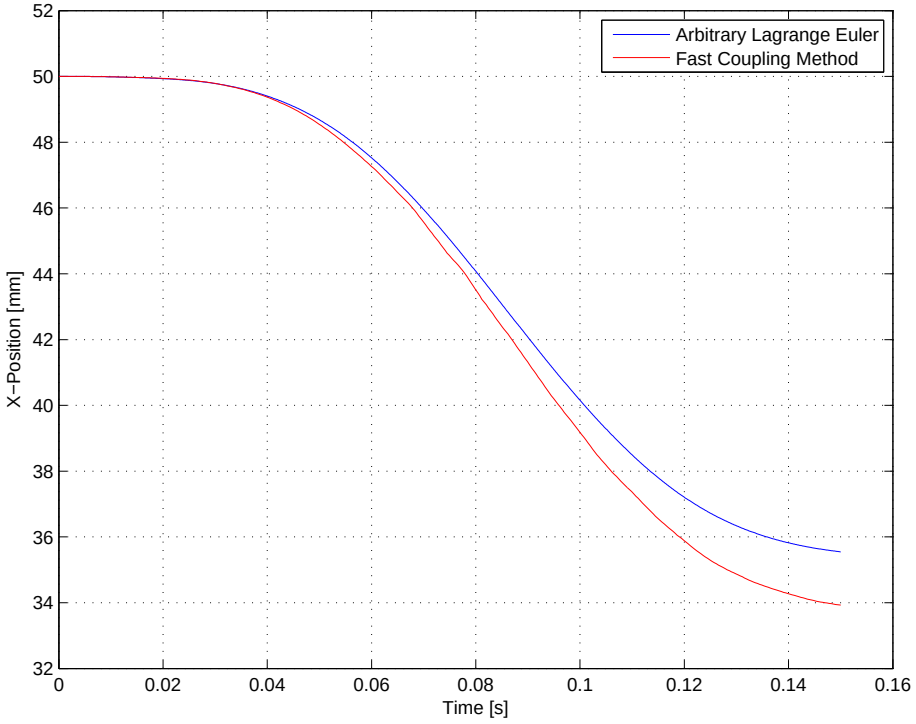

Figure 3.12: X-displacement

The difference between the two simulations might be attributed to the different element types being used, one being shells and the other solids. The size of the fluid elements play a significant role (as investigated in Appendix C) and the coarseness of these elements for both the simulations will certainly influence results. Another factor influencing the results is the distortion of the fluid elements that takes place in the ALE method, as shown in Figure 3.4.

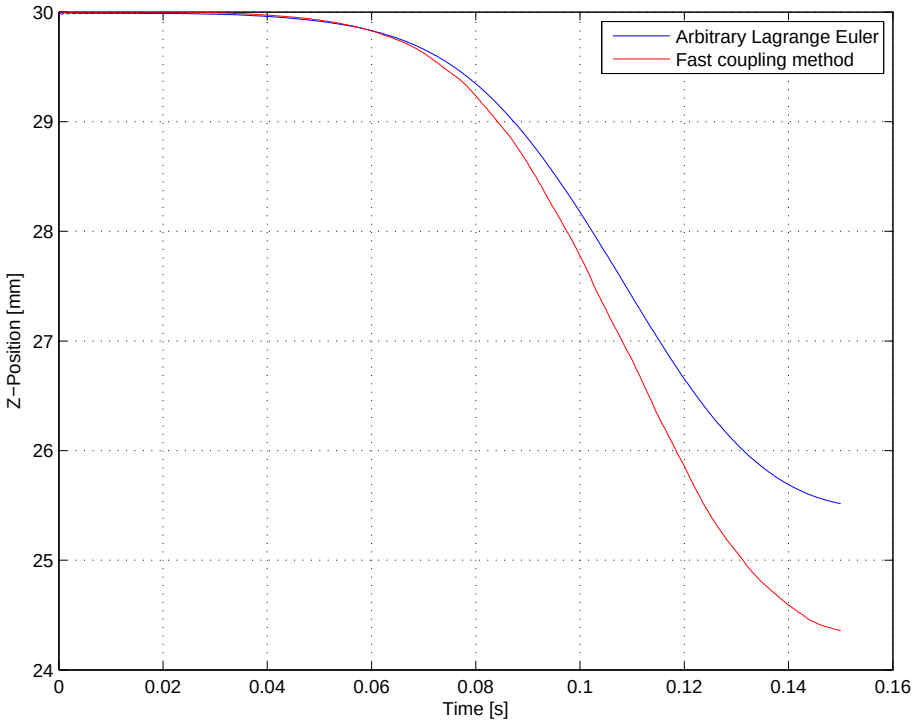

Figure 3.13: Z-displacement

Because the software automatically changes the step factor, time step might also play a role in the difference between results.

3.6 Conclusion

This chapter studied two of the coupling methods available in MSC.Dytran. It was found that the fast coupling method is more appropriate for heart valve simulation. This conclusion was made on the basis that implementation would be much easier due to the non-boundary fitting algorithm used by the Euler solver and the fact that shell elements can be used. Large non-linear structural deformation is also possible without the structure distorting the fluid mesh. The fact that the fluid and structure nodes must coincide at the coupling surface when using the ALE method makes the implementation of this method very difficult due to the complex geometry of the aortic valve.

Chapter 4

Analysis of different aortic valve models

4.1 Introduction

This chapter compares four different aortic valve designs. The results of the simulations are compared with each other and to results found in the literature. The aim was to obtain a better understanding of the functioning of a valve with respect to its geometrical properties. Due to the complex geometry of an aortic valve, the research was firstly aimed at determining the importance of geometric ratios, and secondly to evaluate valve functioning when these ratios are not chosen judiciously. The heart and valves are part of a complex system where the different parts of the system have a direct influence on each others performance. For example, flow boundaries would differ from heart to heart or valve to valve, this would however be impossible to incorporate into a simulation. Therefore boundaries were chosen to reflect the average heart conditions. All of the valves were simulated with MSC.Dytran, taking into account the FSI between the blood and the valve. Post-processing was done with CEI.Ensight. The following will be discussed for each valve:

- The opening and closing characteristics
- Leaflet and attachment stresses during systole and diastole
- Regurgitant volumes
- Effective orifice area

4.2 Modelling

The material parameters i.e. $E, \nu, \rho_l, t_l, \rho_f, \mu$ that were used in the simulations are tabulated in Table 4.1. The value for Young's modulus from the literature was found to vary between 2 MPa [39] and 15 MPa [40] when simulating the material as linear isotropic, therefore it was thought that an appropriate value would be 5 MPa. The Poison ratio (ν), density (ρ_l) and thickness (t_l) of the leaflets are all typical values for the native aortic valve [4; 39]. The density (ρ_f) and dynamic viscosity (μ) as given are the values for human blood with a hematocrit[1] of 45% [41]. These values were used for all four valves.

Table 4.1: Material parameters

E [N/m^2]	$5 \cdot 10^6$
ν[−]	0.3
ρ_l [kg/m^3]	$1 \cdot 10^3$
t_l [mm]	0.3
ρ_f [kg/m^3]	$1.05 \cdot 10^3$
μ [Pa·s]	$3.57 \cdot 10^{-3}$

The aortic and left ventricle (LV) pressures for a normal cardiac cycle can be seen in Figure 4.1 [42]. The difference between the two pressures with an added 10 kPa (as explained in Section 3.2 was used as an input for the inlet fluid boundary, while the output boundary was set to 10 kPa. Figure 4.2 shows the pressure difference.

The material was taken as linear isotropic instead of the actual non-linear orthotropic formulation and due to the fact that the aim was to compare different valves and the simulations were only for the systolic part of the cardiac cycle where the valve experiences very little strain (as explained in Appendix F), this was thought to be sufficient. Although blood is non-Newtonian it was modelled as Newtonian. This assumption has been made in most if not all analyses of heart valves [4]. Four-noded quadrilateral shells with three integration points and a Key-Hoff formulation, were used for the leaflets and Eulerian solid elements were used to model the fluid.

Because of the principle of closed volumes that MSC.Dytran uses to solve FSI problems (as described in Chapter 3), all three leaflets had to be closed

[1]The proportion of blood occupied by red blood cells is referred to as the hematocrit, and is normally about 45%.

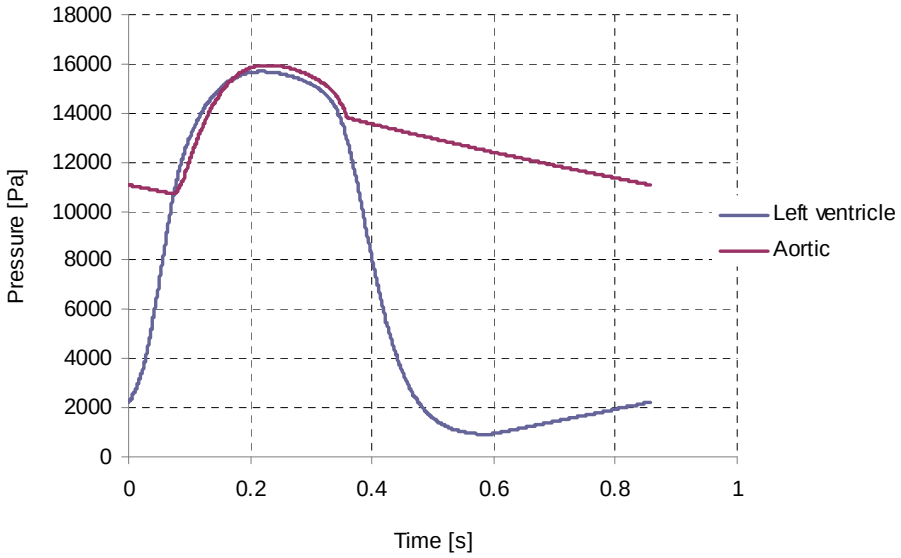

Figure 4.1: Pressure vs. time

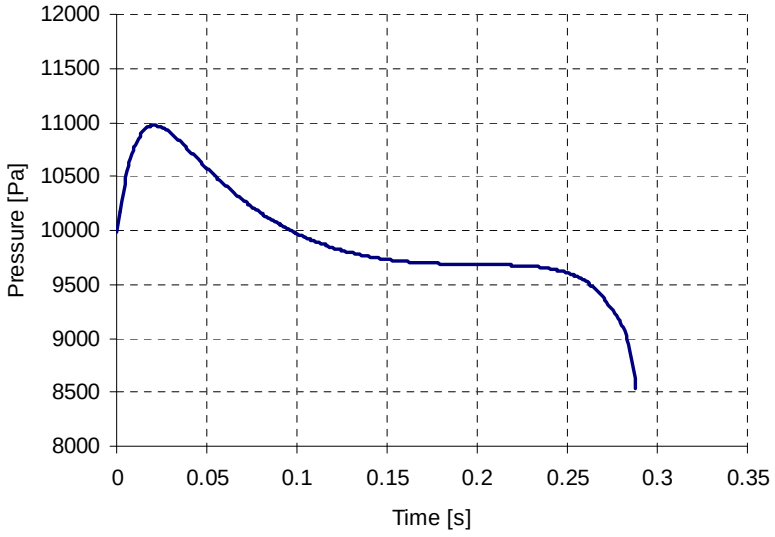

Figure 4.2: Pressure difference vs. time

with porous dummy elements. The inflow and outflow boundary also had to be closed with porous dummy elements, resulting in an aortic valve consisting of four closed volumes, each with its own fluid domain coupled to each other

through porous dummy elements.

To minimize central processing unit (CPU) time all elements except those on the leaflets and the dummies are rigid elements. The reason being that dummy and rigid elements require almost no computation. The rigid elements were also used to constrain the valve. Even though this effort was made, the average run time for a 288 ms simulation was about 36 hours on a Dell Precision 690 workstation with 8 Gb RAM and four CPUs running in shared parallel mode. This long run time is mostly attributed to the number of small Euler elements used to increase the accuracy of the simulations. Master-slave node contact was applied between the leaflets and between the leaflets and aortic walls. Table 4.2 gives a summary of the elements used for the valves (the geometry is described in Section 4.3).

Table 4.2: Element summary

	valve 1	valve 2	valve 3	valve 4
Key-Hoff Shells	1620	2775	2400	1482
Dummy Shells	336	2442	597	404
Rigid Shells	1143	10460	4371	2526
Eulerian Solids	256000	32000	32000	88000

4.3 Geometrical properties

Thubrikar [37] described the geometry of the native aortic valve with the parameters indicated by Table 4.3. The table also includes the parameters used for the four valves. The parameters are ratios with respect to Rb (the radius at the base of the valve). Figure 4.3 illustrates a sectional view of the valve model Thubrikar used to describe the native valve geometry. Ratios used for the four valves were chosen to be of the same order as those described by Thubrikar without taking their dependencies on each other into account.

Table 4.3: Aortic valve geometry ratios

	Rc	H	ϕ°	α°	C_c	Hs	L_f
Thubrikar	1.0	1.42	32	22	0.34	0.71	2.48
valve 1	1.0	1.40	37.19	11.7	0.0	0.0	2.53
valve 2	1.0	0.875	18.43	32.82	0.0	0.0	2.11
valve 3	0.9	0.92	29.85	24.973	0.13	0.228	2.08
valve 4	0.917	1.0	9.604	13.59	0.0	0.38	1.88

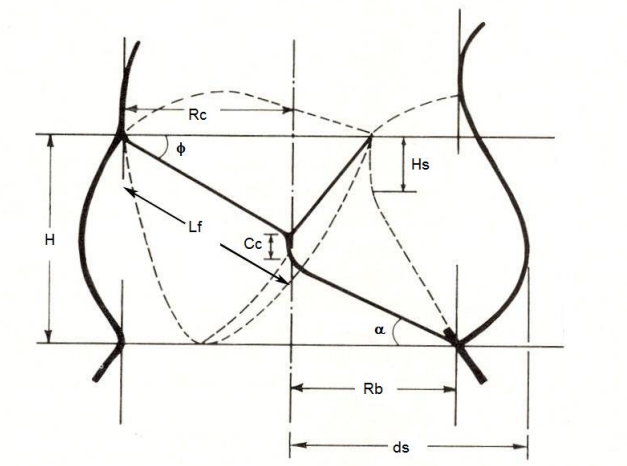

Figure 4.3: Valve dimensions

4.4 Opening and closing characteristics

Figure 4.4 shows an example of valve 2 during the FSI simulation along with velocity vectors of a few Eulerian elements. Valve 2 was constructed to have sinuses (curved sides), the other three valves all have straight sides. The valve was created with sinuses to further increase the difference between valve geometries.

The opening and closing behaviour of the four valves during the positive flow phase of the cardiac cycle is shown in Figure 4.5. The figures are for increments of 0.03 seconds, but because of the small time steps and the frequency on which data was written out the valves are not displayed at 100% the same time.

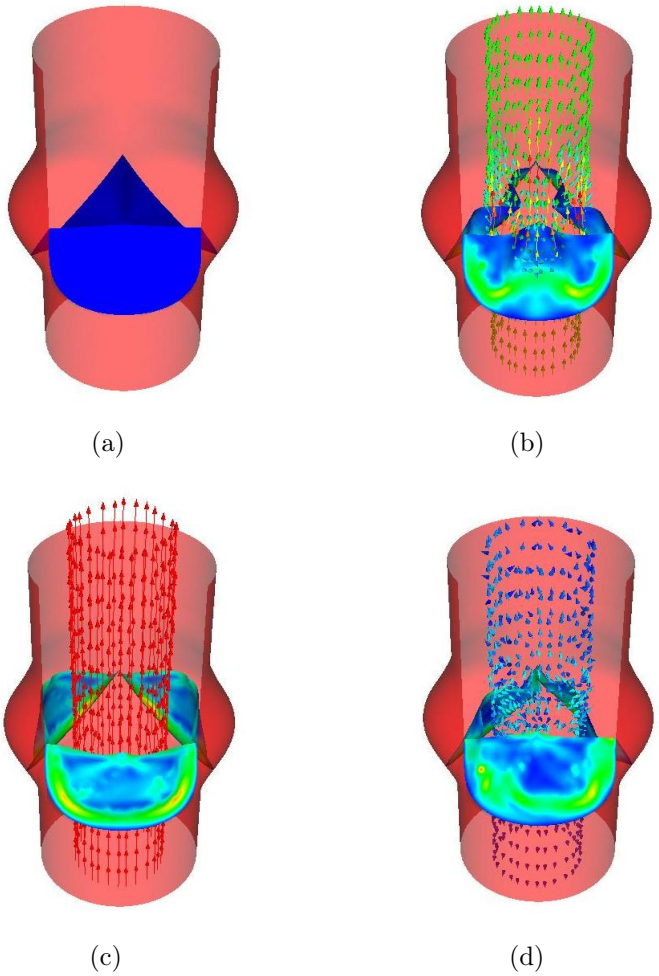

(a) (b)

(c) (d)

Figure 4.4: Valve 2

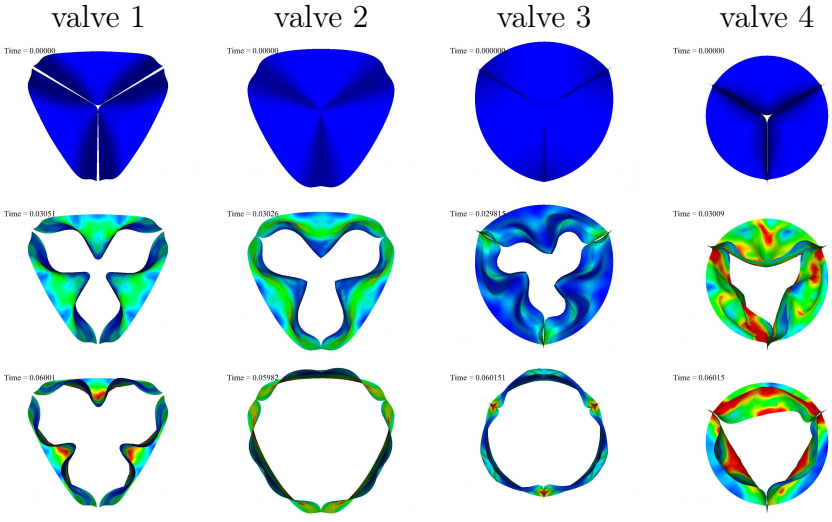

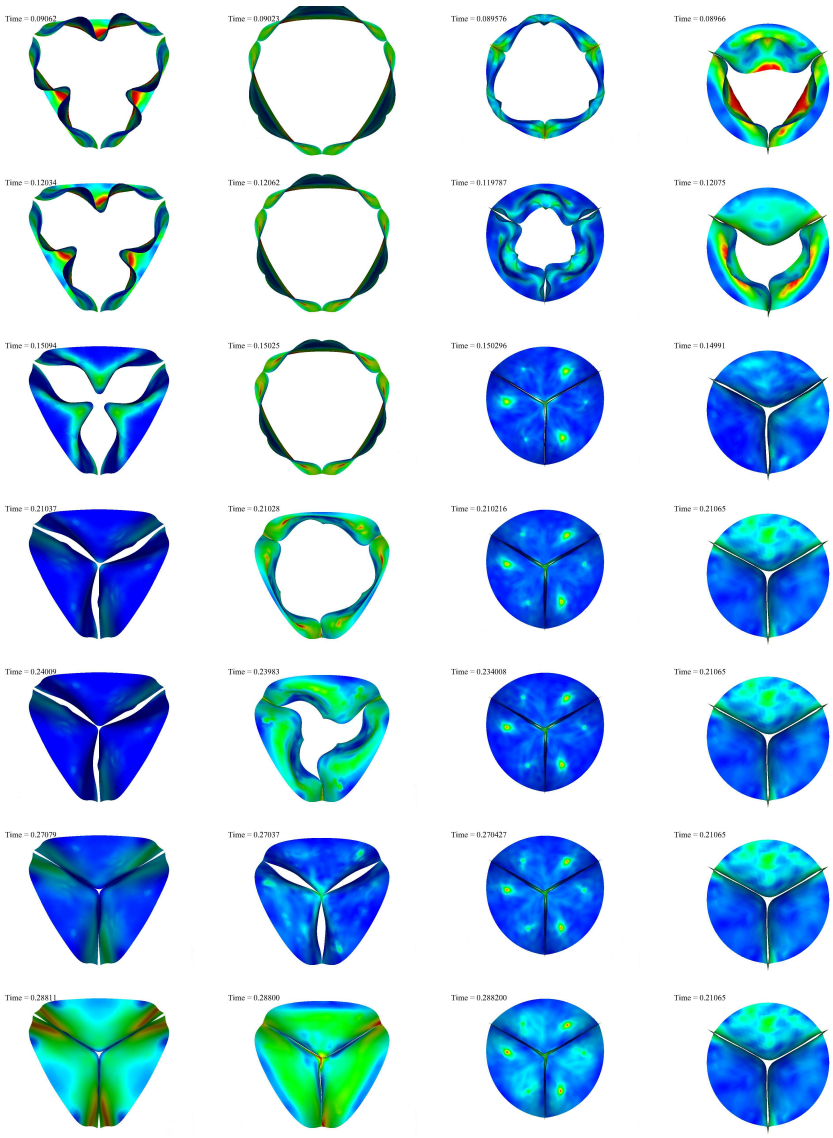

Figure 4.5: Movement over cardiac cycle

Characteristics one would typically require from the valve are smooth opening and closing. This means the leaflet must not make folds as illustrated by valve 4. Another aspect would be minimum leaflet resistance as shown by valve 2, which has the least resistance as it opens the quickest and stays open the longest. Figure 4.5 shows that valve 2 has the smoothest opening and closing behaviour followed by valve 3.

Valve 1 does not open completely. The reason being the long leaflet free edge length L_f. Because of the high L_f ratio for valve 1, a point forms at the leaflet edge as it opens. The further the valve opens the more resistant it

becomes to opening due to the forming of the point. With a higher pressure difference the leaflet's point does "pop" through causing the valve to open completely, but the formation of the point in the first place is not desired.

Due to its design, valve 4 also does not open completely with the applied pressure input. The leaflet area is simply too great, resulting in the valve giving too much resistance. The valve will however open completely with a higher pressure input.

The opening and closing characteristics of the four valves were compared with previous numerical results by Ranga *et al.* [39] for a dry model, Ranga *et al.* [30] for a wet model and experimental results by Leyh *et al.* [43] and Ranga *et al.* [30]. A wet model refers to an FSI problem and a dry model to a purely structural problem where pressures are applied directly to the leaflet nodes. Table 4.4 shows the comparison.

Table 4.4: Opening and closing characteristics

	RVOT [ms]	RVCT [ms]	ET [ms]
Ranga *et al.* [39] (Numerical:Dry)	35.7	39.3	207.2
Ranga *et al.* [30] (Numerical:Wet)	102.5	85	280
Ranga *et al.* [30] (Experimental)	70±27	92±23	321±23
Leyh *et al.* [43] (Experimental)	57.5±11	39.5±5	329±63
valve 1 (Numerical:Wet)	86.7	97.5	266
valve 2 (Numerical:Wet)	71	130	250
valve 3 (Numerical:Wet)	54.4	78	141
valve 4 (Numerical:Wet)	57.2	80	141

The rapid valve opening time (RVOT) is the time it takes for the valve to go from closed to open, where the rapid valve closing time (RVCT) is the time measured when the valve starts to close until it is completely closed. The ejection time (ET) is the time measured from initial opening to complete closure.

A good correlation was found between the four valves and experimental values by Ranga *et al.* [30] and Leyh *et al.* [43] as illustrated in Table 4.4. The dry simulation results by Ranga *et al.* [39] shows much faster times than the other measurements, this is caused by absence of fluid in his models.

Because all of the valves in Table 4.4 have different geometries and the ones from the literature have different boundary conditions different results are inevitable. This comparison however suggests that the numerical results of the four valves from this study fall within appropriate ranges for the investigated FEM parameters.

4.5 Stresses during systole

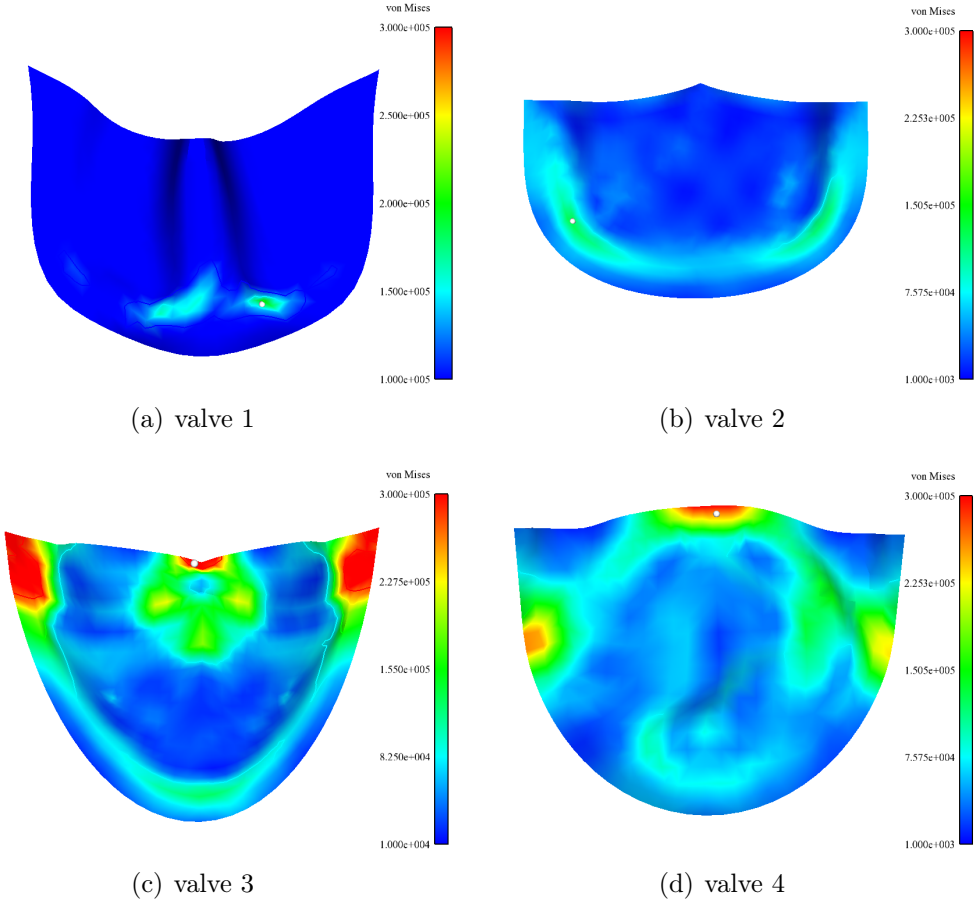

(a) valve 1 (b) valve 2

(c) valve 3 (d) valve 4

Figure 4.6: Maximum von Mises stress during systole

Figure 4.6 shows the Von Mises stress distribution on the leaflets. The FE models of Ranga *et al.* [30] showed peak overall Von Mises stresses ranging between $5.37{\cdot}10^5$ Pa and $6.55{\cdot}10^5$ Pa. In 2007 Ranga *et al.* [39] published another paper where a linear and non-linear leaflet were analysed, this time their results showed the peak overall stress during systole to be $5.00{\cdot}10^5$ Pa for both simulations.

Figure 4.6 indicate that the systolic stress distribution differs from the diastolic stress distribution (described in Section 4.6). The highest stress is found at the attachment points with 403 kPa being the highest stress in valve 3. Figure 4.6 also show that a better stress distribution across the leaflet resulted in a lower maximum stress.

4.6 Stresses during diastole

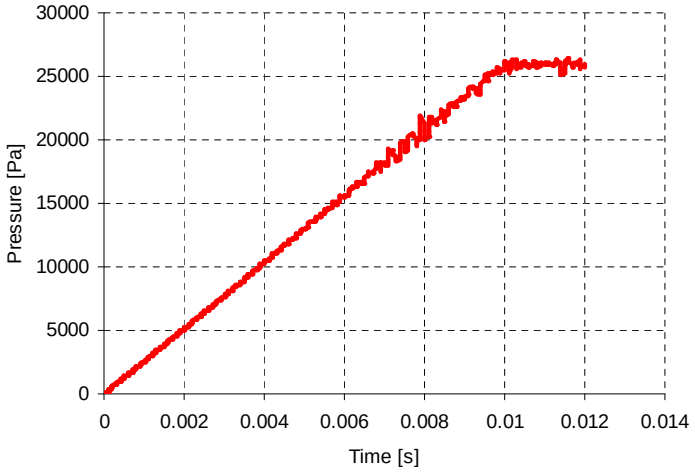

Figure 4.7: Back pressure vs. time

Leaflets experience much greater stress during diastole compared to systole. The higher stress is caused by the higher pressure difference between the aorta and the left ventricle during diastole. For the simulation the pressure difference in Figure 4.7 was applied to the aortic side fluid boundary. This boundary pressure difference was increased gradually from 0 to 200 mmHg (26 kPa) to minimize the effect of oscillations in the fluid.

Figure 4.8 shows the maximum von Mises stress along with the stress contours on the leaflets during a 200 mmHg back pressure cycle. The figures indicate that the maximum stress during diastole occurs at the upper attachment points (the legends were made equal for a better comparison). Valve 2 experiences the highest stress at 4.23 MPa, while valve 3 has the lowest maximum stress at 1.09 MPa. The figures also show that the maximum stress is reduced with a greater distribution of stress throughout the leaflet. This was the case with systolic pressure distribution as well. When comparing valves it is clear that valve 3 has the lowest stress due to an improved distribution of the stress.

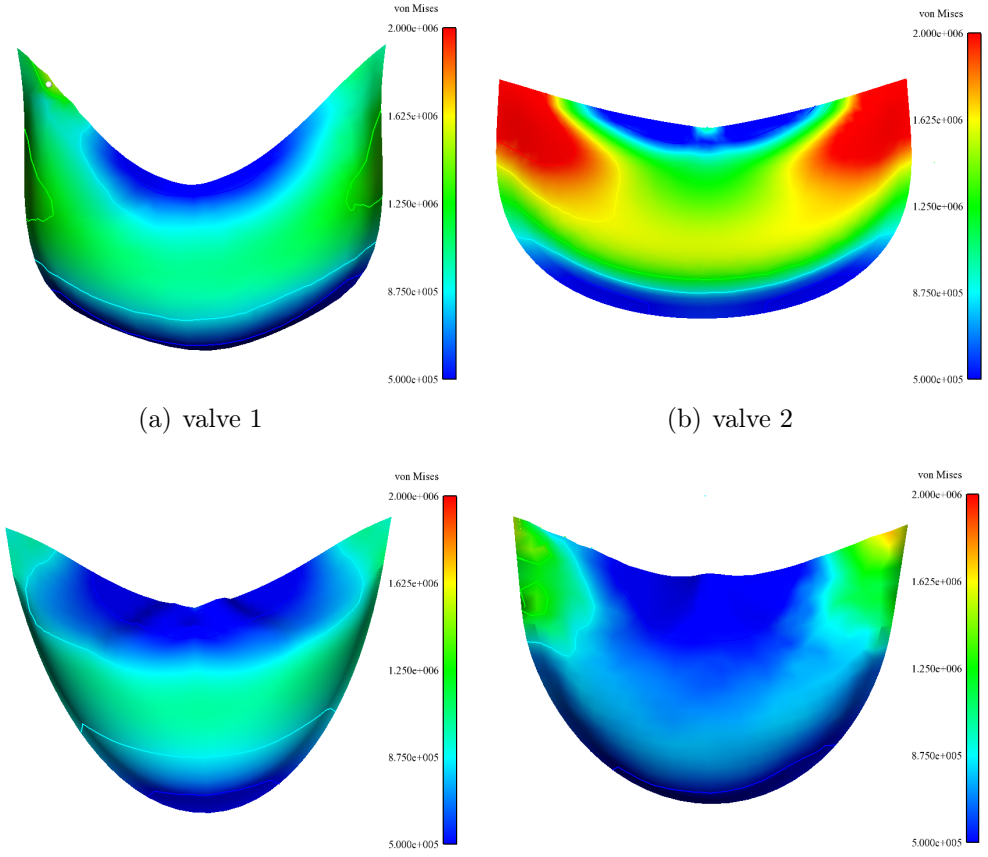

(a) valve 1 (b) valve 2

(c) valve 3 (d) valve 4

Figure 4.8: Maximum von Mises stress during diastole

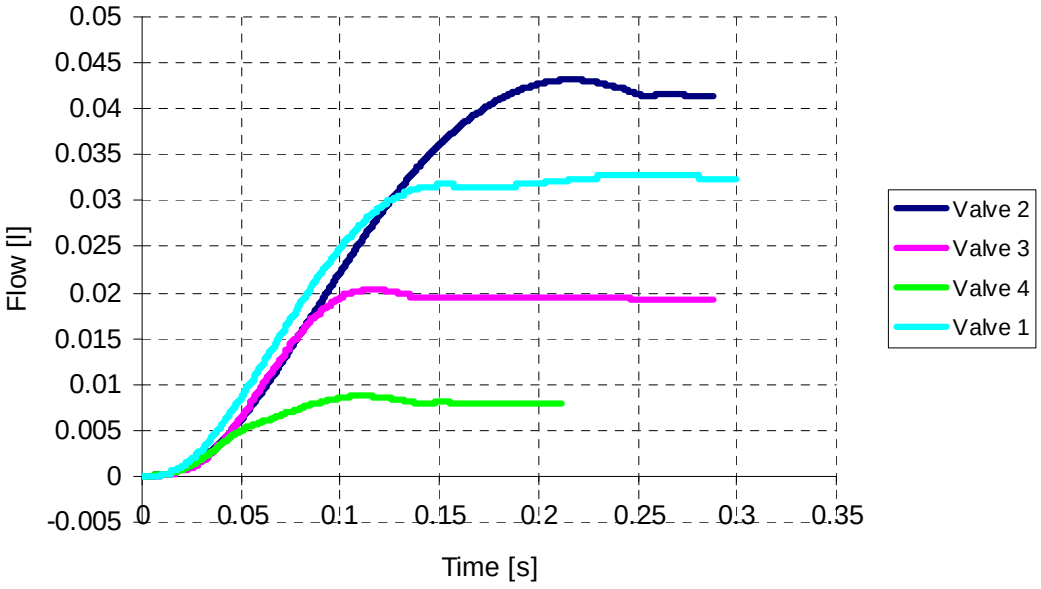

Figure 4.9: Total mass flow vs. time

4.7 Total mass flow and mass flow rate

Figures 4.9 and 4.10 shows the total mass flow (mfl) and mass flow rate (mflr) during the cardiac cycle for all four valves. The mfl (also known as the stroke volume) is the highest for valve 2, with 44 ml. This is a very low value and is probably caused by the short ETs of all four valves. The small pressure difference of ± 7.5 mmHg applied to the boundary also plays a role in the low stroke volume.

Figure 4.10 shows the obvious fact that the valves with the higher mass flows (as depicted in Figure 4.9 also have higher mass flow rates.

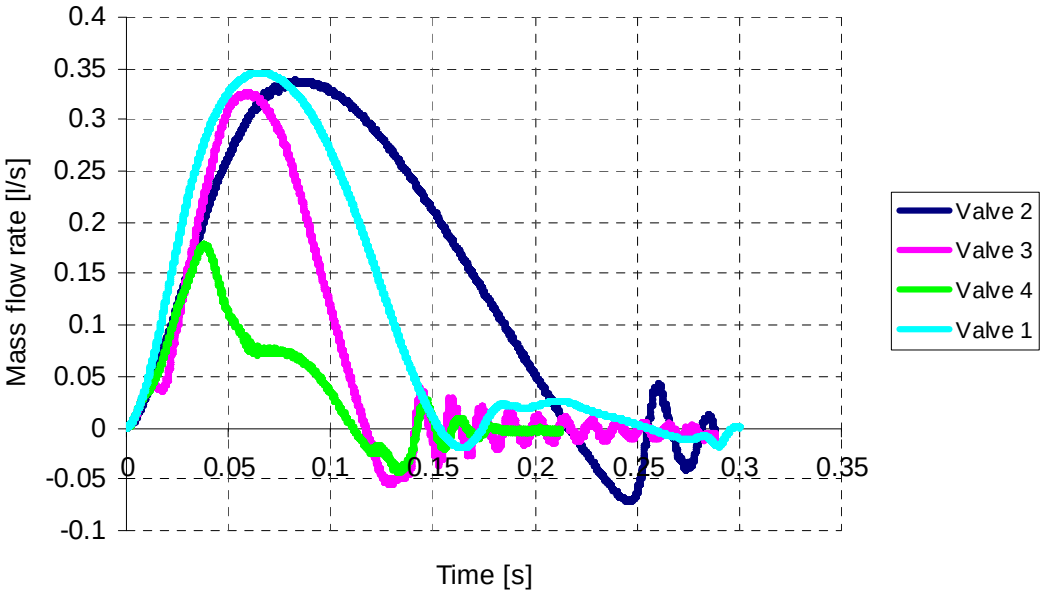

Figure 4.10: Mass flow rate vs. time

4.8 Effective orifice area

The effective orifice flow area is calculated from Equation 4.1, found in the international organisation for standardization (ISO) for Cardiovascular Implants [44]:

$$A_{EO} = \frac{q_{v_{RMS}}}{51,6 \times \sqrt{\frac{\Delta p}{\rho}}} \tag{4.1}$$

where

A_{EO}	is the effective orifice area in square centimetres;
q_{vRMS}	is the root mean square of the forward flow in millimetres per second;
Δp	is the mean pressure difference in millimetres of mercury measured over the positive period of the forward flow phase; and
ρ	is the density of the fluid in grams per cubic centimetre.

The ISO standards also states the minimum performance criteria for various valve sizes. Table 4.5 shows the minimum ISO values in comparison with the calculated values for the four valves.

Table 4.5: Minimum valve areas

$Valve$	ISO_{23mm}	ISO_{25mm}	$valve1_{24mm}$	$valve2_{24mm}$	$valve3_{24mm}$	$valve4_{24mm}$
A_{EO} (cm^2)	$\geq 1,00$	$\geq 1,20$	2.97	2.45	2.25	0.99

Table 4.5 shows that the areas of valves 1, 2 and 3 are greater than the ISO requirements for a 25 mm valve. It can then be assumed that it will be greater than the standard for a 24 mm valve. Valve 4 does however not make the minimum requirement.

4.9 Regurgitant volumes

Regurgitant volume is the volume of fluid that moves backwards into the heart during diastole. The regurgitant fractions for a 200 mmHg back pressure are compared to the allowed ISO values [44] in Table 4.6.

Table 4.6: Regurgitant volumes

$Valve$	ISO_{23mm}	ISO_{25mm}	$valve1_{24mm}$	$valve2_{24mm}$	$valve3_{24mm}$	$valve4_{24mm}$
%	≤ 10	≤ 15	8.43	3.86	4	18.75

The first three valves all have fractions less than the allowed fraction for a 23 mm and 25 mm valve. Valve 4 however does not reach the minimum value for any diameter.

4.10 Conclusion

During the analysis of the four valves valuable knowledge was gained to aid in the development of a prototype valve. First of all it was found that the geometry of the valve greatly affects valve performance and that by not choosing values judiciously will only result in design iterations. As previously mentioned, the valve must open with minimum resistance to the fluid. By accomplishing this, stresses in the leaflets are minimized, in turn minimizing the possibility of aortic stenosis developing and prolonging the valve's lifespan.

Thubrikar [37] documented the importance of other factors in valve design e.g. commisure radius (R_c), leaflet open angle (β) and commisure height (H_s). Firstly it is important for R_c to be smaller than R_b. A decrease in R_c results in a decrease in the valve height. Maximum valve height is achieved when $R_b = R_c$. Secondly, commissural height (H_s) also plays a role in valve height and a study by Thubrikar [37] showed that when $H_s = 0$ only a very tall valve is possible. The last factor influencing the valve height is β (as descussed in Chapter 5), this is the angle the valve leaflets make with the vertical plane. For $\beta = 0$ the flow conduit is perfectly cylindrical and the valve height is at a maximum. With $\beta \geq 0$ a valve of lower height would be obtained.

Table 4.7 shows the parameters developed by Thubrikar [37] to achieve optimal valve performance. These values where developed to guarantee appropriate sealing of the leaflets in the closed position, to ensure a proper valve height-to-diameter ratio and to minimuze energy usage [45].

Table 4.7: Optimum parameters for $Rb = 10$ mm

	H [mm]	R_c [mm]	H_s [mm]	$\beta[^\circ]$
Optimal valve	11.5	8-10	2.4-2.6	4-11

Chapter 5

Valve optimisation

5.1 Introduction

This chapter discusses the geometrical optimisation of the percutaneous aortic valve. The main purpose of valve optimisation is to facilitate minimum energy usage whilst ensuring proper opening and closing of the leaflets during the cardiac cycle. This will prolong the lifespan of the valve, especially the leaflets. Thubrikar [37] optimised a 20 mm diameter valve in 1990. His methods were applied to optimise the geometry for a 19 mm ($Rb = 9.5$ mm) and 25 mm ($Rb = 12.5$ mm) diameter valve, respectively, the internal diameters of the stents used in this project.

The Microsoft Excel Solver was used to find optimum valve dimensions for the specified stent diameters. Solver uses the generalized reduced gradient (GRG2) algorithm to solve non-linear problems [46].

5.2 Optimisation

Thubrikar [37] discussed a number of parameters for valve optimisation. Figure 5.1 illustrates a side preview of an aortic valve in both the open (green area) and closed (blue area) positions. The variables are: radius at the base Rb, radius of the commissures Rc, valve height H, height of the commisures Hs, angle of the open leaflet β, the angle of leaflet flexion θ, coaption height Xs, leaflet length in diastole Ld and leaflet length in systole Ls.

The illustrated valve dimensions were used by Thubrikar to derive Equations (5.1) - (5.4), (see Thubrikar [37], Appendix I for a derivation) . The valve

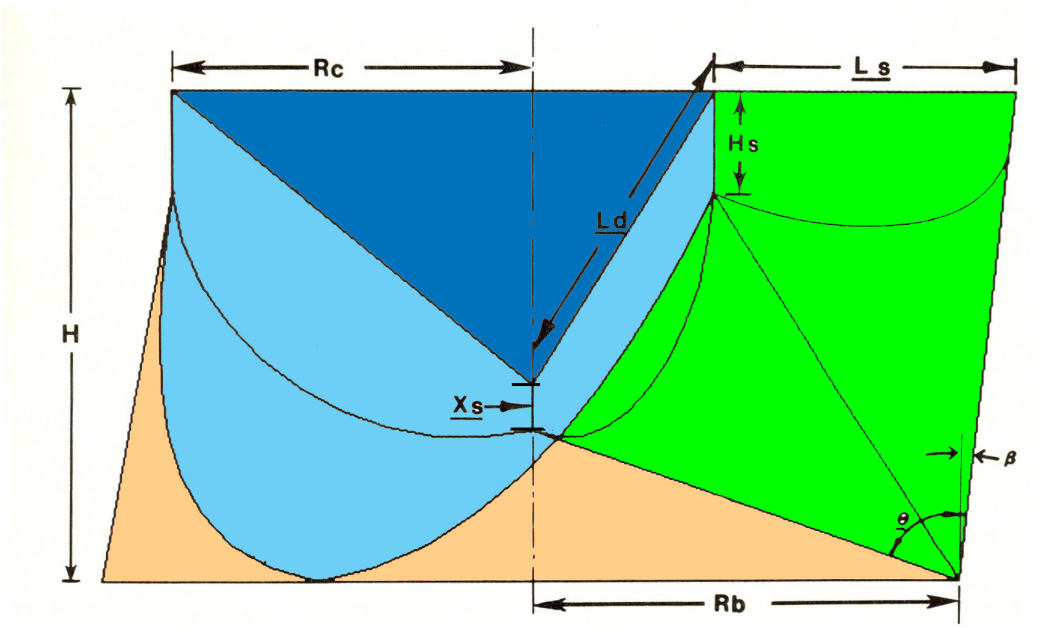

Figure 5.1: Valve dimensions [37]

geometry can be described by these four equations:

$$\theta = 180 + 2\beta - 2\tan^{-1}\left(\frac{H - Hs}{Rb - \frac{Rc}{2}}\right) \tag{5.1}$$

$$Xs = \frac{H}{\cos\beta} + \frac{Rb}{sin\left[\beta - 2tan^{-1}\left(\frac{H-Hs}{Rb-\frac{Rc}{2}}\right)\right]} \tag{5.2}$$

$$Ld = 2\sqrt{Rc^2 + \left\{H - Xs - Rb \cdot \tan\left[2\tan^{-1}\left(\frac{H - Hs}{Rb - \frac{Rc}{2}}\right) - \beta - 90\right]\right\}^2} \tag{5.3}$$

$$Ls = \frac{\sqrt{3} \cdot Rc\left[\pi - \left(\frac{\pi}{180}\right)2\tan^{-1}\left(\frac{\sqrt{3}\cdot Rc}{2Rb+2H\tan\beta - Rc}\right)\right]}{\sin\left[2\tan^{-1}\left(\frac{\sqrt{3}\cdot Rc}{2Rb+2H\tan\beta - Rc}\right)\right]} \tag{5.4}$$

To optimise Equations (5.1) - (5.4), design variables, a cost function and certain constraints are required. For the given problem the variable θ should be minimized and is thus the cost function. By minimizing the cost function the energy usage is minimized resulting in a slower fatiguing valve. The design

variables are H, Rb, Rc, Hs and β. The problem is subjected to the following constraints:

- $Xs = 0.1 \cdot Rb$; A certain minimum coaption height will eliminate leakage.
- $Ld = Ls$; When the leaflet free edge length in systole is equal to the length in diastole no folds are present on the leaflet surface.

The optimisation process was repeated twice, first for $Rb = 9.5$ mm and then for $Rb = 12.5$ mm. The variable Rc was varied between 6 mm and 10 mm for the first optimisation ($Rb = 9.5$ mm), and between 8 mm and 13 mm for the second optimisation ($Rb = 12.5$ mm). The angle of the open leaflet β was set to zero because the valve is stented and the stent restricts the leaflets from opening. In the native aortic valve β can be bigger than zero, which causes the valve height to decrease.

The process can be summed up as follows:

1. There are four equations describing the geometry of the valve.
2. The known values are Rb, β and Rc. The unknown values are H, Hs, Xs (Equation 5.1), Ld (Equation 5.2), Ls (Equation 5.3) and θ (Equation 5.4).
3. Tell the solver to minimize θ by changing the values of H and Hs and by applying the constraints that $Xs = 0.95 \cdot Rb$ and $Ld = Ls$.

5.3 Results

Optimisation results for both the 19 mm and 25 mm valves are depicted in Figures 5.2 - 5.5. Figure 5.2 illustrates the effect that the leaflet flexion angle θ have on valve height H. The curves illustrate the range of optimum values available for the valve. This is then also where a design decision must be made, in other words an appropriate valve height must be chosen. With a chosen valve height, the remainder of the dimensions can be selected from Figures 5.3 - 5.5.

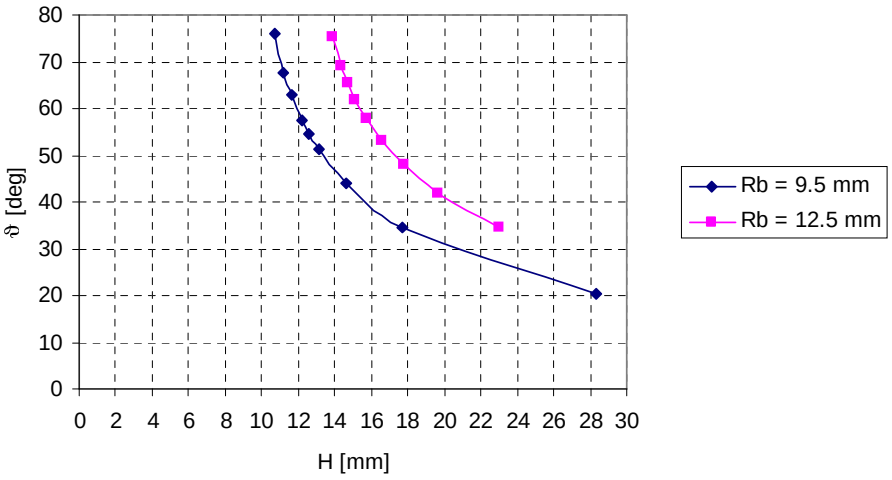

Figure 5.2: Leaflet flexion angle θ vs. valve height H

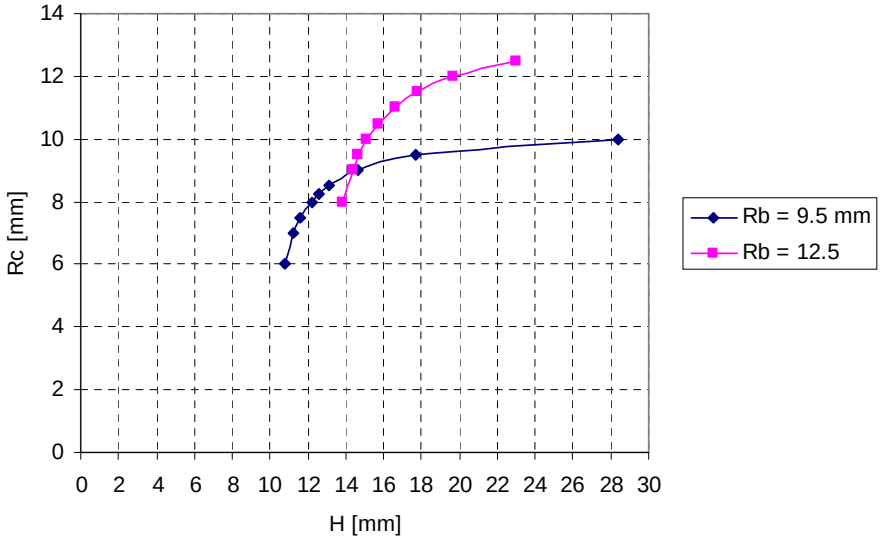

Figure 5.3: Commissure radius Rc vs. valve height H

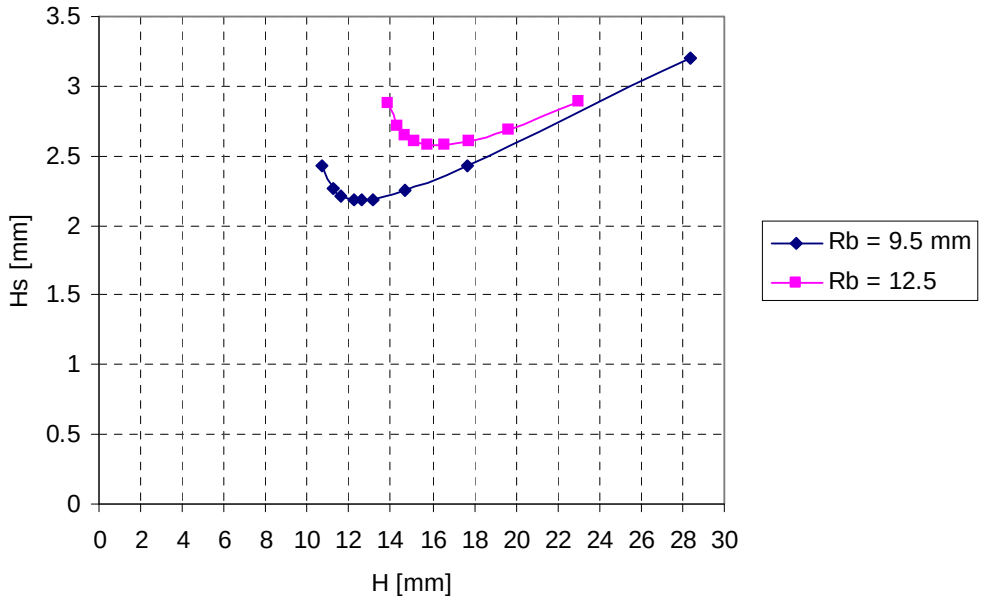

Figure 5.4: Commisure height Hs vs. valve height H

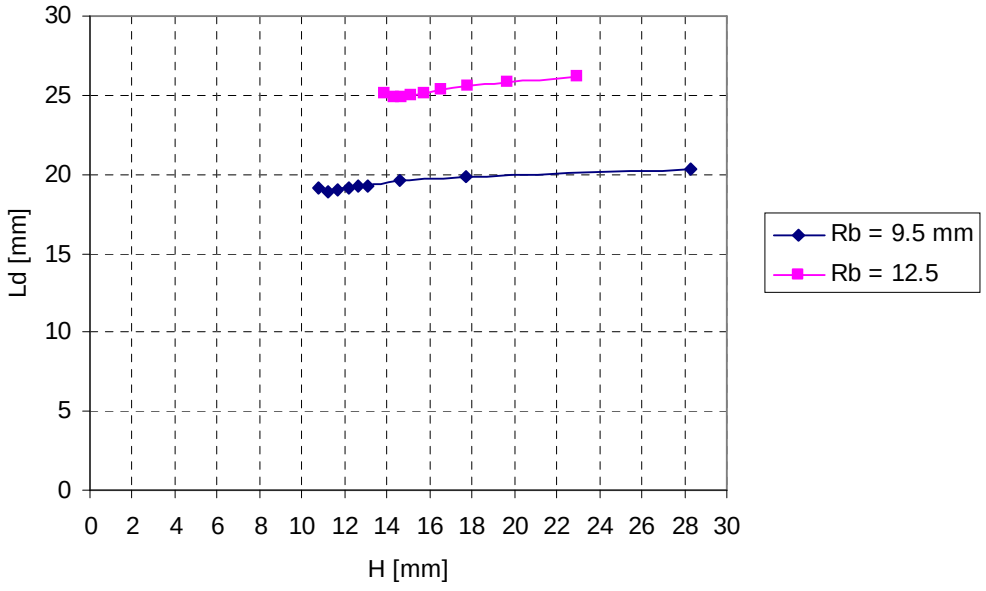

Figure 5.5: Leaflet free edge length Ld vs. valve height H

5.4 Optimum leaflet simulation

The valve in this section was constructed by using the geometry graphs resulting from Section 5.3. Valve specifications were for a 20 mm stent, with a wall thickness of 0.5 mm, resulting in $Rb = 9.5$ mm. A height restriction of 12.6 mm was used due to attachment difficulties. Leaflets are designed for a stented valve, thus β can not be greater than zero. The outcome of this additional restriction is that only one set of optimal dimensions are produced for a certain valve height. By excluding the height restrictions it would be possible to shorten the valve, but in effect the flexion angle would increase, resulting in rapid fatigue.

The process of obtaining the valve dimensions are discussed below:

1. Firstly, determine the inside diameter of the stent (outside diameter of the valve), in this case $Rb = 9.5$ mm.

2. By drawing a vertical line at the height restriction H of 12.6 mm on Figure 5.2, the leaflet flexion angle is found to be 54°.

3. Continuing to the next figures and repeating Step 2, Rc, Hs and Ld can be obtained.

By following the above steps the optimal dimensions for a stented valve with $Rb = 9.5$ mm, $H = 12.6$ mm and $\beta = 0$ was obtained. The next step is to simulate the optimised valve to investigate its performance. Table 5.1 gives the dimensions for the stented valve used in the simulation.

Table 5.1: Optimum valve dimensions

Rc	H	$\theta°$	Xs	Hs	Ld
8.25	12.6	54	0.95	2.18	19.18

The valve geometry is shown in Figure 5.6. A FSI simulation was done for the opening and closing phases of the cardiac cycle. Simulation parameters are shown in Table 5.2, which are the same as the values used in Chapter 4. The mass flow rate curve, used as input boundary condition, is depicted by Figure 5.7 .

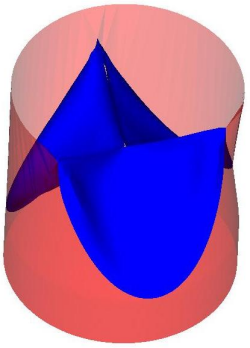

Figure 5.6: Optimum valve for $Rb = 9.5$ mm

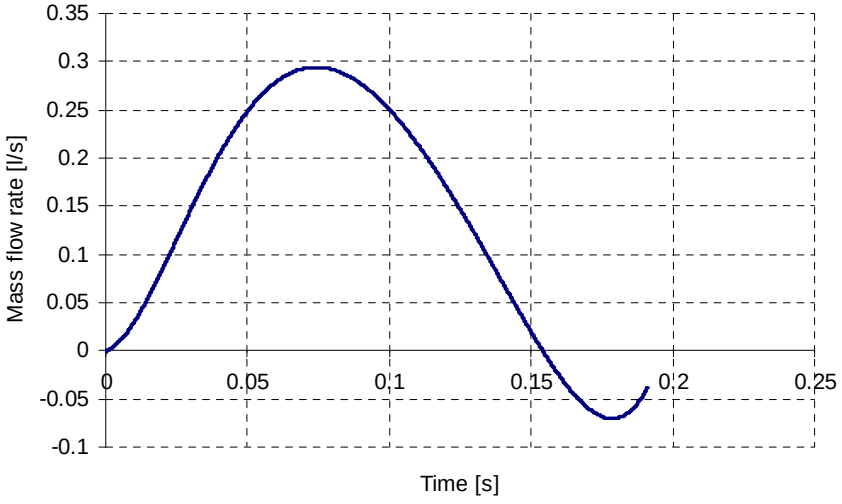

Figure 5.7: Input mass flow rate

Table 5.2: Material parameters

E [N/m^2]	$5 \cdot 10^6$
ν[$-$]	0.3
ρ_l [kg/m^3]	$1 \cdot 10^3$
t_l [mm]	0.3
ρ_f [kg/m^3]	$1.05 \cdot 10^3$
μ [Pa·s]	$3.57 \cdot 10^{-3}$

Opening and closing characteristics

Figure 5.8 depicts the valve during the opening and closing phases of the cardiac cycle, which runs from (a) to (c) . The figure illustrates that the valve opens end closes sufficiently. The RVOT, RVCT and ET are 54 ms, 90 ms and 190 ms respectively. These values compare very well with the values discussed in Section 4.4 when keeping in mind that this simulation was for a lower stroke volume than the simulations done in Section 4.4.

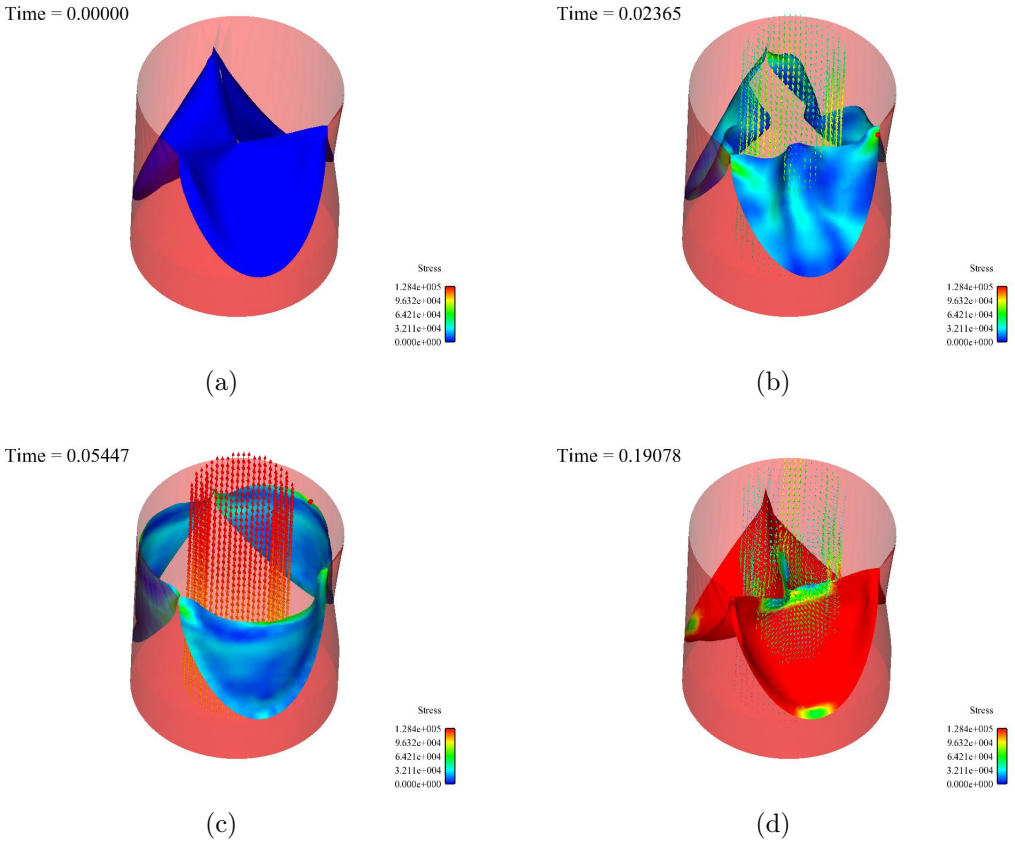

Figure 5.8: Optimum valve simulation

The valve resistance is depicted in Figure 5.9. The figure shows a maximum resistance of 850 Pa. When compared to the resistance and flow rates obtained in Chapter 4, this is definitely an improvement. A maximum resistance of 850 Pa is still high though, this is because of the short ejection time of the valve. The input flow lasted for only 0.15 s while the flow output from Chapter 4

lasted for 0.22 s for valve 2 (which showed the best result). The valve in this simulation also have a smaller diameter than the valves in Chapter 4.

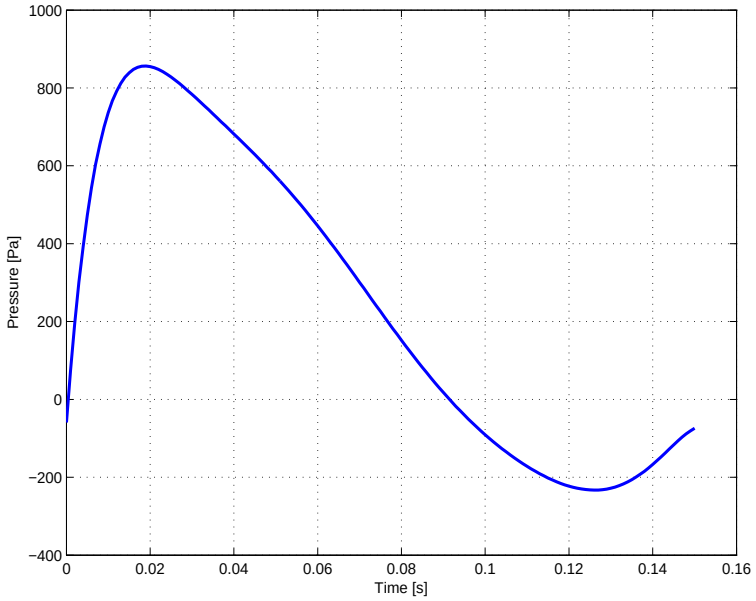

Figure 5.9: Valve resistance vs. Time

5.5 Conclusion

Thubrikar [37] showed that optimal and native valve geometries are very similar, hence it can be said that the native valve is performing optimally. A stented valve used for percutaneous implantation can however not have the same geometry as a native valve. The main reason being that the native valve contains sinuses which allow β to be greater than zero, in effect causing the valve height to decrease. A stented valve has no sinuses, therefore β is equal to zero.

This chapter aimed to aid the valve designer in designing a valve with a proper opening and closing characteristic, enabling him to choose the appropriate dimensions quickly and accurately.

Aortic valve dimensions are dependent on each other and by not selecting dimensions judiciously could result in a defective valve unable to open or close properly.

Chapter 6

Leaflet attachment forces

6.1 Introduction

One of the main problems faced during the design of a stented valve is physically attaching the valve to the stent. Attachments are typically the regions where the highest stress concentrations occur. Another problem in stented valve design is the forces acting on the stent from the valve. The goal of finding the forces acting in-between the leaflets and the stent is to give the stent designer an idea of the forces to be considered during a stent fatigue simulation to determine if the stent is capable of withstanding the radial and axial forces over a high pressure cycle.

To ensure simulation accuracy, simulations were done using two different finite element codes and a comparison was made between the results.

6.2 Modelling

The valve used in this simulation is the same one that was designed in Section 5.4 for a 20 mm diameter stent. The leaflet with its nodes of interest is shown in Figure 6.1. The assumption was made that the leaflets would behave symmetrical, hence only one half of the attachment nodes were post-processed. This assumption is supported by research done by Ranga *et al.* [39] who studied the left ventricle outflow tract and found that even though the flow is asymmetrical it is so little that symmetrical flow as input will be appropriate.

To increase the validity of the results, a dry simulation using two different finite element codes was done for a high pressure cycle. Consequently the

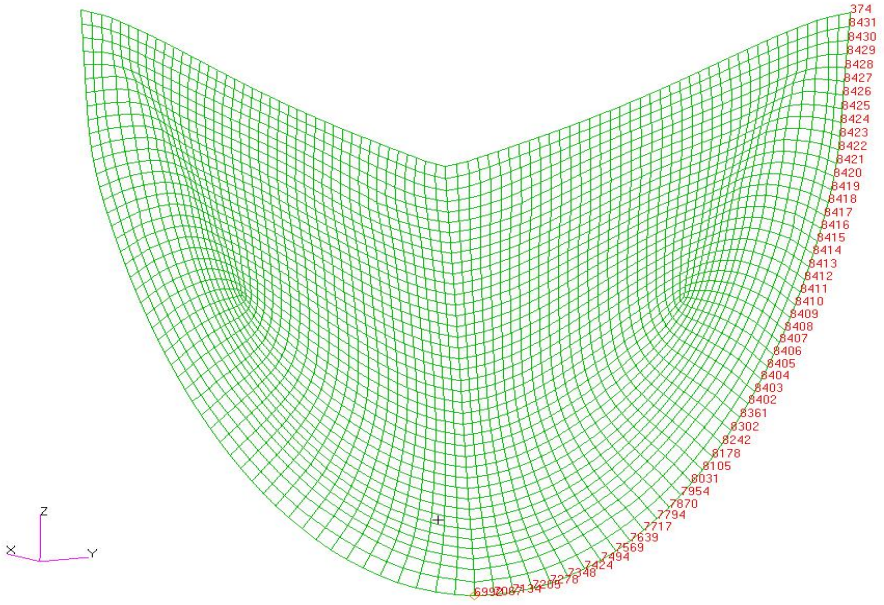

Figure 6.1: Node numbers

valve was simulated twice, once using the explicit solver of MSC.Dytran and again using the implicit non-linear solver of MSC.Marc. Both simulations were transient dynamic, with the difference between the two pressure curves shown in Figure 6.2 applied to the elements on one side of the leaflets. Only the first 0.5 seconds were used in the simulation, because this interval includes the time from minimum to maximum pressure during the cardiac cycle. Initially, the leaflet mesh size was larger, but results indicated that with a mesh refinement results from the two codes correlated more closely. This also supports the accuracy of other simulation results throughout the paper as a fine mesh was used for all models.

The technique of using spatially uniform, but temporally varying pressures in dry models, compared to the more accurate FSI methods, is supported by many authors, including Carmody *et al.* [4] and Arcidiacono *et al.* [33]. Dry simulations are less expensive (in terms of CPU time) than FSI simulations. For the purpose of simulating a real 3D situation, contact was defined between the leaflets. MSC.Dytran makes use of a master-slave-node scheme. In order to maintain symmetry, one half of a leaflet was set to "master" and the adjusant leaflet's half was set to "slave". Thus, for a total of three leaflets, one has six contact definitions. A different scheme is used by MSC.Marc, where only those

elements that have a possibility to come into contact during a simulation are defined in the MSC.Marc contact card.

The elements used in the MSC.Dytran simulation are four-noded quadrilateral Key-Hoff shells, with three integration points through the shell. These shells are computationally more expensive than other shells available in MSC.Dytran, but they show better performance when the strain is greater than 5% [34]. The elements used in the MSC.Marc simulation are "special element" number 139, which is a bilinear thin-shell element. This element is not very sensitive to distortion and performs well in non-linear analyses [47].

The parameters for the simulation are tabulated in Table 6.1. These are typical values for leaflet material.

Table 6.1: Force simulation properties

E [MPa]	5
ρ [kg·m^3]	1000
υ	0.33
Elements	8250

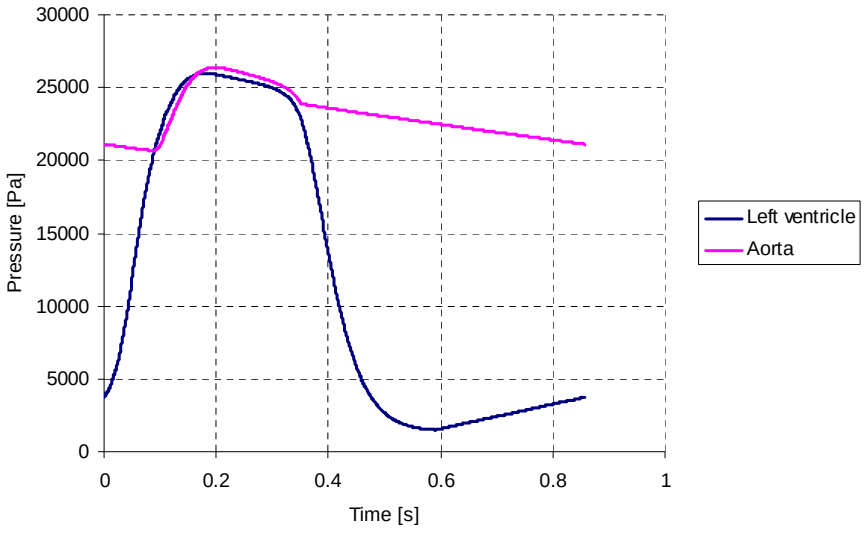

Figure 6.2: Pressure vs. time

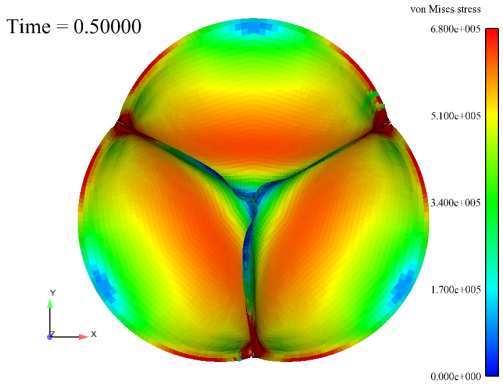

Figure 6.3: Von Mises stress: explicit

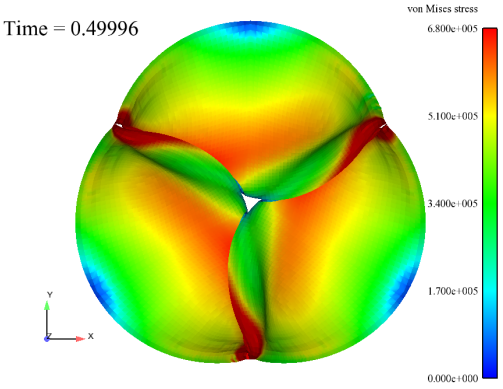

Figure 6.4: Von Mises stress: implicit

6.3 Results

The explicit code has proved to be much more efficient than the implicit code for the short duration simulation. Due to the short duration of the simulation and the highly non-linear deformation of the leaflets, a small time step had to be chosen for the implicit solver to ensure convergence. For a short duration simulation, the explicit code has the advantage of using small steps anyway. Less CPU time is utilized because the explicit code does not have to invert the stiffness matrix, which can require up to 90% of the solution time [4]. The simulation time for the MSC.Dytran model was ±1 hour compared to the MSC.Marc model which had a simulation time of ±22 hours.

Figures 6.3 and 6.4 depicts the Von Mises stress distribution from the top view for the explicit and implicit simulations respectively. This maximum stress is achieved at time 0.5 seconds, when the pressure difference across the leaflets is the greatest.

Figure 6.5 shows the strain energy density curves of all three leaflets for both the explicit MSC.Dytran and the implicit MSC.Marc simulation. The curves indicate that the implicit code has a ±5% higher strain energy density during diastole. This difference is not significant if taken into consideration that different codes, element formulations and contact algorithms were used. Figure 6.6 shows the radial and axial forces for one half of a leaflet over the cycle. Strong similarities between the values of the maximum radial force and the maximum axial force were noticed. Both maxima occured at 0.5 seconds, the same time as the maximum stress at the attachment points shown in

Figures 6.3 and 6.4.

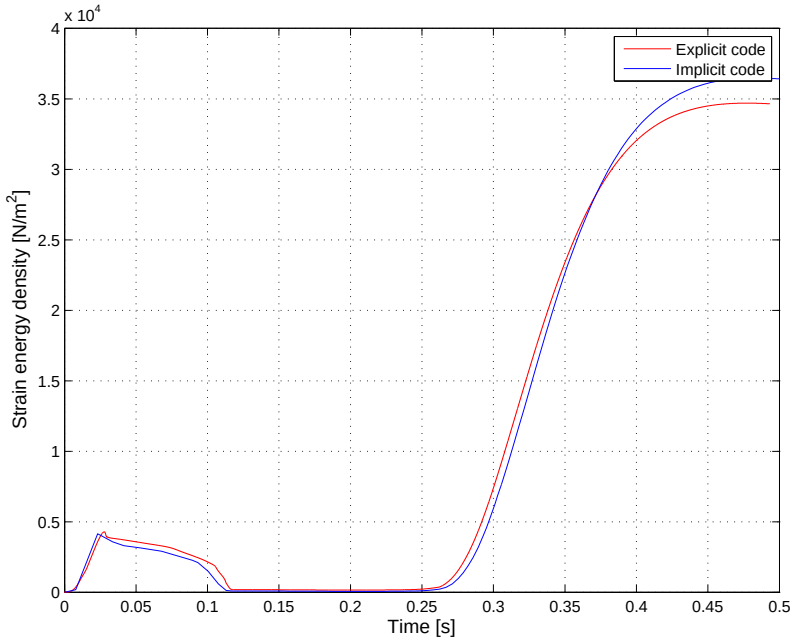

Figure 6.5: Strain energy density vs. time

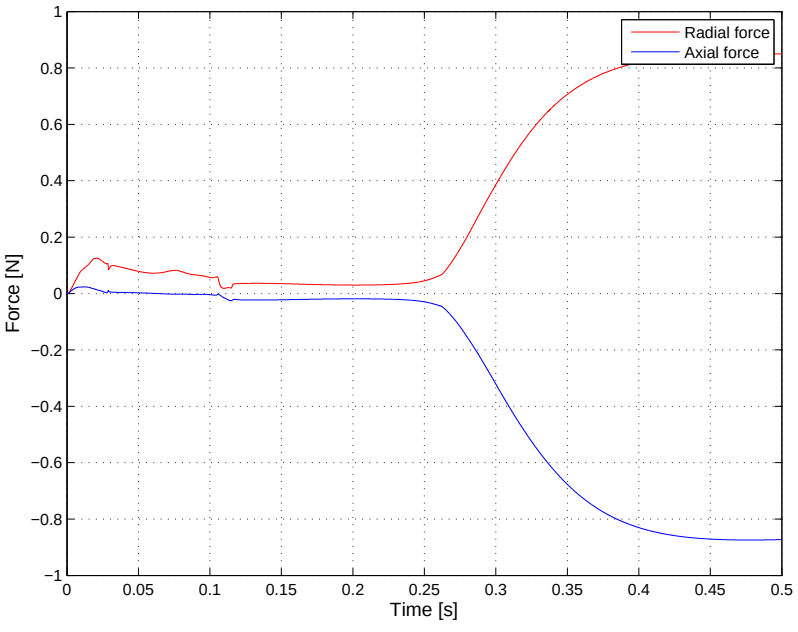

Figure 6.6: Force vs. time

6.4 Conclusion

The aim of this chapter was to extract the leaflet attachment forces for further use in the stent design. The attachment forces were calculated with a FE model which was solved using two different codes and methodologies. According to ISO requirements a valve should be able to take one diastolic cycle of 230 mmHg [44]. In a normal heart the maximum pressure during diastole is 120 mmHg, therefore it was thought that by applying a 165 mmHg pressure to the valves will be a good approximation for a high pressure cycle. This results in a safety factor of 1.4. It would be pointless to design a valve that can take 230 mmHg every cycle. This will result in an overly strong and thick stent and the idea is to design a stent that is as small as possible.

A good correlation was found between the results from both simulations. The leaflet forces can now typically be used by a stent designer to load a stent for fatigue testing.

Chapter 7

Straight and curved back valve comparison

7.1 Introduction

Leaflet attachment can be narrowed down to two methods. The first method is to attach the leaflet edge to the stent in a straight line along the axial direction of the stent. Figure 7.1 shows an example of this method. The second method is to attach the leaflet edge in a parabolic line to the stent; Figure 7.2 shows an example of this method.

Attaching the leaflet edge in a straight manner is much easier when the stitching is done by hand, but a curved attachment resembles the native valve

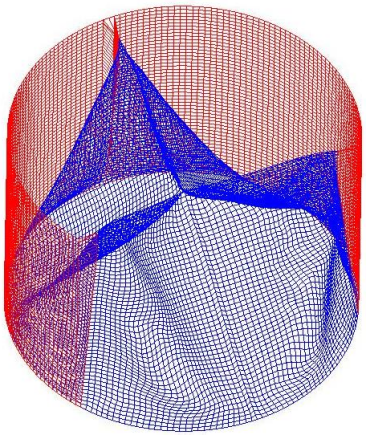

Figure 7.1: Example of a straight attachment

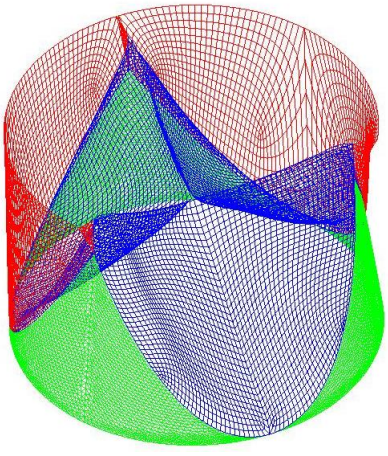

Figure 7.2: Example of a curved attachment

more closely. Therefore the goal of this chapter is to critically evaluate and compare the two valves, with the use of FSI simulations, and to identify any significant differences.

7.2 Finite element models

Geometry creation

It is more difficult to construct a computer aided drawing (CAD) model of the aortic valve in the closed position compared to the open position. The reason for this is because of the leaflet shape and initial contact between the leaflets in the closed position. In the open position the leaflets form a perfect cylinder where in the closed position they form a complex geometry. The initial contact between adjusant leaflets makes meshing the leaflets and assigning the FSI boundary conditions complicated. Therefore an alternative method of creating a model of the valve was investigated that would make the meshing process easier. It was found that a good way of setting up the problem when working with MSC.Patran as pre-processor is as follows:

- Construct a third of the valve in the open position using MSC.Patran
- Where the leaflet is supposed to make contact with the other two leaflets during closure, construct a rigid contact surface.
- Construct a FE model and then apply a pressure on the leaflet to close it, but not so much that strain occurs.
- When the leaflet is pressed closed with the specified contact distance between the leaflet and the rigid surfaces, extract the mesh.
- The deformed leaflet mesh can be used to create a surface. By remeshing the surface, a good leaflet mesh can be obtained.
- Lastly, create the rest of the mesh to satisfy the FSI solver's criteria. By rotating all the elements twice, three identical leaflets in the closed position can be created.

Simulation parameters

Element sizes, especially on the leaflets, are very small. This is because (as mentioned in Chapter 6.2), the finer mesh, although computationally more expensive, is required for accuracy. Numerical validation of the results is only possible with another FSI package. It was thus decided that as an alternative to purchasing another FSI package, credibility of results would be increased by focusing on leaflet and fluid mesh refinement. Mesh refinement sensitivity is discussed in Appendix C.

Both valves have the same dimensions except for the straight or curved leaflet attachment edge. Geometrical and material parameters are shown in Table 7.1. The geometrical parameters are for an optimised 20 mm diameter valve. The material parameters where chosen to reflect the properties of the native valve.

Table 7.1: Simulation parameters

Geometry		Material	
Rb [mm]	9.5	E [N/m^2]	$5 \cdot 10^6$
Hs [mm]	2.18	t_l [mm]	0.3
H [mm]	12.6	ρ_f [kg/m^3]	$1.05{\cdot}10^3$
Xs [mm]	0.95	μ [Pa·s]	$3.57{\cdot}10^{-3}$
Lf [mm]	19.18		
β[°]	0		
θ[°]	54.5		

The valve mesh consists of various different element types of which only the leaflet and fluid elements are of real interest. For the leaflets, four-noded quadrilateral shells with a Belytschko-Lin-Tsay (BLT) formulation were used. They are the most efficient shells in MSC.Dytran [34]. Hexahedral solid elements were used to construct the fluid mesh. In order to make use of the fast coupling algorithm in MSC.Dytran these solid elements have to be aligned with the basic coordinate system. Because both valves are stented, the outside surfaces of the valve consists of rigid elements. Dummy elements are used to create closed volumes for the FSI solver. A summary of the elements used is given in Table 7.2. Note the difference between the number of BLT shells for the straight and curved valves. The difference is caused by the larger surface area of the straight valve leaflets.

Table 7.2: Element summary

	Straight valve	Curved valve
Belytschko-Lin-Tsay	9000	6612
Dummy shells	2397	728
Rigid shells	12594	17181
Eulerian solids	134750	134750

Boundary conditions

Both valves have six master-slave-node contact conditions, three for contact between the leaflets and three for contact between the leaflets and the outside surface representing the stent. To decrease the computational effort, timers are used to switch the contacts on and off during the simulation.

The fluid boundary conditions consists of an inflow boundary, where inflow velocity is given in a subroutine as a function of time and a constant pressure on the outflow boundary side. The reason for using a velocity input instead of a pressure input is to calculate the pressure drop across the valve over time. The subroutine is compiled with the original MSC.Dytran executable to create a new executable, using the Microsoft Intel Fortran 9.1 compiler on a Linux platform.

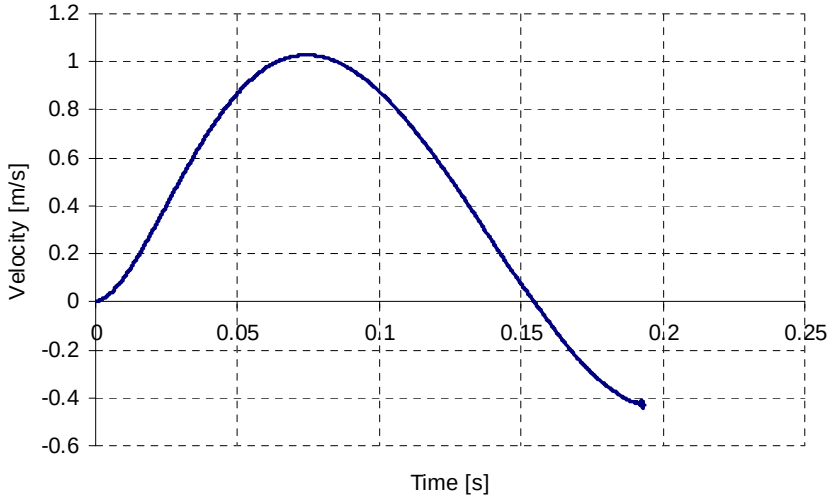

Figure 7.3: Input velocity vs. time

The area of interest was the opening and closing characteristics of the valves, therefore only this phase of the cardiac cycle was simulated. The velocity boundary condition curve is depicted in Figure 7.3. This input velocity gives a stroke volume of 26 ml. The systolic part of the simulation lasts for 0.55 s and systole is approximately 33.8% of the total cardiac cycle [48] which results in a heart rate of 131 bpm. The resulting cardiac output can then be calculated as 3.4 l/min. This heart rate was chosen to reduce the already long computation time to simulate systole.

7.3 Results

Both simulations were run on a Dell Precision 690 workstation with eight CPUs (of which only four CPUs were used). Total run time was ±80 hours for each simulation. Post processing was done with Ensight 8.2.

Resistance

As mentioned, the input boundary condition was specified with a velocity equation. This allowed the input pressure to change over time as a result of the input flow and the constant output pressure boundaries. Figure 7.4 shows the pressure difference across the valves.

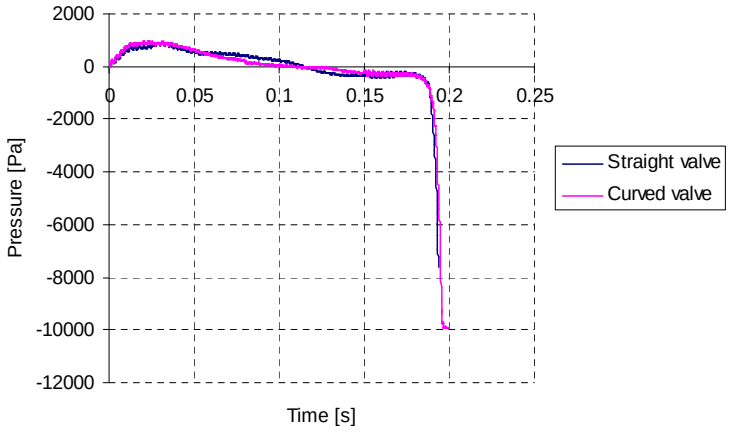

Figure 7.4: Pressure difference vs. time

From the figure it is clear that the pressure losses (or pressure differences) across the valves are very similar. The maximum pressure difference for the straight valve is 897 Pa and the maximum pressure difference for the curved valve is 900 Pa. The peak pressure loss in a 23-26 mm bioprosthetic valve, for a cardiac output of 5 l/min, is ±7 mmHg (933 Pa) [37]. A 20 mm diameter valve will have an increase in pressure loss for a 5 l/min cardiac output. The results are difficult to compare to those from a normal heart with a native valve, the reasons being that the native valve has a bigger diameter (26mm) and the cardiac output is higher. The goal is however to compare two designs to each other and not with a bigger human native valve.

Energy

Strain energies of the two valves are compared in Figure 7.5. This is only for the positive flow period through the valves. The straight valve reaches a peak of 161 μJ at 0.035 s and the curved valve reaches a peak of 168 μJ at 0.046 s. This peak occurs almost halfway through the opening cycle, when the leaflets are slightly bent in the middle.

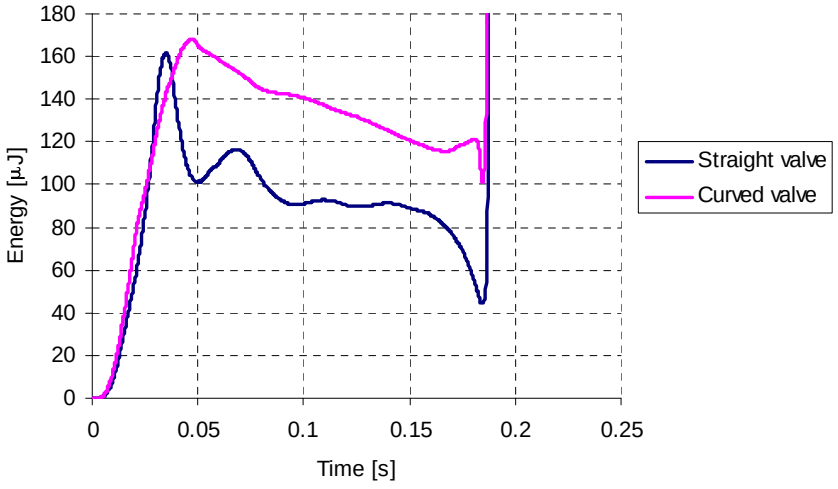

Figure 7.5: Strain energy vs. time

Opening and closing behaviour

The opening and closing of the valves are depicted in Figure 7.6. Table 7.3 shows a rapid valve opening time (RVOT) of 80 ms for the curved valve, 20 ms slower than the straight valve. At 85 ms, the curved valve has a shorter rapid valve closing time (RVCT) time than the straight valve. The ejection time (ET) for both valves are more or less the same at 187 ms and 194 ms for the straight and curved valves, respectively.

Table 7.3: Valve characteristics

	Straight valve	Curved valve
RVOT [ms]	60	80
RVCT [ms]	106	85
ET [ms]	187	194

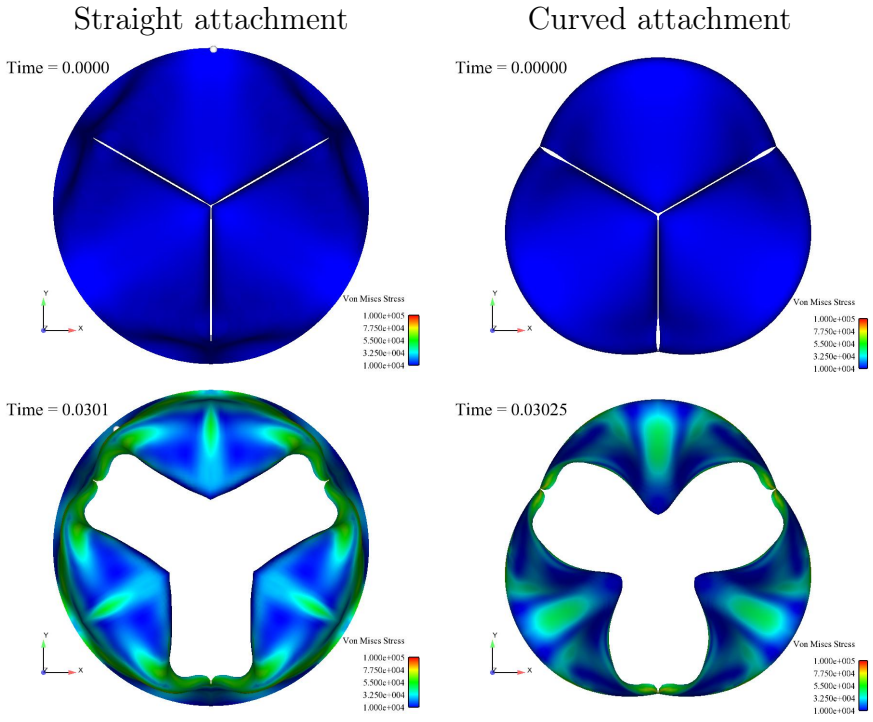

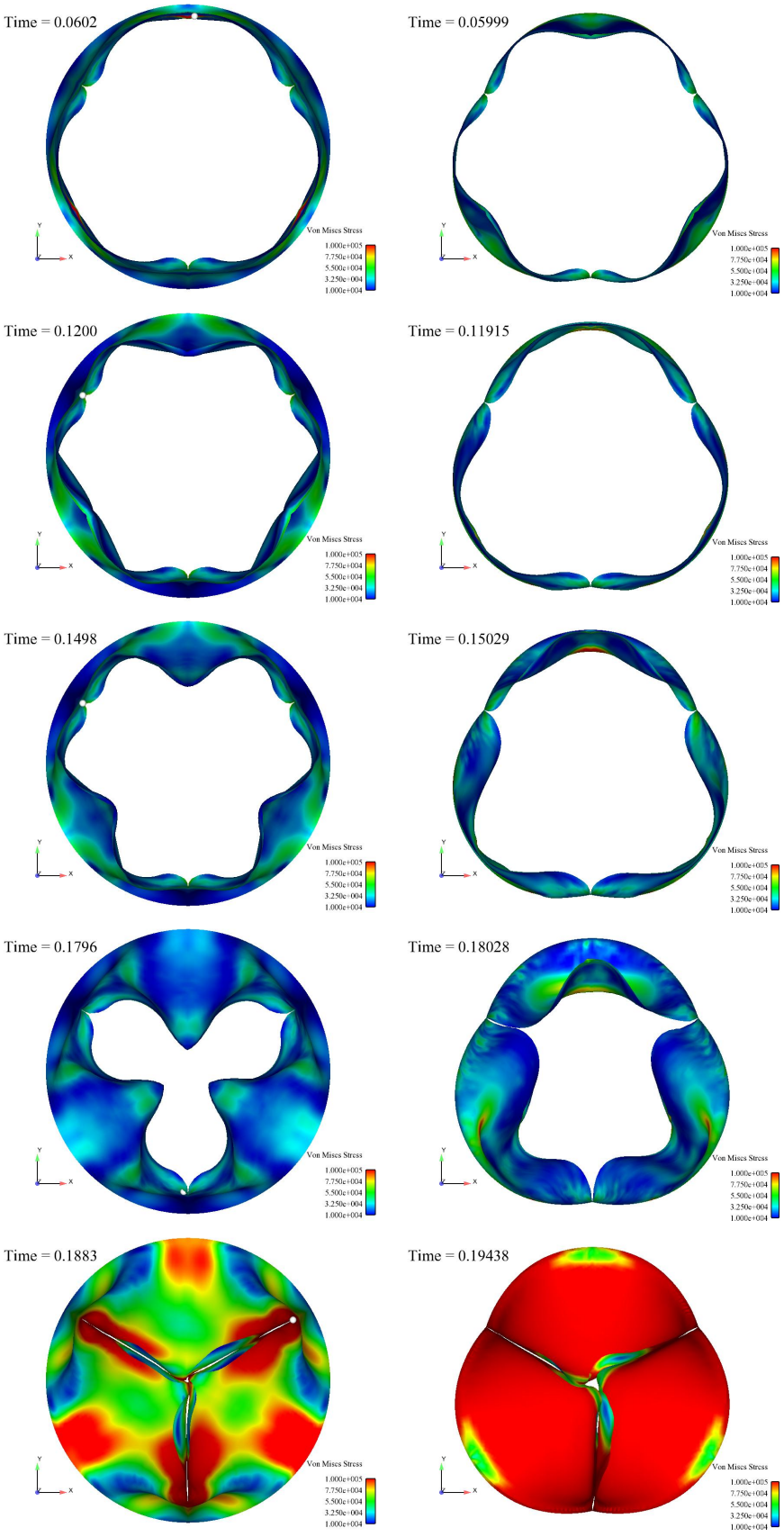

Figure 7.6: Opening and closing behavior of curved and straight valve

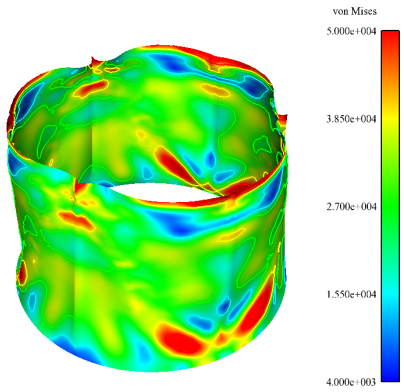

Figure 7.7: Von Mises stress: straight valve

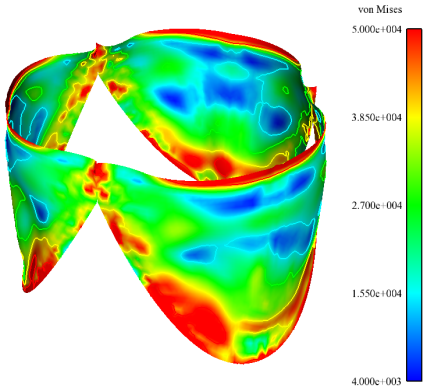

Figure 7.8: Von Mises stress: curved valve

Leaflet stresses

The maximum stresses during the opening of the valves are illustrated in Figures 7.7 and 7.8. Figure 7.9 shows a plot of the maximum Von Mises stress during the opening and closing phase. Figure 7.9 is not as insightful as the fringe plots and can be misleading, because stress concentrations occur (this is why Figure 7.9 is not "smooth"). It shows the maximum stress at a node in the model; not necessarily the same node as at the previous time step. The fringe plots of Figures 7.7 and 7.8 aid in the estimation of the maximum stress. Maximum stress in the straight valve is slightly higher at 65 kPa, compared to that of the curved valve which has a maximum stress of 56 kPa. Figure 7.9 does however show that in the curved valve, the higher stresses last longer, possibly due to an improved stress distribution in the straight valve due to its larger surface area.

7.4 Conclusion

From the simulation results, it can be concluded that there is no significant difference between the two valve designs, thus supporting both designs as viable options for the percutaneous valve. The straight valve naturally forms a curve during simulation, much like the curved valve, even though it is not attached in that manner. The folds that are created can clearly be seen in Figure 7.2. This shows that the curved shape is the desired shape and therefore this is also the shape of the native aortic valve. It is believed that the curved shape of

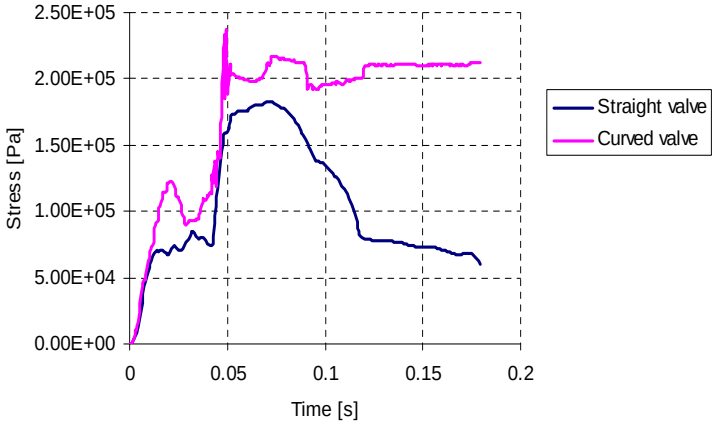

Figure 7.9: Maximum von Mises stress vs. time

a native leaflet, when combined with its aortic sinus, form an almost circular shape, which effectively distributes pressure across the leaflet during diastole [37].

Consideration must be given to the possibility that folds created in the straight valve, when in the closed position, can cause early fatigue due to elevated stresses. This can only be proven by comparing the two valve's stress related reactions by conducting a fatigue test in a pulse duplicator.

Chapter 8

Valve dilation

8.1 Introduction

Aortic valve incompetence due to dilation[1] is a common disorder and it can even be surgically reconstructed [49]. Aortic valve diameters vary from one individual or species to the next. As mentioned earlier, two different diameter valves were constructed, namely a 20 mm and 26 mm for implantation into sheep and humans, respectively. A major concern related to stented valve design is to establish what the effect of over- or under-dilation would be. Typically, dilation should not be more than 10% of the original design size.

Under dilation would not have such a significant effect on valve functioning compared to over-dilation, because the valve will still be able to close properly. Over-dilation will cause the leaflets to move in the radial direction, causing the valve to open up in the middle. Dilation of the valve root will cause valve insufficiency due to leakage [50]. This chapter will evaluate the effects of over- and under-dilation and also investigate the possibility to resolve the problem by increasing the leaflet free edge length (Lf).

8.2 Previous studies

Although no literature could be found regarding dilation of stented valves for percutaneous insertion, the dilation of the normal aortic valve has been investigated by several authors. Brewer *et al.* [51] was the first to describe aortic root

[1]Dilation is the act of stretching or enlarging an opening.

dilation at the commisural, as an essential part of leaflet opening. Thubrikar [37] studied the opening of the aortic valve using a marker fluoroscopy technique on native valves. These studies showed that the expansion of the aortic root and sinuses during systole assits in opening the leaflets. This expansion is however not possible in a stented valve (due to the presence of the stent) and the leaflets open purely due to a pressure difference between the ventricle and the aorta. Grande *et al.* [52] investigated the root dilation of the native aortic valve using FE models. They evaluated the relationships between root dilation, leaflet stress, strain and coaption. It was concluded that root dilation significantly increases leaflet stress and strain while it reduces coaption. More recently Lansac *et al.* [53] conducted a four-dimensional study on aortic root dynamics. Results showed that aortic root expansion follows a precise chronology during systole and the valve takes on a more cylindrical shape.

8.3 Simulation

In order to investigate dilation, two FE models of aortic valves were designed. The geometries of the two valves are described by the parameters in Table 5.1 in Section 5.4, with the only difference between the two being the leaflet free edge length (Lf). For the first valve, Lf was chosen with the normal length of 18 mm and for the second valve Lf was increased to 21 mm. This 16% increase in length was thought to be a reasonable maximum, because (as was shown in Chapter 4) a larger than necessary Lf value will result in a too large leaflet surface area. The simulations carried out were purely structural with pressure loads applied directly to the nodes.

Finite element model

Valve geometries were created, using a script file written by Dr. Michel Labrosse, from the University of Ottawa [45](with permission). The script reads the valve dimensions as input and then creates the geometry in Ansys. The geometry .igs file can then be imported into MSC.Patran. MSC.Patran was used as pre-processor and MSC.Dytran as a solver. The FE model of the leaflets, root and contact boundary is depicted in Figure 8.1. The element summary for the two valves is tabulated in Table 8.1. Four master-slave-node contact cards were

used; three for contact between the leaflets and one for contact between the valve root and the expanded rigid root. The material parameters are shown in Table 8.2

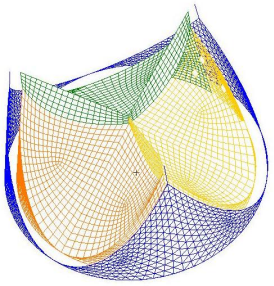

Figure 8.1: Valve with root contact boundary

Table 8.1: Element summary

	Valve 1: Xs=0.95 mm	Valve 2: Xs=2 mm
Belytschko-Lin-Tsay (Leaflet)	2400	2514
Belytschko-Lin-Tsay (Root)	1800	1794

Table 8.2: Material parameters

E_l [N/m^2]	$2 \cdot 10^6$
E_r [N/m^2]	$5 \cdot 10^6$
ν [-]	0.3
ρ_l [kg/m^3]	$1 \cdot 10^3$
t_l [mm]	0.2
t_r [mm]	0.4
ρ_f [kg/m^3]	$1.05 \cdot 10^3$
μ [Pa· s]	$3.57 \cdot 10^{-3}$

Simulation procedure

Figures 8.2 and 8.3 show the valve before and after dilation. The valves were expanded in the radial direction by applying a pressure load on the root area of the valve (green elements). The valves were expanded with 5%, 10% and

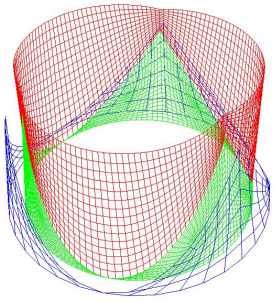

Figure 8.2: FE model before dilation

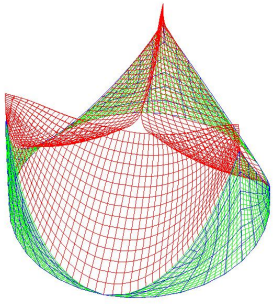

Figure 8.3: FE model after dilation

15% in the radial direction. To ensure full valve expansion to the desired diameter for each percentage dilation, replicas of the valve root were created (blue elements), but with the desired increase in diameter. These replica roots were then used as contact boundaries for the valve during the dilation simulation. For each valve, three replica roots had to be created. Figure 8.1 illustrates a valve with its contact boundary (replica root) for a 15% expansion.

A pressure of 50 Pa was applied to the leaflets (red elements) to close them after the expansion process. After leaflet closure, the centre gap can be visualised.

In order to simulate behaviour during under-dilation, the same procedure was followed as with the over-dilation, but instead of having a replica root with an increased diameter as contact boundary, a smaller diameter root was created. Only the valve with $Lf = 19\ mm$ was simulated for a 15% under-dilation.

8.4 Results

Over-dilation

By increasing the leaflet free edge length (Lf), the surface area of the leaflet is increased. The result of this dimensional change not only allowed improved coaption, but when valve dilation occurs, the larger coaption area brings about better leaflet closure. Figure 8.4 illustrates the dilation from left to right for a 5%, 10%, and 15% dilation respectively, with $Lf = 18.2$ mm. Figure 8.5 shows the dilation from left to right for a 5%, 10%, and 15% dilation respectively,

with $Lf = 21$ mm. As expected, dilation causes the valve to open in the middle, as can be seen in Figure 8.4(c). Figure 8.5(c) shows that by increasing the leaflet free edge length, this problem can be solved. When the centre holes of two valves are compared at a 15% expansion, the valve with $Lf = 21$ mm shows almost no hole as a result of an increased coaption surface.

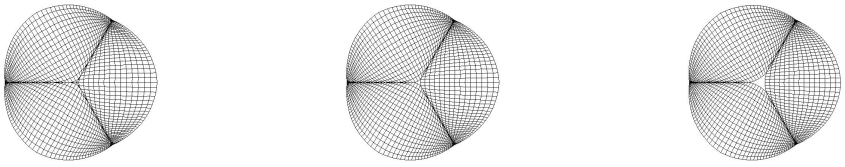

(a) 5% (b) 10% (c) 15%

Figure 8.4: Valve over-dilation with $Lf = 18.2$ mm

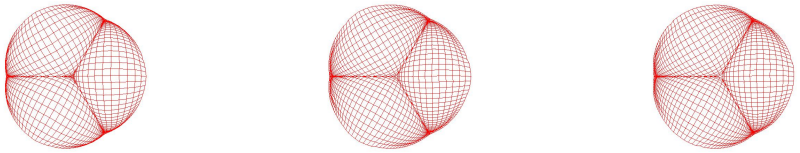

(a) 5% (b) 10% (c) 15%

Figure 8.5: Valve over-dilation with $Lf = 21$ mm

Under-dilation

Figure 8.6 illustrates the effect of under-dilation on valve closure. The figure is for a 15% under-dilation. As expected, over- and under-dilation have an opposite effect. With under-dilation, the leaflet surface area is too large, creating folds during the closing phase. However, due to the relatively low material stiffness, the leaflets still close. In the long run the folds might be a cause for concern, due to the fact that these are areas of increased stress.

8.5 Conclusion

The effect of over- or under-dilation on valve closure was examined in this chapter. In the ideal case, the aim would be to expand the valve to its design diameter, but this will not always be possible. For example, during animal

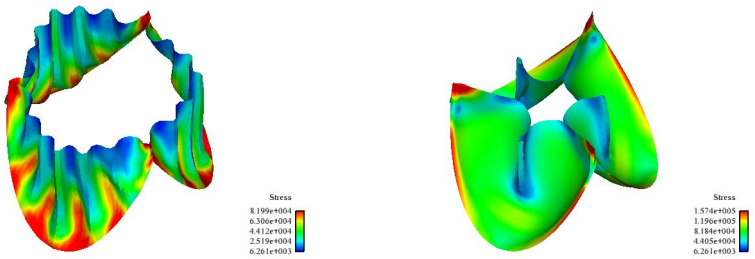

Figure 8.6: Effect of under-dilation

trials only a 19 mm valve will be available. However, the sheep aorta diameters might not be exactly 19 mm.

The over-dilation simulations show that, as expected, a hole is formed in the centre of the leaflets. Although this opening is relatively small in relation to the rest of the valve, it would cause the valve to leak. As demonstrated by the simulations, a possible solution would be to increase the leaflet free edge length (Lf). An increased Lf, although compensating for over-dilation, would have a negative impact on under-dilation.

Results for the under-dilation simulation show that valve behaviour is influenced. Decreasing Lf to ensure that the valve will function when under dilated is not an appropriate solution. This will simply cause the valve to leak when it is expanded to its normal diameter. Therefore, there is no immediate solution to the folds caused by under-dilation. The effect these folds have on valve fatigue should be examined in a pulse duplicator fatigue test; which is beyond the scope of this thesis.

Ideally the best solution would be to have a valve size for every possible scenario, which is practically impossible. Alternatively, a feasible solution would be to develop a range of valve sizes. Native valve diameters can be measured prior to the insertion of the new valve. With the availability of a range of valve sizes it would be best to use a slightly larger replacement valve (than the native valve diameter) and under dilating it, rather than using a too small replacement valve and over dilating it.

Chapter 9

In-vitro valve testing

9.1 Introduction

Testing prototype valves in a pulse duplicator is an essential first step to evaluate a valve's performance. For the purpose of collecting pressure and flow data along with high speed images, a pulse duplicator was therefore designed and manufactured. Appendix B discusses the pulse duplicator design and validation of a MATLAB model of the arterial tree. The pulse duplicator was designed specifically to study the heamodynamics of the valves and is not intended for fatigue testing (a different pulse duplicator for fatigue testing was designed by another student specifically for this purpose).

9.2 Prototypes

Two stented prototype valves were tested and compared to a commercial mechanical valve by St. Jude and a non-stented valve based on the geometry described in Chapter 5. The valves are depicted in Figure 9.1. Valve A is the non-stented prototype with leaflets made from un-treated bovine pericardium. Valve B has leaflets made from treated Kangaroo pericardium (treatment methods are confidential). Valve C has leaflets from un-treated bovine pericardium. Valve D is the St. Jude mechanical valve.

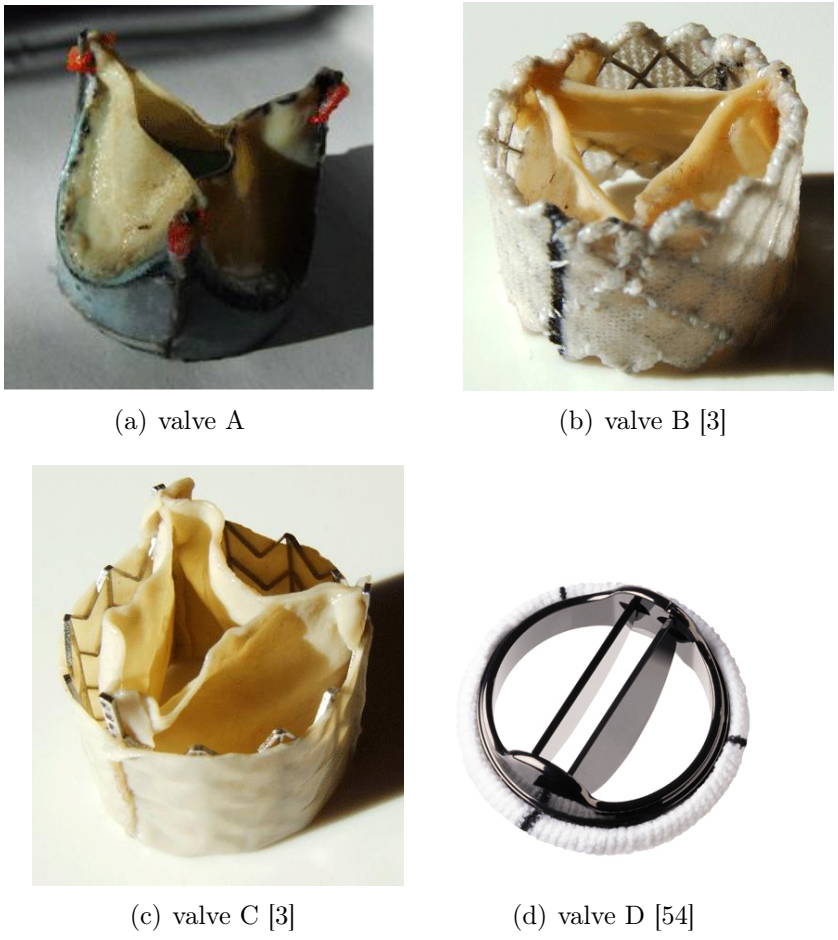

(a) valve A (b) valve B [3]

(c) valve C [3] (d) valve D [54]

Figure 9.1: Prototype valves

9.3 Test setup

The test setup was a pulse duplicator based on the 4-element Windkessel model which simulates the arterial tree. A detailed discussion of the pulse duplicator design and its validation are presented in Appendix B.

All valves were tested with a 1 Hz pulse with a stroke volume of ±63 ml. This created a cardiac output of 3.78 l/min with a heart rate of 60 bpm. 60 bpm is slightly less than the normal heart rate of 72 bpm. The decreased heart rate was due to two reasons: Firstly, the camera used for motion capturing had a frame rate of 75 fps, thus a slower heart rate was necessary to capture the leaflet movement. Secondly, the pulse duplicator had to be operated manually, time was kept with a metronome and constant stroke volume was maintained

by measuring piston travel. All of this was easier to achieve at 1 Hz. Water was used as a testing medium. Although the viscosity of blood is 2-3 times more than that of water it was found that water as a test medium is sufficient when comparing different valves [55].

9.4 Measurements

The hydrodynamic performance of the prototype valves under pulsatile flow can be expressed by the following quantities [55]:

1. Stenocity, which can be described as the mean systolic pressure difference over the valve as an indication for the resistance to opening.
2. Closure volume, i.e. the amount of backflow during valve closure.
3. Leakage volume, i.e. the amount of backflow through the closed valve.
4. Energy losses due to stenocity and regurgitant flows. The sum of the closure flow and the leakage is called regurgitation of the valve.
5. Opening and closing behaviour.

Pressure measurements

Pressure measurements were conducted with pressure transducers. The calibration of these transducers is described in Appendix G. The pressure transducers were amplified with a Spider 8 bridge amplifier and data acquisition was performed with the Catman software. The sampling rate was 50 Hz with the average data taken over ten cycles to conduct further processing.

The mean systolic pressure difference was calculated by subtracting aortic pressure from ventricle pressure and then by calculating the mean between two consecutive differential zero values.

Flow measurements

Flow measurements were done by means of an orifice plate as described in Appendix G. Figure 9.2 illustrates the definition of closure and leakage volume used for further calculations. The same type of pressure transducers used for

measuring the aortic and ventricular pressure, were used in the orifice plate. In order to calculate flow, the differential pressure from the orifice plate was fitted to the pressure-flow calibration curve in Appendix G.

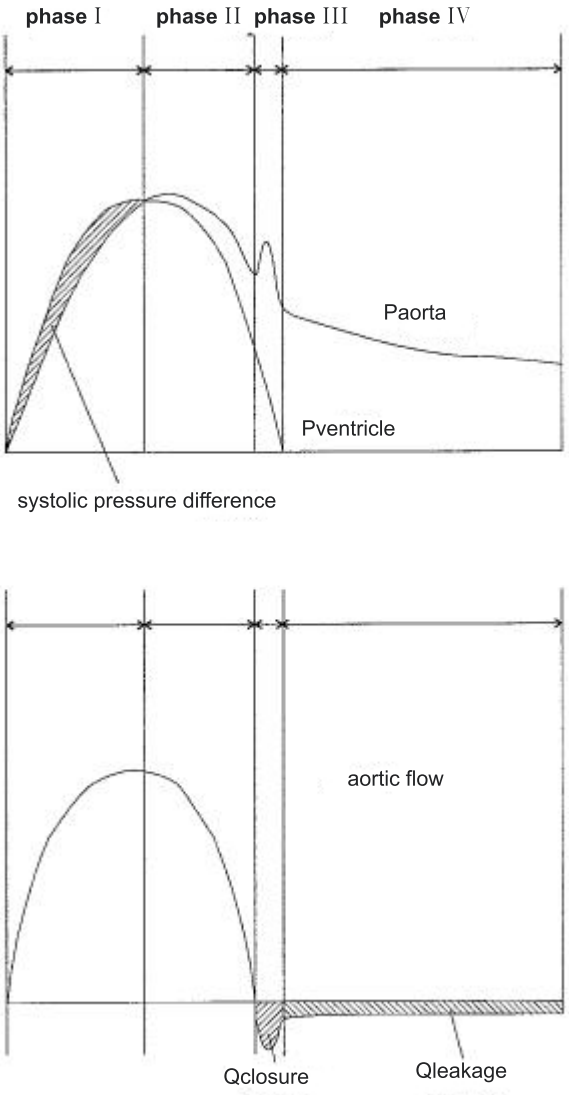

Figure 9.2: Phases of the cardiac cycle [55]

Energy losses

Energy losses through the valve can be calculated according to the energy loss due to the pressure gradient over the valve during systole and the energy loss

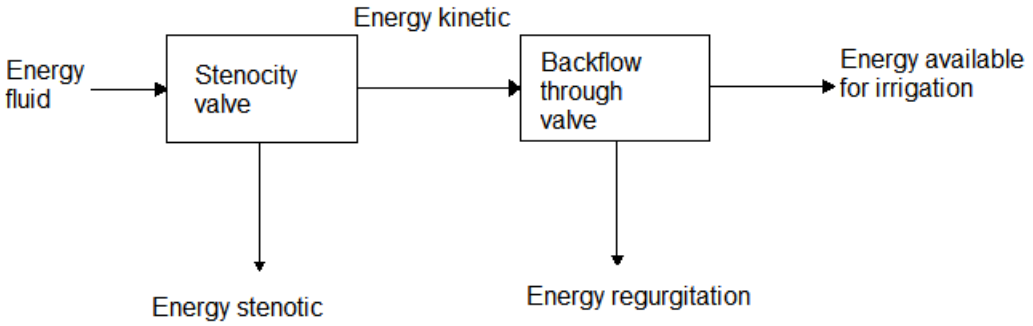

Figure 9.3: Energy flow diagram [55]

due to the regurgitant volumes during diastole. The pressure gradient over the valve during systole, is caused by the valve's stenotic behaviour and is therefore called *stenotic energy loss*.

Calculating energy loss for a valve is a helpful way to characterize overall valve efficiency, and is a good option for valve comparison.

In order to calculate energy loss, the cardiac cycle must be divided into four characteristic phases as illustrated in Figure 9.2. The diagram in Figure 9.3 demonstrates the decrease in fluid energy due to valve losses.

The test fluid contains a certain amount of kinetic energy as well as energy dissipated by the valve. Kinetic energy can be determined by simultaneously measuring the flow and pressure during systole, i.e. phases I and II. The fluid kinetic energy is given as follows [55]:

$$\text{Energy kinetic} = \int_{I+II} Q\, p_{ao}\, dt \tag{9.1}$$

Here Q is the aortic flow and p_{ao} the aortic pressure. It is assumed that leaflet deformations are elastic and they do not cause energy loss. The stenotic energy of the valve can be expressed with [55]:

$$\text{Energy Stenotic Phase I} = \int_{I} Q\, \Delta p\, dt \tag{9.2}$$

$$\text{Energy Stenotic Phase II} = \left[\int_{II} Q\, dt \,/\, \int_{I} Q\, dt\right] \times \int_{I} Q\, \Delta p\, dt \tag{9.3}$$

The total amount of energy in the test fluid can then be calculated with [55]:

$$\begin{aligned}\text{Energy fluid} = \text{Energy Kinetic} + \text{Energy Stenotic Phase I} + \\ + \text{Energy Stenotic Phase II}\end{aligned} \tag{9.4}$$

The regurgitant energy losses can be calculated with [55]:

$$\text{Energy Regurgitation} = \int_{III+IV} |Q|\ p_{ao}\, dt \tag{9.5}$$

The efficiency of the valve can then be expressed by [55]:

$$\text{Efficiency Valve} = \frac{\text{Energy available for irrigation of arterial tree}}{\text{Energy fluid}} \tag{9.6}$$

$$\text{Efficiency Valve} = \frac{\text{Energy fluid} - (\text{Energy stenotic} + \text{Energy regurgitation})}{\text{Energy fluid}} \tag{9.7}$$

The energy loss caused by the stenocity of the valve can be expressed by [55]:

$$\text{Stenocity} = \frac{\text{Energy stenotic}}{\text{Energy fluid}} \tag{9.8}$$

The energy loss caused by the regurgitation through the valve can be expressed by [55]:

$$\text{Regurgitation} = \frac{\text{Energy regurgitation}}{\text{Energy fluid}} \tag{9.9}$$

Visualisation

A high speed image sensor was used to record the opening and closing of the valves. The sensor used was a DVT smart sensor which has a maximum speed of 75 fps.

9.5 Results

The pressure and flow curves for the various valves used in the pulsatile test are presented in Appendix E.

Figure 9.4 depicts the mean systolic pressure difference across the valves, which is also an indication of valve resistance or stenocity. The tilting disk (D) has the lowest pressure loss, with $dP = 400$ Pa. Prototypes A, B and C all have a slightly higher mean pressure.

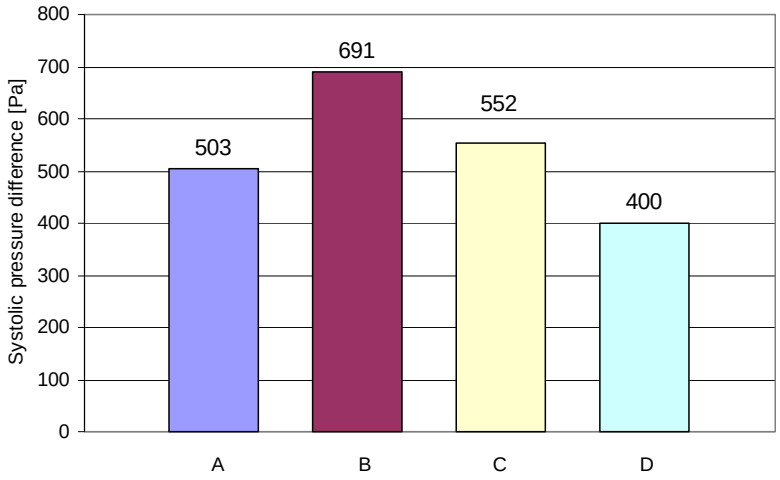

Figure 9.4: Mean systolic pressure difference over prototype valves

Figure 9.5 depicts the regurgitation as a percentage of stroke volume for the different valves. The figure also illustrates the large effect closure and leakage volume have on total regurgitation. Prototype A only shows a 1% leakage volume and a 2% closure volume. The two stented valves show higher regurgitation with 16% being the highest for prototype B. The ISO requirement is that 19 mm diameter valves should have a regurgitant fraction of $\leq 10\%$. Prototypes B and C are thus 6% and 1% over the required limit.

Figure 9.6 illustrates the efficiency of the valves, as well as regurgitant and stenotic fractions. The graph clearly indicates that valve regurgitation have the biggest effect on valve efficiency. All four of the valves have a high efficiency rating. Spee [55] calculated the efficiency of a Bjork-Shiley mechanical valve

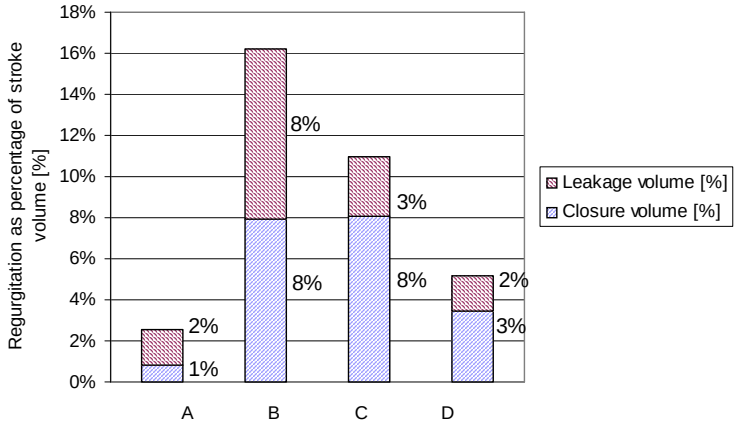

Figure 9.5: Regurgitation through prototype valves as a percentage of stroke volume

to be 0.83. Other valves tested by Spee [55] showed efficiency ratings of over 0.9.

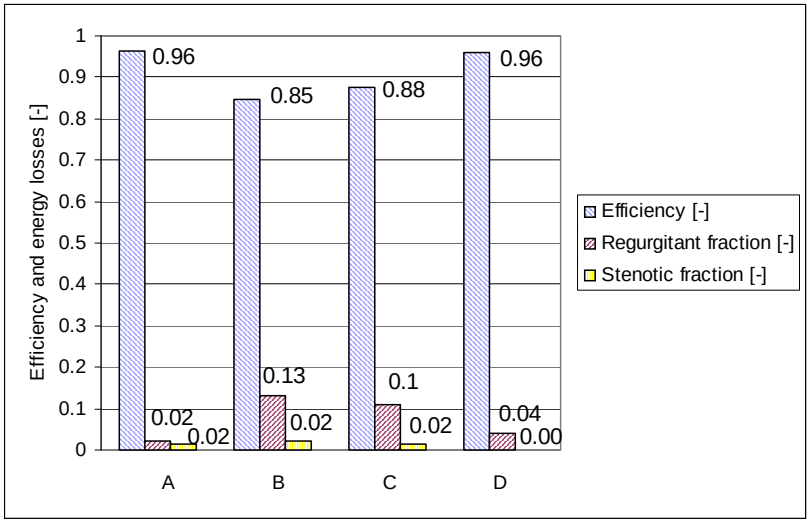

Figure 9.6: Efficiency and energy losses of prototype valves

9.6 Conclusion

The pulse duplicator proved to be successful in testing the prototype valves. High quality pressure and flow measurements were taken along with images of the valve during the opening and closing cycle. The pressure and flow data were used to characterize the valves regarding their respective efficiencies. The two stented prototypes showed efficiencies of over 86% and the stentless prototype had the same efficiency as the St. Jude valve with a value of 96%.

Manufacturing the stented valves to the exact required specifications proved to be a very complicated process. Great difficulty was experienced when handling the material, with the added problem that leaflets had to be manually stitched onto the stent. Constructing a symmetrical valve was thus very problematic.

With all the problem areas taken into consideration, the author strongly believes that further manufacturing experience will bring about stented valve performance measuring up to that of commercial valves (for example the St. Jude mechanical valve). The main reason is that, at present manufacturing difficulties are resulting in prototype valves that are not symmetrical and prototype geometry that does not accurately reflect the intended design geometry.

Chapter 10

Conclusion and recommendations

10.1 Conclusion

The design and manufacturing of a stented aortic valve is an extremely time and energy consuming process which requires a great number of resources.

This thesis forms part of two other studies with the main objective to develop a stented valve suitable for percutaneous implantation. A valve of this kind will enable interventionists to perform less invasive procedures, eliminating many of the risks involved with open heart surgery. It would also be a more economical procedure, reaching an extensive group of individuals in dire need of an aortic valve replacement.

This thesis contributes to the design of the valve as part of the replacement prosthesis. Although a detailed literature study and review was done on the aortic valve, the main focus of this thesis was to dynamically simulate valve behaviour. More specifically, valve behaviour was simulated taken into consideration the complex interaction between the blood and the valve itself.

In order to explain the operating procedure for FSI simulation, a simple plate model was constructed. ALE and the general fast coupling method were used for model simulation. After comparing simulation results it was concluded that the general fast coupling method is a more suitable method to use for aortic valve simulations.

It was hypothesized that leaflet geometry will have the largest effect on valve performance. The author therefore attempted to investigate the effect of geometrical characteristics on valve performance. Various valve geometries were created and simulated. The results and findings were then applied to find

possible solutions in order to optimise valve performance.

Results showed that haemodynamic behaviour was greatly affected by different geometrical characteristics. An optimal leaflet geometry will bring about enhanced leaflet performance. Optimal geometries were established for a 19 mm and a 25 mm valve by optimising various parameters found in the literature.

There are two methods to attach leaflets to a stent. One method places the leaflets in a "straight" orientation whereas the second method creates a more natural "curved" orientation. Both scenarios were simulated and the results showed almost no significant difference. When simulated, the straight valve adopted a curved shape, suggesting that the curved shape is the more natural orientation.

Forces acting between the leaflet and stent were investigated by means of simulation. Identifying forces that act between the leaflets and stent can be a helpful tool, enabling the stent designer to effectively load the stent during simulations. The force simulations were done with both the explicit MSC.Dytran- and implicit MSC.Marc solvers.

Valve dilation was studied to find solutions for problems relating to over- and under-dilation. Results showed that by increasing the leaflet coaption area (closure area), the problem of over-dilation could be solved. Coaption area can be increased by increasing the leaflet free edge length (Lf). This however increases the possibility of unwanted folds forming on the leaflets during under-dilation. It was concluded that a range of valves might be necessary and that it will be better for a valve to operate under its designed diameter than above it. With a range of valves available and by measuring the recipient's native valve diameter, a slightly bigger replacement valve should thus be inserted instead of over dilating a small replacement valve.

Leaflet stiffness and thickness were investigated to determine their influence on valve behaviour. Results indicated that thickness has a more significant effect on valve behaviour than stiffness. These results are concurrent with results found in the literature.

A pulse duplicator was designed and manufactured to study the in-vitro behaviour of the prototype valves. Flow and pressure data obtained from the pulse duplicator were used to calculate valve efficiencies and therefore enabling a characterisation of the valves. Some stented valves were found to be 88%

efficient, which is a positive result when taking into a consideration that a commercial mechanical valve (like the St. Jude valve) was found to have an efficiency of 96%.

A stentless prototype valve was also manufactured based on the optimal geometrical principles. The efficiency of this valve was calculated to be 96%.

Great difficulty was experienced during the manufacturing of both the stentless and stented prototypes, with the latter being much more complex. A steep learning curve is involved in the manufacturing of stented valves, with very thin biomaterials increasing the complexity. The author strongly believes that further experience in stented valve manufacturing will facilitate the production of stented valves with efficiencies measuring up to those of commercial prosthetic valves.

The thesis was completed with the validation of an FSI simulation using MSC.Dytran (see Appendix A). This was achieved by taking data from the pulse duplicator, applying it as boundary conditions in the simulation and then comparing the results. The rapid valve opening time (RVOT), rapid valve closing time (RVCT), ejection time (ET) and velocity output from the simulation was compared to the measured data and a good correlation was found. To the author's knowledge this is the first validated FSI simulation of an aortic valve simulated with MSC.Dytran.

10.2 Recommendation

Although many aspects of percutaneous valve design were discussed throughout the thesis, the magnitude of a project like this one allows for much more work to be done in the future:

- Extensive fatigue testing is necessary before animal trails can start.
- Non-linear leaflet material and its influence on valve behaviour should be further investigated.
- Valve over- and under-dilation should be tested in-vitro.

List of References

[1] Ye, J., Cheung, A., Lichtenstein, S., Pasupati, S., Carere, R., Thompson, C., Sinhal, A. and Webb, J.: Six-month outcome of transapical transcatheter aortic valve replacement in the initial seven patients. *European Journal of Cardiothoracic Surgery*, vol. 31, p. 16, 2007.

[2] Esterhuyse, A.: *Structural Design and Analysis of a Stent for Implimentation in a Percutaneous Aortic Heart Valve*. Master's thesis, University of Stellenbosch, 2008.

[3] Smuts, A.: *Design of tissue leaflets for a percutaneous aortic heart valve*. Master's thesis, University of Stellenbosch, 2008.

[4] Carmody, C., Burriesci, G., Howard, I. and Patterson E, A.: An approach to the simulation of fluid-structure interaction in the aortic valve. *Journal of Biomechanics*, vol. 39, pp. 158–169, 2006.

[5] Chikwe, J., Walther, A. and Pepper, J.: The surgical management of aortic valve disease. *British Journal of Cardiology*, vol. 6, pp. 453–461, 2003.

[6] Otto, C., Lind, B., Kitzman, D., Gersh, B. and Siscovick, D.: Association of aortic-valve sclerosis with cardiovascular mortality and morbidity in the elderly. *The New England Journal of Medicine*, vol. 341, pp. 142–147, 1999.

[7] lung, B., Baron, G., Butchart, E., Delahaye, F., Gohlke-Barwolf, C., Levang, O., Tornos, P., Vanoverschelde, J., Vermeer, F., Boersma, E., Ravaud, P. and Vahanian, A.: A prospective survey of patients with valvular heart disease in europe: The euro heart survey on valvular heart disease. *European Heart Journal*, vol. 24, pp. 1231–1243, 2003.

[8] Fann, J., Chronos, N., Rowe, S., Michiels, R., Lyons, B., Leon, M. and Kaplan, A.: Evolving strategies for the treatment of valvular heart disease: Preclinical

and clinical pathways for percutaneous aortic valve replacement. *Catheterization and Cardiovascular Interventions*, vol. 71, pp. 434–440, 2008.

[9] Artunes, M.: Off-pump aortic valve replacement with catheter-mounted valved stents: Is the future already here? *European Journal of Cardio-thoracic Surgery*, vol. 31, pp. 1–3, 2007.

[10] Hufnagel, C., Harvey, W., Rabil, P. and Mcdermott, T.: The surgical correction of aortic insufficiency. *Surgery*, vol. 35, pp. 673–683, 1954.

[11] Harken, D., Soroff, H., Taylor, W., Lefemine, A., Gupta, S. and Lunzer, S.: Partial and complete prosthesis in aortic insufficiency. *Journal of Thoracic Cardiovascular Surgery*, vol. 40, pp. 744–762, 1960.

[12] Anderson, H.: Transluminal catheter implanted prosthetic heart valves. *International Journal of Angiology*, vol. 7, pp. 102–106, 1998.

[13] Bonhoeffer, P., Boudjemline, Y., Saliba, Z., Merckx, J., Aggoun, Y., Bonnet, D., Acar, P., Le Bidois, J., Sidi, D. and Kachaner, J.: Percutaneous replacement of pulmonary valve in a right-ventricle to pulmonary-artery prosthetic conduit with valve dysfunction. *Lancet*, vol. 365, pp. 1403–1405, 2000.

[14] Cribier, A., Eltchaninoff, H., Bash, A., Boenstein, N., Tron, C., Bauer, F., Derumeaux, G., Anselme, F., Laborde, F. and Leon, M.: Percutaneous transcatheter implantation of an aortic valve prosthesis for calcific aortic stenosis: First human case description. *Circulation*, vol. 106, pp. 3006–3008, 2002.

[15] YNHH Health Library, May 2008.
Available at: http://www.ynhh.org/cardiac/heart/interior_heart_anatomy.jpg

[16] Heartlab.Robberts, December 2007.
Available at: http://heartlab.robarts.ca/scratch/valve.geometry.gif

[17] Wikimedia, June 2008.
Available at: http://upload.wikimedia.org/wikipedia/commons/5/5b/

[18] Heartlab.Robberts, December 2007.
Available at: http://heartlab.robarts.ca/scratch/cusp.anatomy.gif

[19] Heartlab.Robberts, December 2007.
Available at: http://heartlab.robarts.ca/scratch/cross.section.gif

[20] De Hart, J.: *Fluid-Structure Interaction in the Aortic valve: a three-dimensional computational analysis*. Ph.D. thesis, University of Eindhoven, 2002.

[21] Brodsky, A, M.: Percutaneous approaches to aortic valve replacement. The Society for Cardiovascular Angiography and Interventions, December 2004.

[22] Attmann, T., Quaden, R., Francis, R., Konig, C., Cremer, J. and Lutter, G.: Percutaneous heart valve replacement: histology and calcification characteristics of biological valved stents in juvenile sheep. *Cardiovascular Pathology*, vol. 16, pp. 165–170, 2007.

[23] Catalyst eNews, Volume 3 Issue 5, June 2008.
Available at: http://my.clevelandclinic.org/Documents/Giving/Cleveland%20Clinic.pdf

[24] Dewey, T., Walther, T., Doss, M., Brown, D., Ryan, W., Svensson, L., Mihaljevic, T., Hambrecht, R., Schuler, G., Wimmer-Greinecker, G., Mohr, F. and Mack, M.: Transapical aortic valve implantation: An animal feasibility study. *The Society of Thoracic Surgery*, vol. 82, pp. 110–116, 2006.

[25] Walther, T., Dewey, T., Wimmer-Greinecker, G., Doss, M., Hambrecht, R., Schuler, G., Mohr, F. and Mack, M.: Transapical approach for sutureless stent-fixed aortic valve implantation: experimantal results. *European Journal of Cardio-thoracic Surgery*, vol. 29, pp. 703–708, 2006.

[26] CoreValve, April 2008.
Available at: http://corevalve.com

[27] Edwards Lifesciences, April 2008.
Available at: http://www.edwards.com

[28] Li, J., Luo, X. and Kuang, Z.: A nonlinear anisotropic model for porcine aortic heart valves. *Journal of Biomechanics*, vol. 34, pp. 1279–1289, 2001.

[29] van Loon, R.: *A 3D method for for modeling the fluid-structure interaction in heart valves*. Ph.D. thesis, University of Eindhoven, 2005.

[30] Ranga, A., Bouchot, O., Mongrain, R., Ugolini, P. and Cartier, R.: Computational simulations of the aortic valve validated by imaging data: evaluation of valve-sparing techniques. *Interactive Cardio Vascular and Thoracic Surgery*, vol. 5, pp. 373–378, 2006.

[31] De Hart, J., Cacciola, G., Schreurs, P. and Peters, G.: A three-dimensional analysis of a fibre-reinforced aortic valve prosthesis. *Journal of Biomechanics*, vol. 31, pp. 629–638, 1998.

[32] Cacciola, G., Peters, G. and Schreurs, P.: A three-dimensional mechanical analysis of a stentless fibre-reinforced aortic valve prosthesis. *Journal of Biomechanics*, vol. 33, pp. 521–530, 2000.

[33] Arcidiacono, G., Corvi, A. and Severi, T.: Functional analysis of bioprosthetic heart valves. *Journal of Biomechanics*, vol. 38, pp. 1483–1490, 2005.

[34] *Dytran 2007 r1: Users Guide*, 2007.

[35] *Dytran 2007 r1: Theory Manual*, 2007.

[36] Esteq Engineering, September 2008.
Available at: http://engineering.esteq.com/

[37] Thubrikar, M.: *The Aortic Valve*. 1st edn. CRC Press, Inc, 1990.

[38] van Loon, R., Anderson, P., van de Vosse, F. and Sherwin, S.: Comparison of various fluid-structure interaction methods for deformable bodies. *Computers and Structures*, vol. 85, pp. 833–843, 2007.

[39] Ranga, A., Mongrain, R., Biadilah, Y. and Cartier, R.: A compliant fea model of the aortic valve. In: *12th IFToMM World Congress, Besancon, France*. 2007.

[40] Watton, P., Luo, X., Wang, X., Bernacca, G., Molley, P. and Wheatley, D.: Dynamic modelling of prothetic chorded mitral valves using the immersed boundary method. *Journal of Biomechanics*, vol. 40, pp. 613–626, 2007.

[41] Wiley encyclopedia of biomedical engineering volume 1. John Wiley & Sons Inc, Hoboken, New Jersey, 2006.

[42] Garcia, D., Barenburg, P., Pibarot, P., Dekker, A., van der Veen, F., Maessen, J., Dumesnil, J. and Durand, L.: A ventricular-vascular coupling model in presence of aortic stenosis. *American Journal of Physiology - Heart an Circulatory Physiology*, vol. 288, pp. H1874–H1884, 2005.

[43] Leyh, R., Schmidke, C., Sievers, H. and Yacoub, M.: Opening and closing characteristics of the aortic valve after different types of valve-preserving surgery. *Circulation*, vol. 100, pp. 2153–2160, 1999.

[44] *Cardiovascular implants - Cardiac valve prosthesis.* International Standard ISO 5840, 4th edn, 2005.

[45] Labrosse, M., Carsten, J., Francis, R. and Thubrikar, M.: Geometric modeling of functional trileaflet aortic valves: Development and clinical applications. *Journal of Biomechanics*, vol. 39, pp. 2665–2672, 2006.

[46] Microsoft, October 2008.
Available at: http://support.microsoft.com/kb/214115

[47] *Marc 2007 r1, Volume B: Element Library*, 2007.

[48] Martini, F. and Bartholomew, E.: *Essentials of Anatomy & Physiology.* 4th edn. Pearson Education Inc, 2007.

[49] Grande-Allen, K., Cochron, R., Reinhall, P. and Kunzelman, K.: Finite-element analysis of aortic valve-sparing: Influence of graft shape and stiffness. *IEEE TRANSACTIONS ON BIOMEDICAL ENGINEERING*, vol. 48, pp. 647–659, 2001.

[50] Underwood, M., Khoury, G., Deronck, D., Glineur, D. and Dion, R.: The aortic root: structure, function, and surgical reconstruction. *Heart*, vol. 83, pp. 376–380, 2000.

[51] Brewer, R., Deck, J., Capati, B. and Nolan, S.: The dynamic aortic root. its role in aortic valve function. *Journal of Thoracic Cardiovascular Surgery*, vol. 72, pp. 413–417, 1976.

[52] Grande, K., Cochron, R., Reinhall, P. and Kunzelman, K.: Mechanisms of aortic valve incompentence: Finite element modeling of aortic root dilation. *Annuals of Thoracic Surgery*, vol. 69, pp. 1851–1857, 2000.

[53] Lansac, E., Lim, H., Shomura, Y., Lim, K., Rice, N., Goetz, W., Acar, C. and Duran, C.: A four-dimensional study of the aortic root dynamics. *European Journal of Cardio-thoracic Surgery*, vol. 22, pp. 497–503, 2002.

[54] St. Jude Medical, July 2008.
Available at: http://www.sjmprofessional.com/EN-US/ProductLibrary/Pages/Regent-Valve-HP-Series-Standard-Valve.aspx

[55] Spee, I.: In-vitro testing of trileaflet heart valve prosthesis. Tech. Rep., Technical University of Eindhoven, 1997.

[56] Davila, J., Trout, R., Sunner, J. and Glover, R.: A simple mechanical pulse duplicator for cinematography of cardiac valves in action. *Annals of Surgery*, vol. 143, pp. 544–551, 1956.

[57] Oura, M., Kobayashi, N., Takeda, S., Iwasaki, K. and Umezu, M.: Development of the compact mock circulation system and the new flow-cell model for pulse spectrophotometry. In: *30th Annual International IEEE EMBS Conference*. 2008.

[58] Fries, R., Graeter, T., Aicher, D., Reul, H. Schmitz, C., Böhm, M. and Scä fers, H.: In vitro comparison of valve-preserving aortic replacement. *The Journal of Thoracic and Cardiovascular Surgery*, vol. 132, pp. 32–37, 2006.

[59] Bröckner, K.: Improved design of a pulse duplicator to study the natural heart valves. *Chest*, vol. 51, pp. 11–17, 1967.

[60] HLAVÁČ, M.: Windkessel model analysis in Matlab. Tech. Rep., Department of Biomedical Engineering, FEEC, BUT, 1998.

[61] Bernacca, G., O'Connor, B., Williams, D. and Wheatley, D.: Hydrodynamic function of polyurethane prosthetic heart valves: influences of Young's modulus and leaflet thickness. *Biomaterials*, vol. 23, pp. 45–50, 2002.

[62] Bernacca, G., Mackay, T., Wilkinson, R. and Wheatley, D.: Calcification and fatigue failure in a polyurethane heart valve. *Biomaterials*, vol. 16, pp. 279–285, 1995.

[63] Bernacca, G., Mackay, T., Wilkinson, R. and Wheatley, D.: Polyurethane heart valves: Fatigue failure, calcification, and polyurethane structure. *Journal of Biomedical Materials Research*, vol. 34, pp. 371–379, 1997.

[64] Efunda, July 2008.
Available at: www.efunda.com

Appendix A

FSI validation

A.1 Introduction

To give the FSI simulation results more credibility, a FSI validation was necessary. FSI validation can be achieved by building a prototype valve and comparing the test results to the simulation results.

In the test setup the differential pressure across the prototype valve was recorded simultaneously with flow data and high speed images of the valve. The differential pressure from the test setup was then applied as a boundary condition in the FSI simulation. A FSI simulation with pressure boundaries has a velocity boundary output as result.

The obtained velocity data from the test setup was compared to the measured velocity. Due to the nature of the leaflet material, difficulty was experienced during manufacturing of a symmetrical valve. The end result being that the prototype did not open and close symmetrical, the high speed images was thus used to compare the RVOT, RVCT and ET rather than to compare actual leaflet deformation.

A.2 Prototype

Figure A.1 illustrates the prototype valve. The leaflet material consists of untreated Bovine pericardium and the root is cut out from a 19 mm internal diameter plastic tube. It was very difficult to build a prototype valve to the exact same specifications as the simulated valve, for the following reasons:

- The prototype had to be build manually, so human errors and inaccuracy playes a role.
- The small dimensions of the prototype (19 mm diameter) increases manufacturing difficulty.
- The type of leaflet material used, Bovine pericardium, was very difficult to handle.

Figure A.1: Prototype

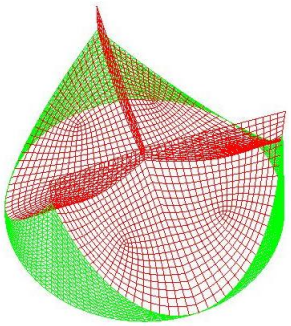

Figure A.2: FE model for validation

A.3 Simulation parameters

Figure A.2 demonstrates the leaflets and root of the valve model, created for the FSI simulation. The fluid domain consists of 256 000 solid elements and the leaflets consists of 2400 shell elements. Table A.1 tabulates the simulation parameters. The non-linear true stress-strain curve in Figure A.3 was used for the material elasticity model. This stress-strain relationship is for Bovine pericardium in the matrix ($X11$) direction, as discussed in Appendix F.

The differential pressure across the valve and flow rate through the valve were measured simultaneously in a pulse duplicator. The differential pressure depicted in Figure A.4 was then used as a boundary condition for the FSI simulation.

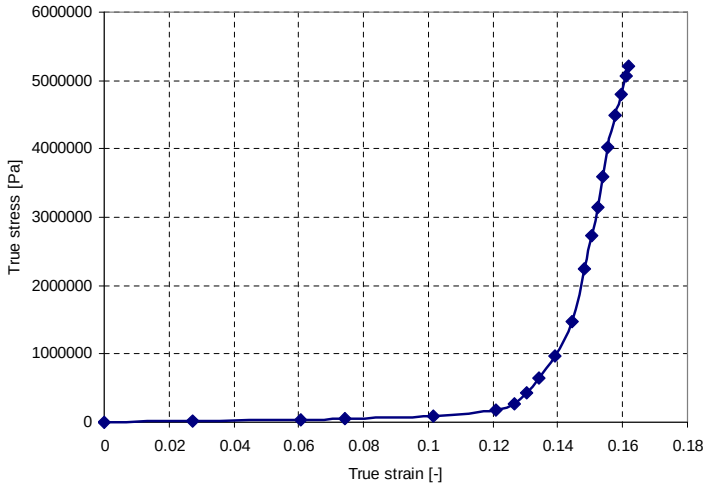

Figure A.3: True stress vs. strain [3]

Table A.1: Simulation parameters

ν [-]	0.3
ρ_l [kg/m^3]	$1 \cdot 10^3$
t_l [mm]	0.2
ρ_f [kg/m^3]	$1.05 \cdot 10^3$
μ [Pa·s]	$1.0 \cdot 10^{-3}$

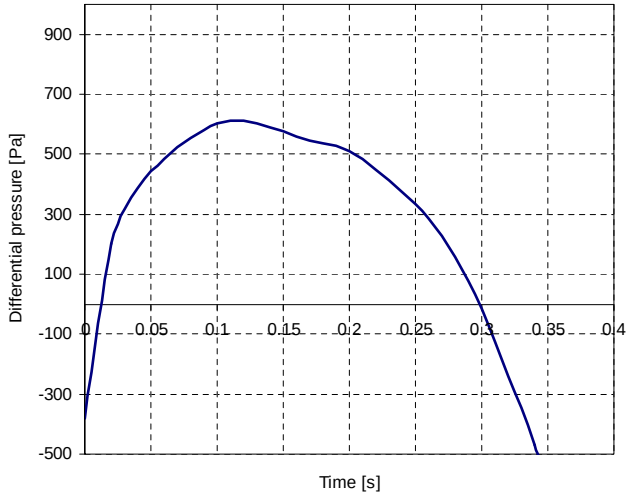

Figure A.4: Differential pressure boundary curve

A.4 Results

Figure A.5 shows the axial velocity from the FSI simulation as well as the measured velocity. The measured and peak velocities are almost similar: 0.62 m/s for the measured and 0.68 m/s for the simulation velocity. The simulation curve shows some oscillation when it shoots past zero, but this effect is not captured with the pressure sensors because of the low sampling frequency. The sampling frequency for the pressure sensors is 50 Hz compared to a "sampling frequency" of ± 10 MHz for a average time step of $0.1 \cdot 10{-}6$ sec for the simulation. The RVOT, RVCT an ET are compared in Table A.2. Figure A.6 shows the simulation results (right hand side) accompanied by the photos from the pulse duplicator (left hand side), for the specified time interval.

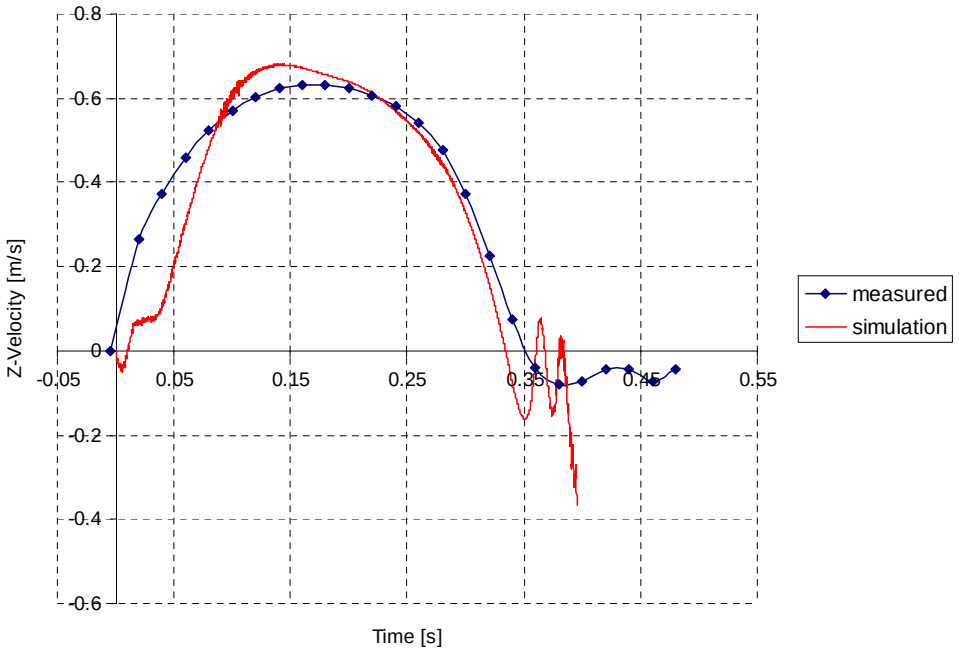

Figure A.5: Simulation and measured axial velocity

Table A.2: Opening and closing characteristics

	Measured	Simulation
RVOT [ms]	91	82
RVCT [ms]	91	90
ET [ms]	351	332

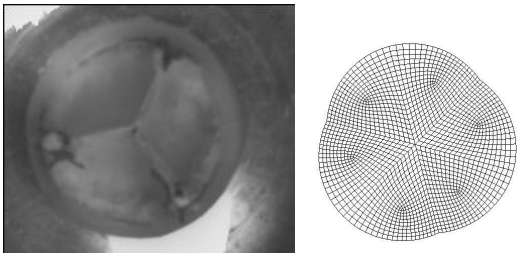

(a) Time = 0 ms

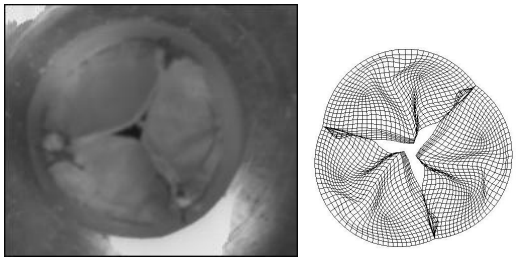

(b) Time = 39 ms

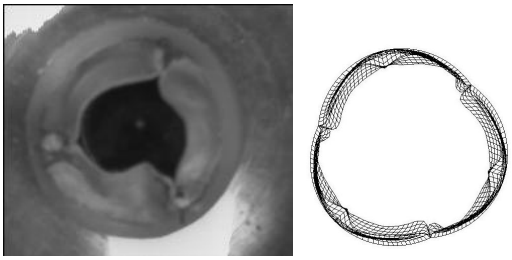

(c) Time = 78 ms

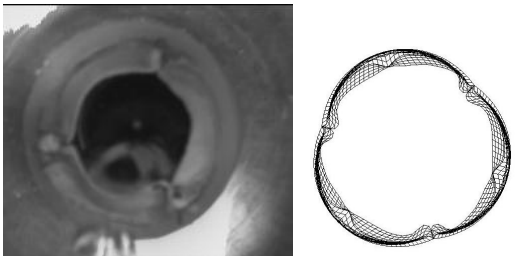

(d) Time = 118 ms

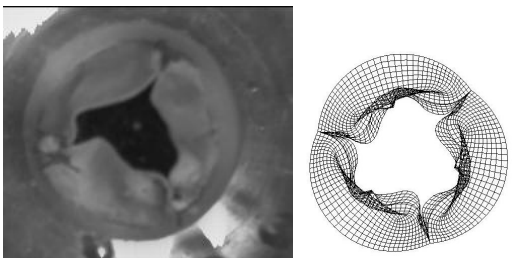

(a) Time = 351 ms

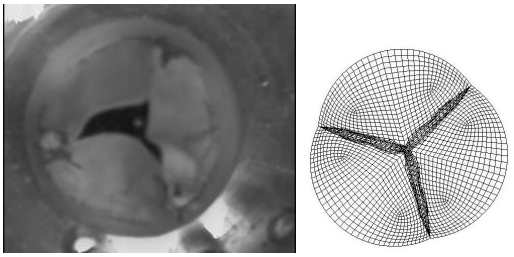

(b) Time = 360 ms

Figure A.6: Visualization

A.5 Conclusion

Exact simulation of the valve would really be difficult to achieve. Too many factors, from which material behaviour stands out, influence results. As mentioned previously, it is very difficult to manufacture the valve precisely as intended in the design. Results throughout this thesis proved that the slightest change in geometry will have an influence on valve performance.

A good correlation was found between flow velocity results from the simulation and test setup. The simulation had a RVOT that is 10% less than that of the prototype valve and a RVCT of 1% less. The ET of the prototype is 5% more compared to the simulated value. These values become clearer when one compares the opening and closing photos with the simulation results. The prototype takes a little longer to open and close than the simulated valve.

Apart from a few small discrepancies, the results from the simulations actually compare very well with that of the prototype valve. To the author's knowledge this is the first validated FSI simulation of an aortic valve with the use of MSC.Dytran.

Appendix B

Pulse duplicator design and validation

B.1 Design of a simple pulse duplicator

In-vitro experiments in a pulse duplicator are an important phase in the design of any heart valve substitute. The pulse duplicator enables researchers to study the physiological behaviour of the valve. It is therefore critical that the pulse duplicator must simulate the cardiac cycle and arterial tree as closely as possible. In other words, the pressure waves and flow curves produced by the heart, must be approximated as closely as possible by the machine.

McMillan [56] first showed the usefulness of using cinematography to study valvular motion. From there it became a standard procedure to test heart valves in vitro due to the difficulties of doing it in-vivo. Many different designs exist today and are used in the fields of research and by prosthetic heart valve companies, for example Core Valve and Edwards Lifesciences [55; 57; 58; 59].

The aim of this section was to design and build a simple pulse duplicator. The idea was to keep the design as uncomplicated as possible due to time and financial constraints. The specifications of the pulse duplicator can be summarized as follows:

- Simulate the left ventricle and arterial tree as closely as possible.
- Allow clear visibility of the aortic valve area for easy haemodynamc studying.

- Minimize manufacturing cost and time by using off the shelf components.
- Must be manually operated with automation a future possibility.

Model of the pulse duplicator

In order to develop a pulse duplicator, a clear understanding of the left ventricle and arterial tree function in mathematical terms was needed. The arterial tree and left ventricle can easily be described by a Winkessel model. 2-element, 3-element and 4-element Windkessel models are shown in figures B.1, B.2 and B.3 respectively. The differential equations for the models are given in Equations B.1 - B.3 which can be solved for the 2-element, 3-element and 4-element models respectively. The system of differential equations can easily be solved with the use of SIMULINK [60] or with one of the differential equation solver methods in MATLAB. The equations where solved using Adams's method (ODE113) in MATLAB.

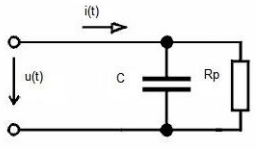

Figure B.1: 2WM

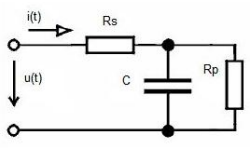

Figure B.2: 3WM

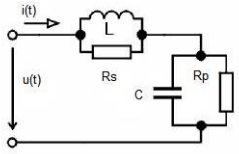

Figure B.3: 4WM

$$i_1(t) = \frac{u(t)}{Rp} + C\frac{du(t)}{dt} \tag{B.1}$$

$$i_1(t) = \frac{u_c(t)}{R_p} + C\frac{du_c(t)}{dt} \tag{B.2}$$

$$\begin{aligned} \frac{du_c(t)}{dt} &= -\frac{1}{R_pC}u_c(t) + \frac{1}{C}i_1(t) \\ \frac{di_L(t)}{dt} &= -\frac{R_c}{L}i_L(t) + \frac{R_c}{L}i_1(t) \end{aligned} \tag{B.3}$$

Pulse duplicator model validation

Figure B.4 illustrates the pulse duplicator after manufacturing. The main components are:

Figure B.4: Pulse duplicator

- A: High speed image sensor
- B: Valve test section
- C: Orifice plate
- D: Mitral valve mounting section
- E: Piston pump
- F: Gate valve for peripheric resistance

- G: Ball valve for characteristic resistance
- H: Compliance chamber

The flow in the system was measured using an orifice plate with equally spaced pressure taps. The calibration data for the orifice plate and the pressure sensors can be seen in Appendix G.

To calculate the compliance in the chamber, it was assumed that the air expands and compresses adiabaticaly. The change in air volume can be measured on the chamber itself and the change in pressure can be measured by means of the pressure sensors. For the setup as shown in Figure B.4, the change in pressure was measured as $dP = 15000$ Pa and the change in volume as $V = 2.51 \cdot 10^{-5}\text{m}^3$. The compliance can then be calculated with Equation B.4.

$$C = \frac{\Delta V}{\Delta p} \tag{B.4}$$

The inertia of the fluid can be described with Equation B.5 with $\rho = 10^3$ kg/m^3 the density of the water and $r = 10$ mm, $l = 600$ mm the radius and length of the test tube respectively:

$$L = \frac{\rho l}{\pi r^2} \tag{B.5}$$

The characteristic resistance Rc was estimated as $1.0\ 10^{11}$ N·s/m^5 [55]. The peripheric resistance Rp can be measured under steady flow conditions as the head loss over the peripheric valve. Table B.1 shows the parameters used for the validation.

Table B.1: Windkessel parameters

C [m^5/N]	$1.67 \cdot 10^{-9}$
L [kg/m^4]	$1.91 \cdot 10^{6}$
Rp [N·s/m^5]	$4.265 \cdot 10^{8}$
Rc [N·s/m^5]	$1.0 \cdot 10^{11}$

For the setup in Figure B.4 and the parameters in Table B.1, the pressure drop across the orifice plate and the valve, were measured simultaneously. The flow was then calculated using the orifice calibration curve in Appendix G. The converted flow curve was then used as input to the MATLAB model. Figure B.5 shows the flow curve recorded in the pulse duplicator and used as an input

to the MATLAB model. The negative area of the curve is caused by leakage through the valve. The measured aortic pressure was also compared with the aortic pressure output of the Windkesssel models. It can be seen in the figure how closely the 2 and 4-element Windkessel models approximate the actual pressure.

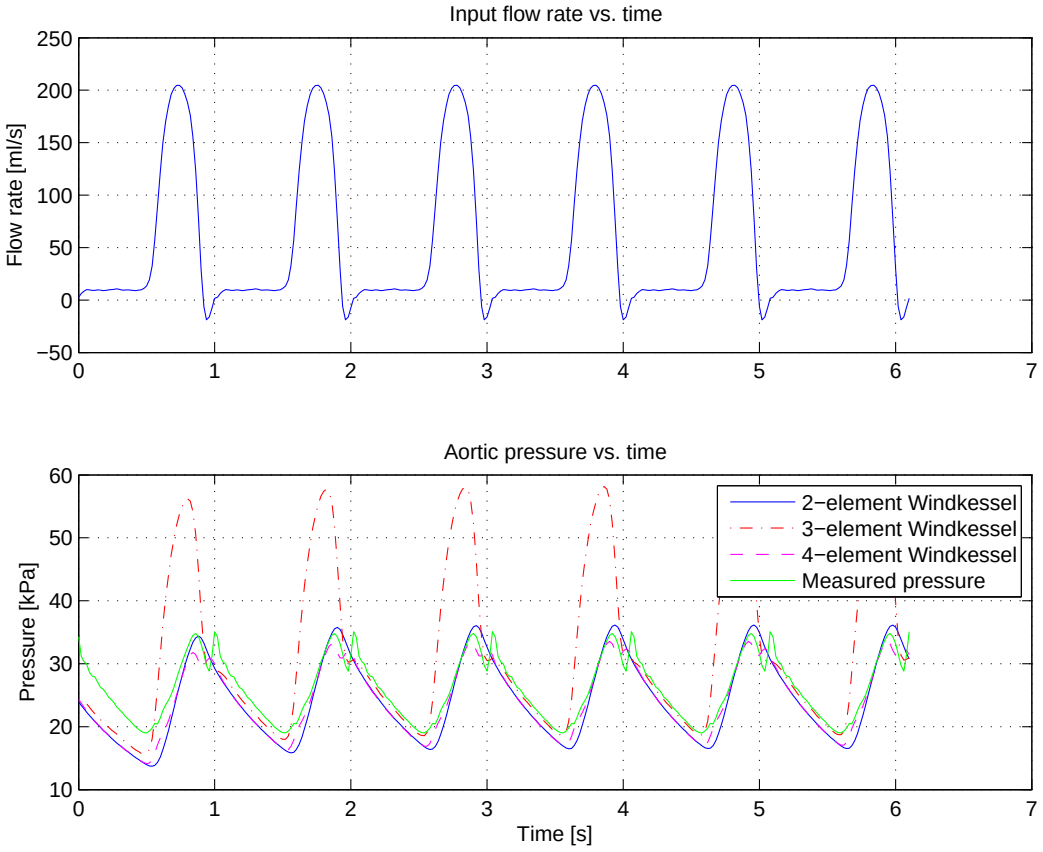

Figure B.5: Pulse duplicator validation

B.2 Influence of afterload

Afterload are the parameters that give the aortic pressure curve its characteristic shape. By changing the variables in a pulse duplicator, the curve shape can be changed. Figures B.6 - B.9 demonstrates the effect each of the variables on the curve have.

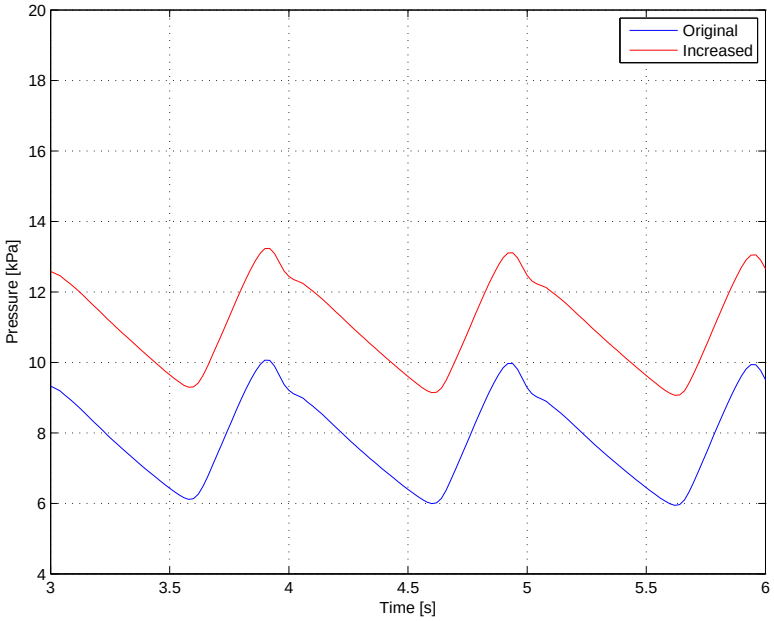

Figure B.6: Increased peripheric resistance Rp

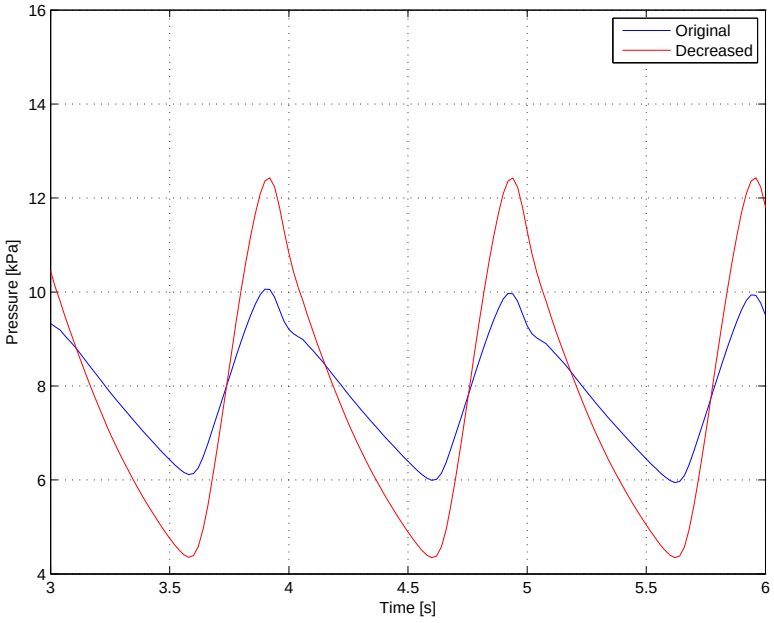

Figure B.7: Decreased compliance C

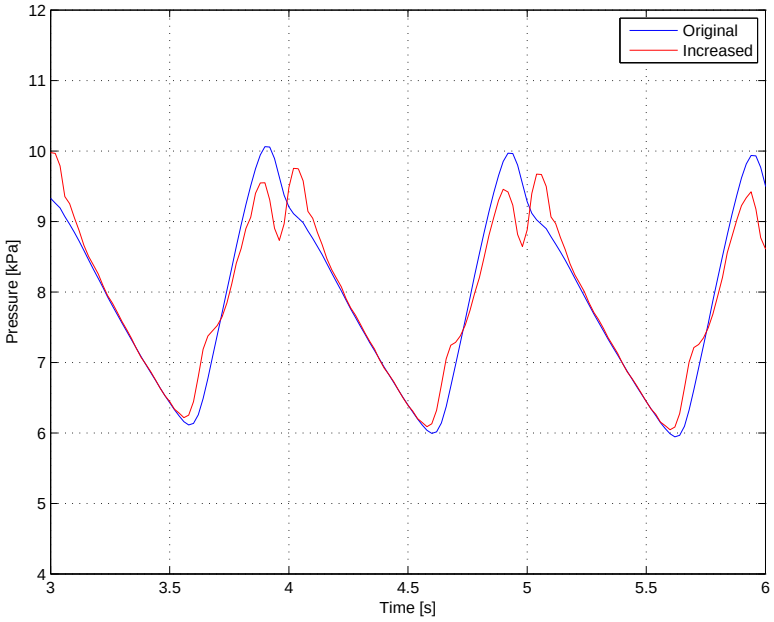

Figure B.8: Increased characteristic resistance Rc

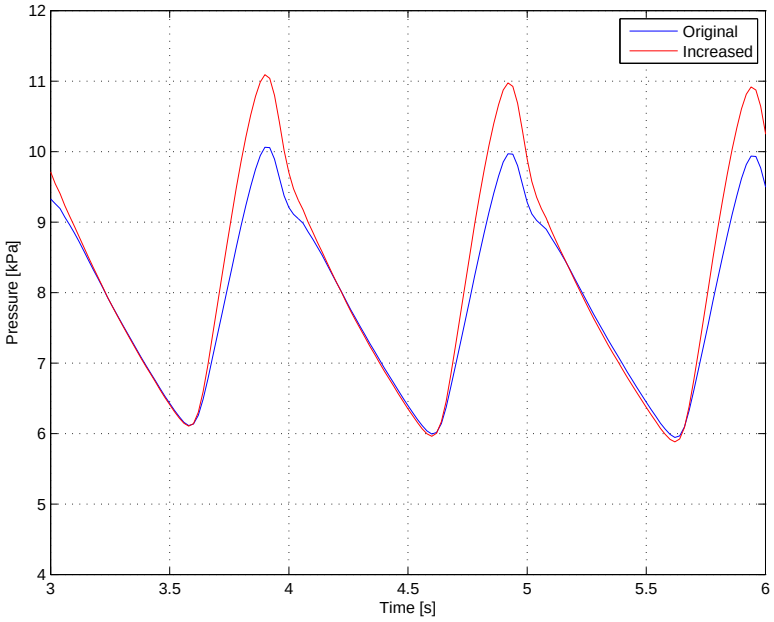

Figure B.9: Increased fluid inertia L

B.3 Conclusion and recommendations

A pulse duplicator was successfully modelled, designed and manufactured. For the purpose of using the pulse duplicator to study the opening and closing of the valves, this pulse duplicator was sufficient. The pressures recorded across the valve can be used as an input to an FSI simulation. The flow computed from the pressure difference across the orifice plate can also be used as an input for an FSI simulation.

Unfortunately the duplicator could only work at pressures of 200 mmHg over 160 mmHg, much higher than normal physiological pressures of 120 mmHg over 80 mmHg. Total resistance in the duplicator was found to be too high, due to the small diameter (20 mm) tubing used during manufacturing.

In order to make a more physiological realistic duplicator it is recommended that tubing with a larger diameter be used.

As mentioned, for the purpose of studying the opening and closing behaviour of the valve, the pulse duplicator proved to be successful. The reason being that both the valve and the orifice plate work with differential pressures and they were thus not affected by the elevated pressures in the duplicator.

Appendix C

Model sensitivity

Although many parameters can be varied for an FSI analysis, it was found that two of the most important factors are the damping of the global stiffness matrix, and the size of the Euler elements. Others factors include hourglass damping, element type, artificial viscosity, etc.

C.1 The effect of Euler element size

The goal of this study was to vary Euler or fluid element size in a FSI model and then compare the total reaction force measured on the valve leaflets. This study consisted of five cases each with a different element size. For the study the leaflets of the valve was set to be a rigid material. By setting the material to be rigid one would be able to obtain the total reaction force acting on the centre of gravity of the leaflet. This was then also the result that was compared between the different simulations. This setup allows one to only change the Euler mesh size, while keeping the other parameters the same. A pressure of 26 kPa was applied as a step function to the top boundary of the Euler mesh, and the bottom boundary was set to 0 kPa. The difference in pressure causes the fluid to flow from the normally outflow boundary to the normally inflow boundary, in other words creating reverse flow.

Figures C.1 to C.5 illustrates the leaflet from above with the accompanying Euler mesh and the number of Euler elements per case.

Figures C.6 shows the total reaction force for each case. Due to a very rough mesh, case 1 does not converge. All the other cases converge, but with different values. Results from case 4 and case 5 are very similar, showing that

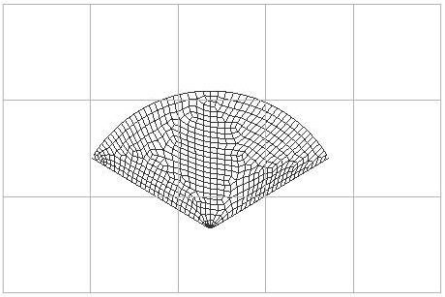

Figure C.1: Case 1: 5x3x5 = 75 elements

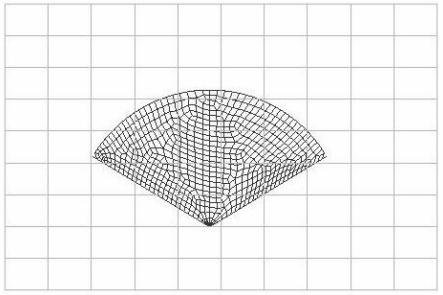

Figure C.2: Case 2: 10x9x10 = 900 elements

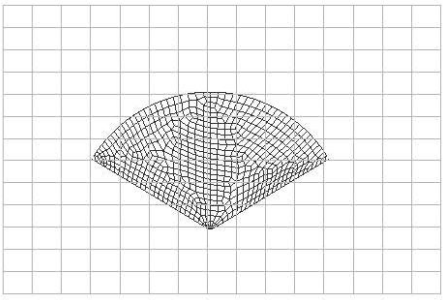

Figure C.3: Case 3: 15x13x15 = 292 elements

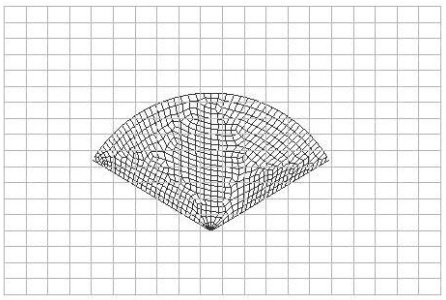

Figure C.4: Case 4: 20x18x20 = 7200 elements

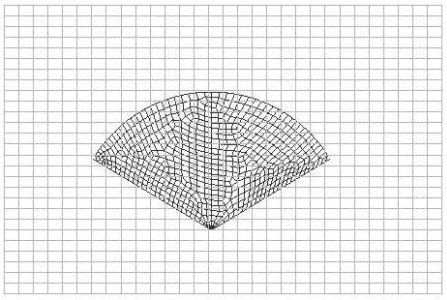

Figure C.5: Case 5: 30x27x30 = 24300 elements

the smaller mesh size converges, but with an increase in CPU time. Therefore when meshing, a decision should be made based on the most important factor for the particular simulation, i.e. availability of time or the desire for accurate results, with the latter being the obvious choice in almost every case.

Case 5 showed some oscillations at the beginning of the analysis, this was due to the fact that the fluid was initially at rest and then subjected to a step

input at the inflow boundary. This can be avoided by increasing the pressure gradually from zero instead of using a step input.

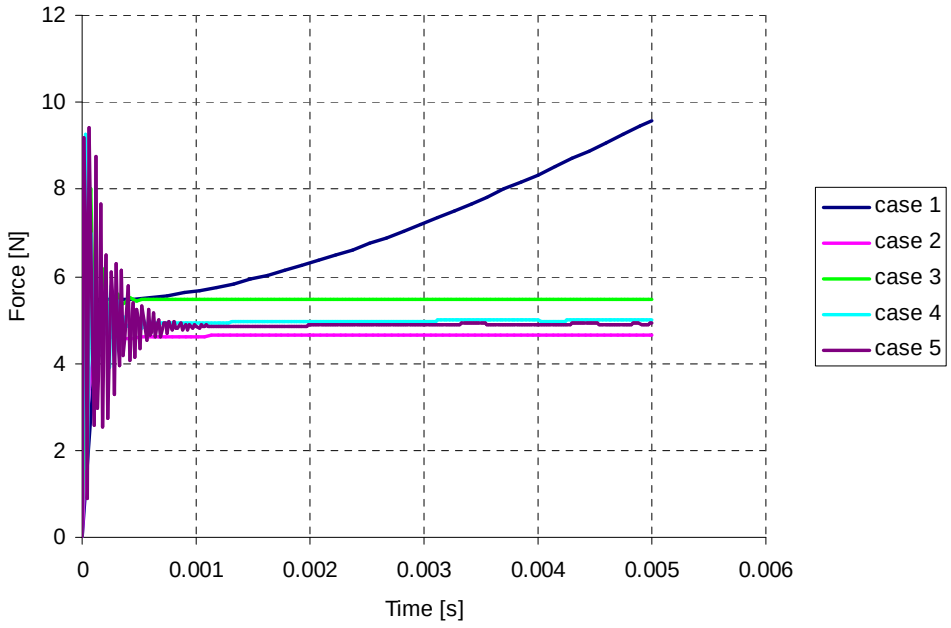

Figure C.6: Total reaction force

C.2 The effect of damping the global stiffness matrix

Damping is used to find the steady-state part of a dynamic solution to a transient response [35]. Light damping of the structure is sometimes necessary to avoid resonance. The damping is based on a mass-spring-damper system. The equation of motion reads [35]:

$$M \cdot a^n + C \cdot v^n + F_{int}^n = F_{ext}^n \tag{C.1}$$

Where C is:

$$C = \frac{2\beta}{\Delta t} M \tag{C.2}$$

In Equation C.2, β is the factor that can be changed to increase or decrease damping.

For the investigation, the same valve and identical parameters were used every time. Only the damping coefficient, β, was changed. Figure C.7 illustrates the opening and closing differences for a damping coefficient of 0.001, 0.002, 0.0035 and 0.005. Although the difference is not significant, damping does cause the valve to open slower, and once it has been opened, to close slower. Figure C.8 shows the strain energy density curves of the leaflets for the four cases.

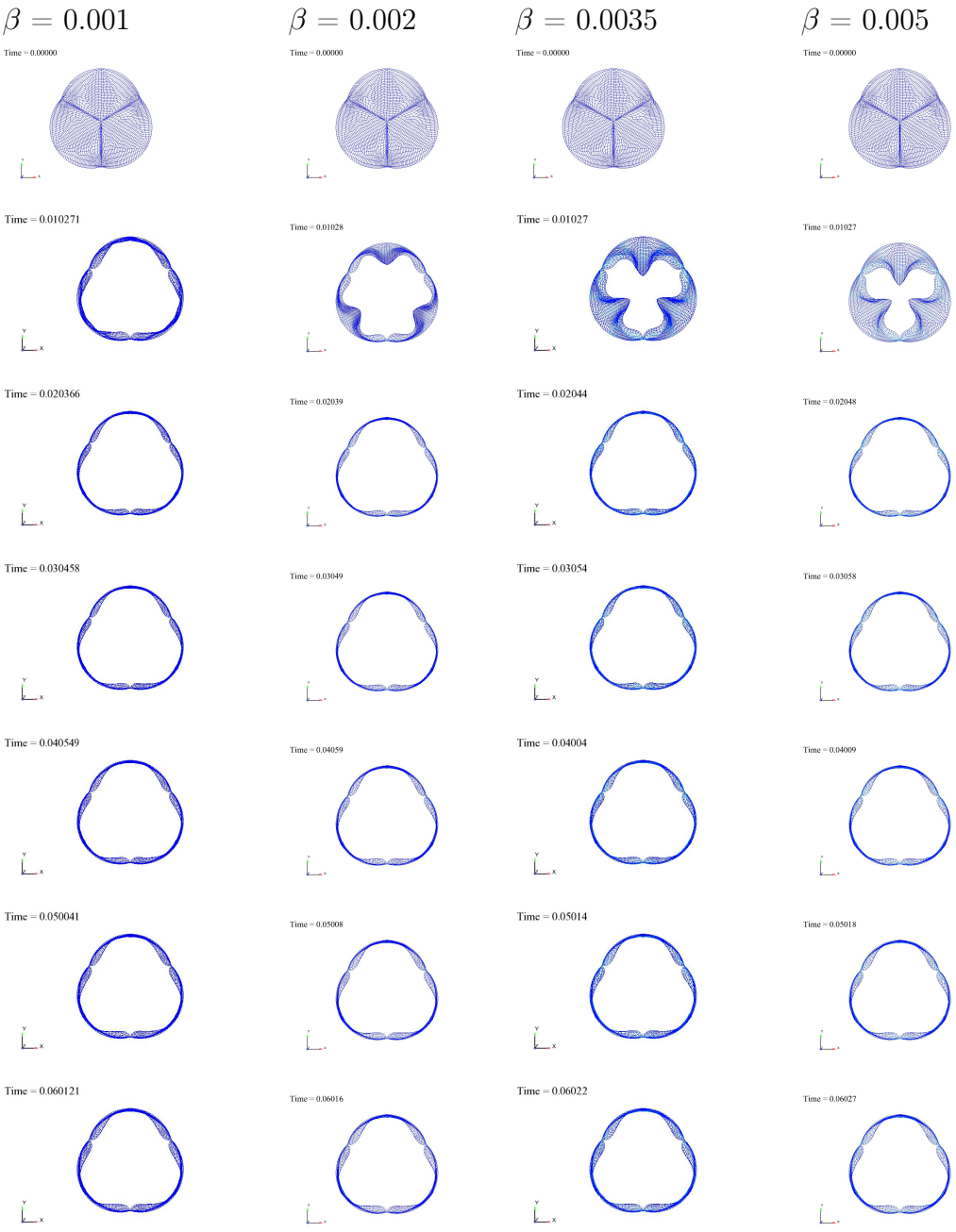
$\beta = 0.001$
$\beta = 0.002$
$\beta = 0.0035$
$\beta = 0.005$
Time = 0.00000
Time = 0.00000
Time = 0.00000
Time = 0.00000
Time = 0.010271
Time = 0.01028
Time = 0.01027
Time = 0.01027
Time = 0.020366
Time = 0.02039
Time = 0.02044
Time = 0.02048
Time = 0.030458
Time = 0.03049
Time = 0.03054
Time = 0.03058
Time = 0.040549
Time = 0.04059
Time = 0.04004
Time = 0.04009
Time = 0.050041
Time = 0.05008
Time = 0.05014
Time = 0.05018
Time = 0.060121
Time = 0.06016
Time = 0.06022
Time = 0.06027

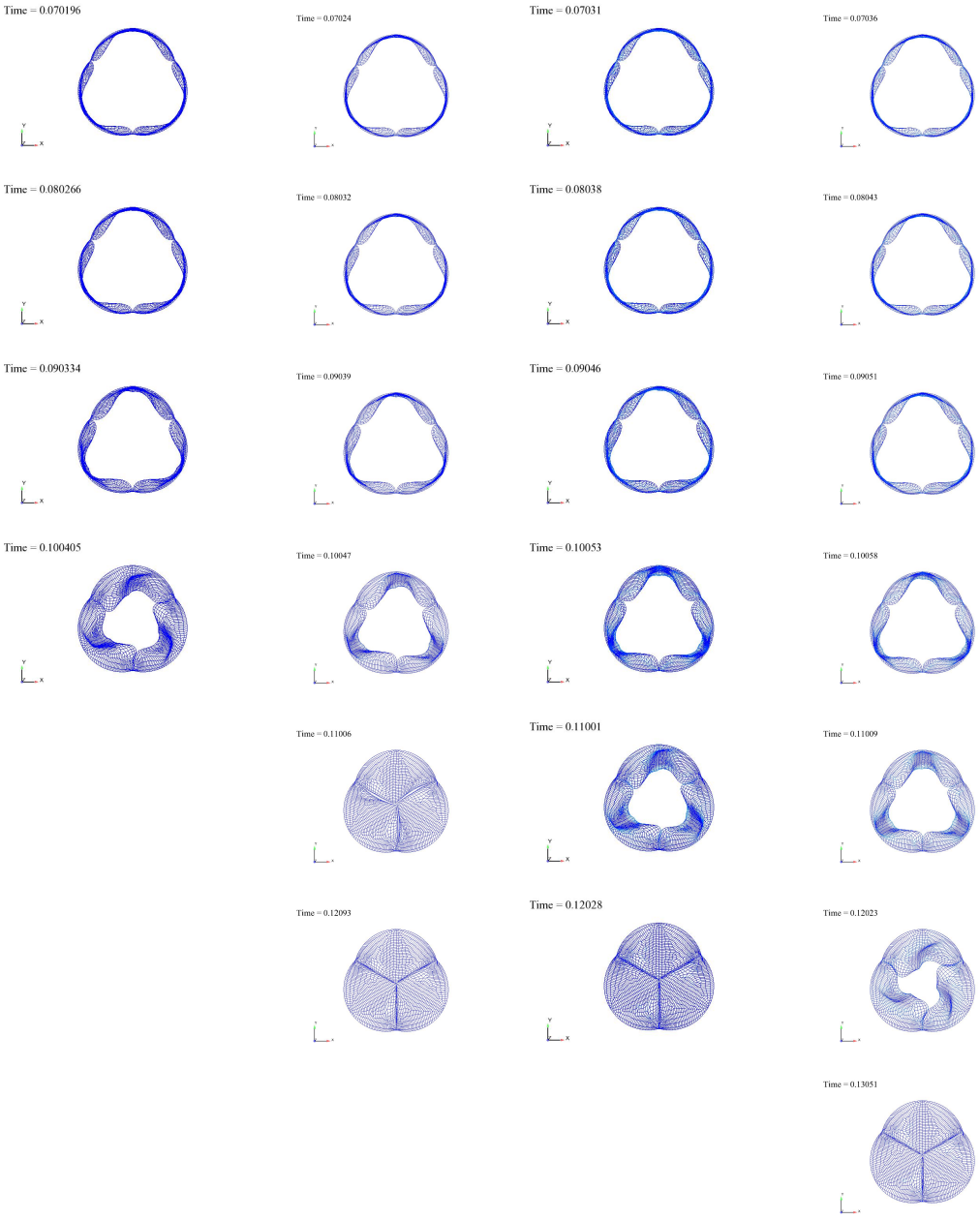

Figure C.7: Opening and closing behaviour after damping

It can be concluded that damping, even when used in low quantities, does have an effect on valve behaviour. If damping is required, it would be advisable to use the lowest factor that keeps the leaflets from oscillating.

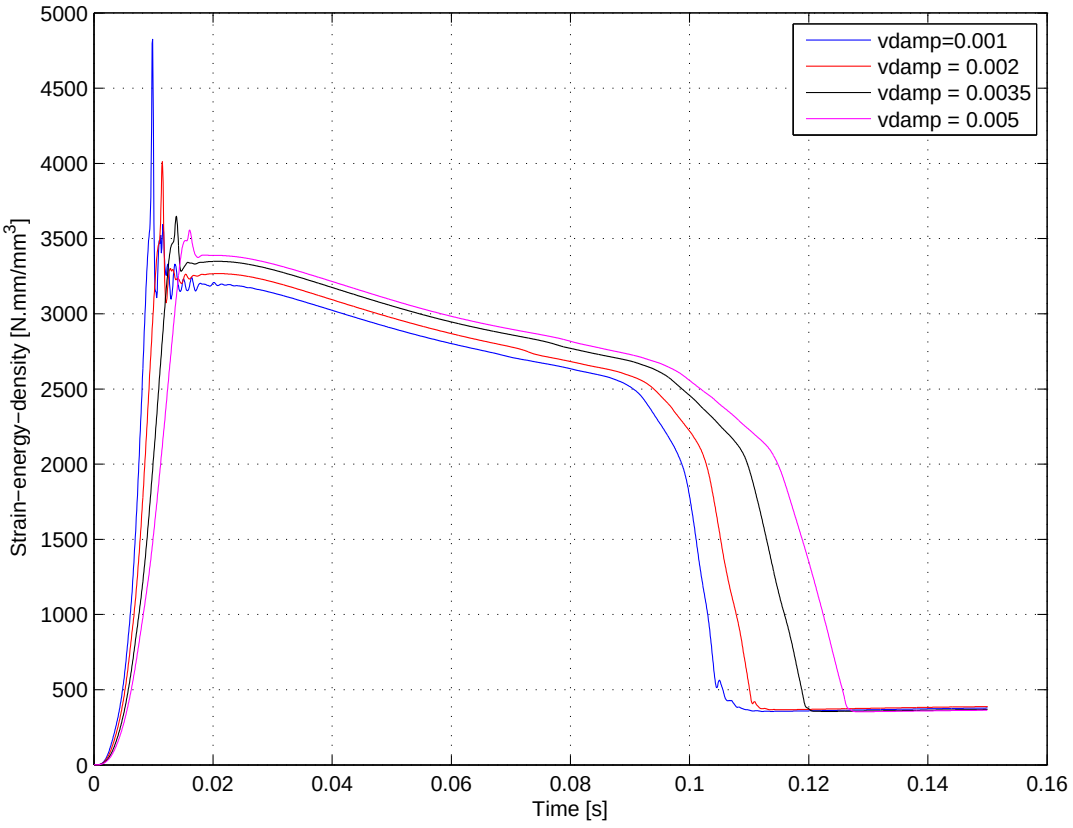

Figure C.8: Strain energy density vs. time

Appendix D

Leaflet stiffness and thickness

D.1 Introduction

Literature on aortic valves indicate many different leaflet material parameters, which led the author to further investigate the effect of material stiffness and thickness on leaflet functioning. Bernacca *et al.* [61] studied the influence of Young's modulus and leaflet thickness on the hydrodynamic behaviour of polyurethane valves. It was found that over a wide range of moduli, the hydrodynamic function is not affected significantly. Valves with higher moduli undergo less strain which increases their life span. Bernacca *et al.* [62, 63] showed that calcification will most likely occur at areas where high stress is present. These are the areas where leaflet failure is most likely to happen.

During this study the hydrodynamic performance, leaflet strain and resistance to opening was investigated. The same valve was used, but with different leaflet material properties. In order to calculate resistance or pressure drop over the valves, an FSI simulation with a velocity inlet boundary and a static pressure outlet boundary was used. These boundary conditions are of no use when simulating a full cardiac cycle, as zero velocity is reached at valve closure, therefore no further input will be present to complete the cycle. An inlet and outlet boundary pressure is thus essential for a full cardiac cycle simulation. Because of the amount of time required for a fluid structure analysis, the second simulations with the pressure boundaries were all "structure" only simulations.

Initially the valve was simulated for a thickness of 0.2, 0.35 and 0.5 mm and a Young's modulus of 2, 5 and 8 MPa. With the additional two boundary

conditions a total of 18 cases were simulated. Outputs of significance for the pressure boundary case were strain, opening and closing behaviour, whereas pressure drop over the valve was the output of interest for the velocity boundary condition.

D.2 FSI simulation parameters

For the FSI analysis the same valve was simulated with the only difference between simulations being the Young's Modulus and thickness of the material. The valve geometry can be seen in Figure D.1. The simulations were transient dynamic and the velocity inlet boundary condition is illustrated by Figure D.2. The outlet boundary condition was set to 0 Pa.

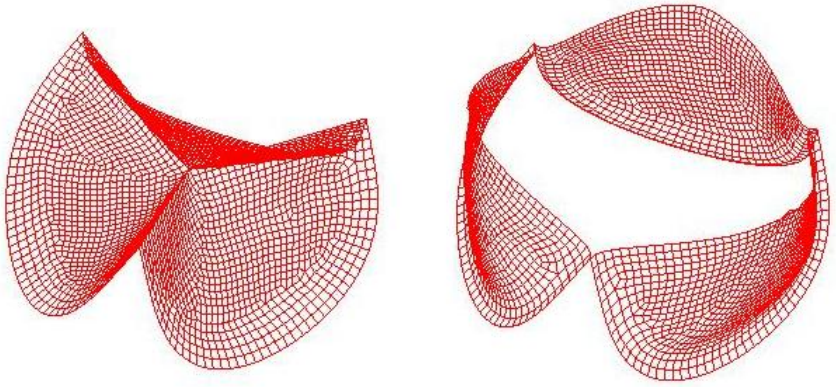

Figure D.1: Valve used in FSI analysis

D.3 Dry simulation parameters

As with the FSI analysis, the same valve was simulated every time with the only difference between simulations being the Young's modulus and thickness of the material. The valve geometry can be seen in Figure D.3. The simulations were transient dynamic and the differential pressure from the two curves in Figure D.4 was applied directly to the nodes on the leaflets.

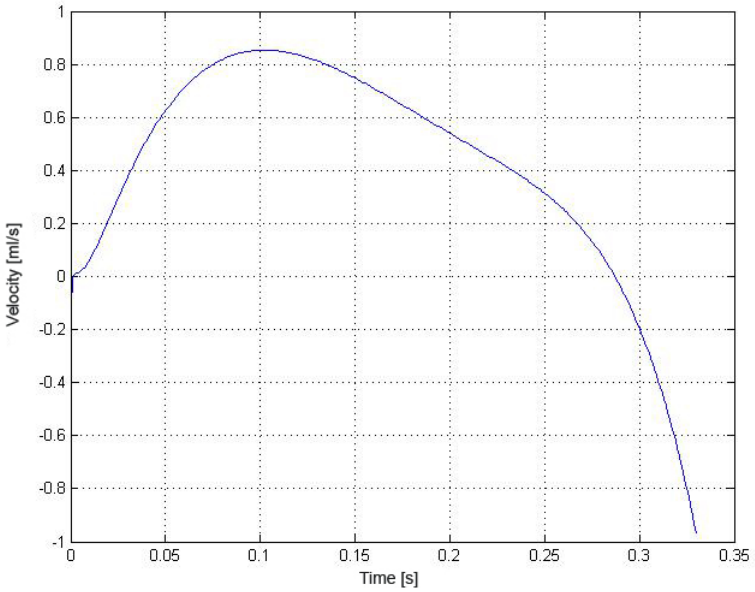

Figure D.2: Velocity input curve

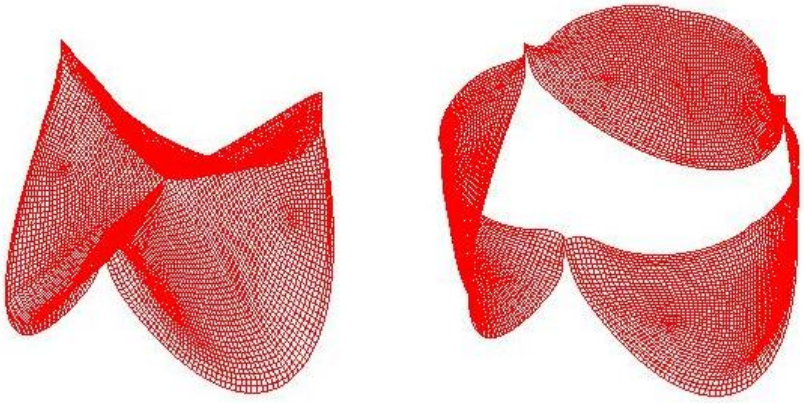

Figure D.3: Valve used in dry analysis

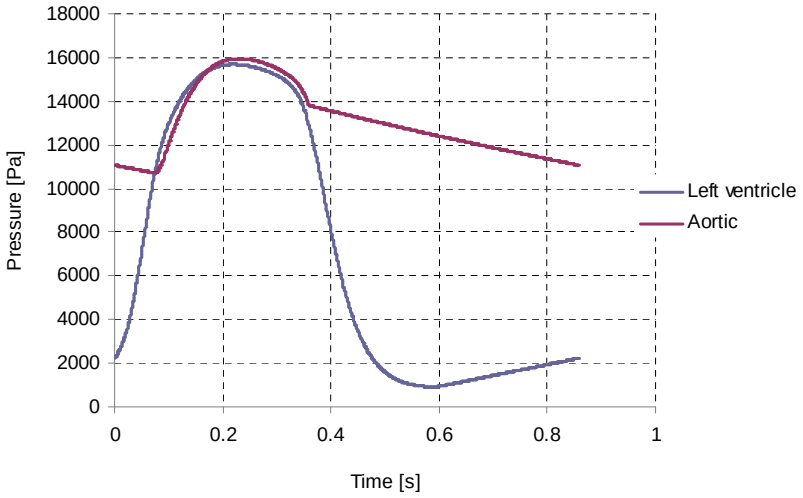

Figure D.4: Pressure input curve

D.4 Results

Figure D.5 shows the result from the FSI analysis with t2E2 corresponding to 0.2 mm thickness and $E = 2$ MPa, t2E5 corresponding to 0.2 mm thickness and $E = 5$ MPa, etc. The figures illustrate the maximum pressure drop over the valve during systole. This can also be seen as the pressure required to completely open the valves. The graph clearly illustrates that although stiffness has a notable influence on resistance it is not as significant as the leaflet thickness. These results are concurrent with the results found by Bernacca *et al.* [61] who tested polyurethane valves in-vitro.

The leaflet stiffness will actually play an even smaller role in-vitro than found in the simulations. The material was modelled as isotropic with a linear stress-strain relationship, thus a constant Young's modulus. The actual material used for the leaflets behave non-linear (as discussed in Appendix F) and the stress-strain graph initially have a small gradient, increasing exponentially with an increase in strain. Thus, during systole when the leaflets experience a low strain, the resultant leaflet's stiffness will be equally low.

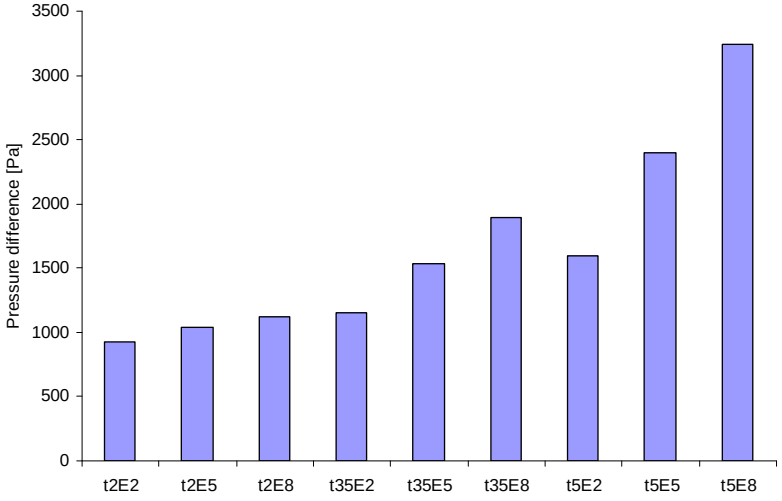

Figure D.5: Maximum valve resistance

Figures D.6 and D.7 show the maximum stress and strain respectively experienced by the valve during diastole. It can be observed that the Young's modulus has a significant effect on strain and is equally important as thickness to reduce strain during diastole.

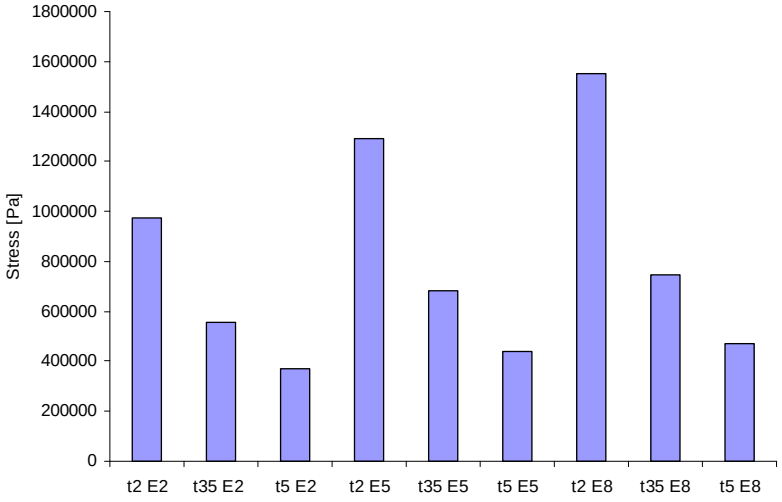

Figure D.6: Maximum von Mises stress

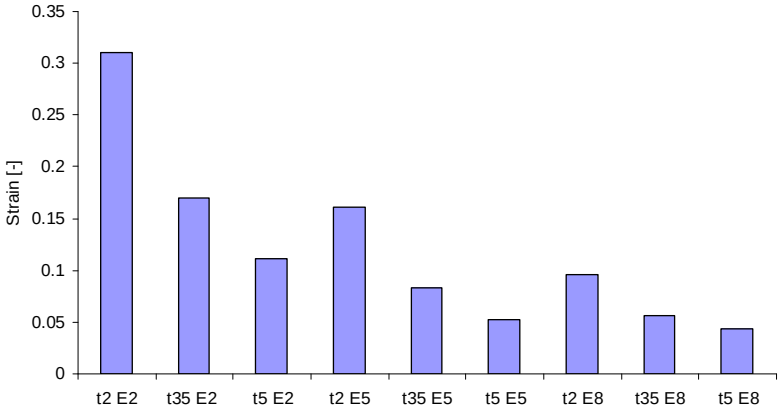

Figure D.7: Maximum shear strain

D.5 Conclusion

The main objective of this section was not to do an in depth analysis, but rather to evaluate the effect of leaflet stiffness and thickness on valve performance. Results clearly show that leaflet thickness has a significant effect on valve performance during the systolic phase, much more so than Young's modulus.

When evaluating the stress-strain relationship, results however indicate that the Young's modulus is equally effective as thickness in reducing strain during diastole.

Taking the above-mentioned results into consideration it is concluded that the ideal leaflet material should have a small thickness and high Young's modulus. Such a material will allow the leaflet to open and close easily during the systolic phase but it will also help in reducing the strain during the diastolic phase. Therefore the ideal leaflet material will have a non-linear behaviour, were a low strain will have a low stress as result. A higher strain will result in a much higher stress.

The author acknowledges the fact that non-linear material behaviour was not analysed, but it is suspected that non-linear material behaviour will increase valve performance as the native aortic leaflet material behaves non-linearly.

Appendix E

In-vitro results

E.1 Visualisation

Figure E.1 illustrates the image results for three of the valves from Chapter 9. The images are for 39 ms intervals. Unfortunately it was not possible to mount the St. Jude valve in such a manner that images could be taken.

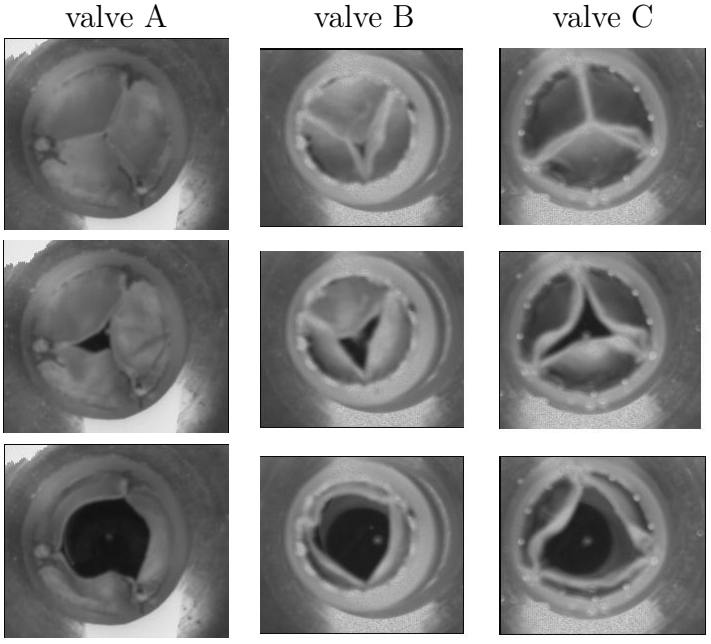

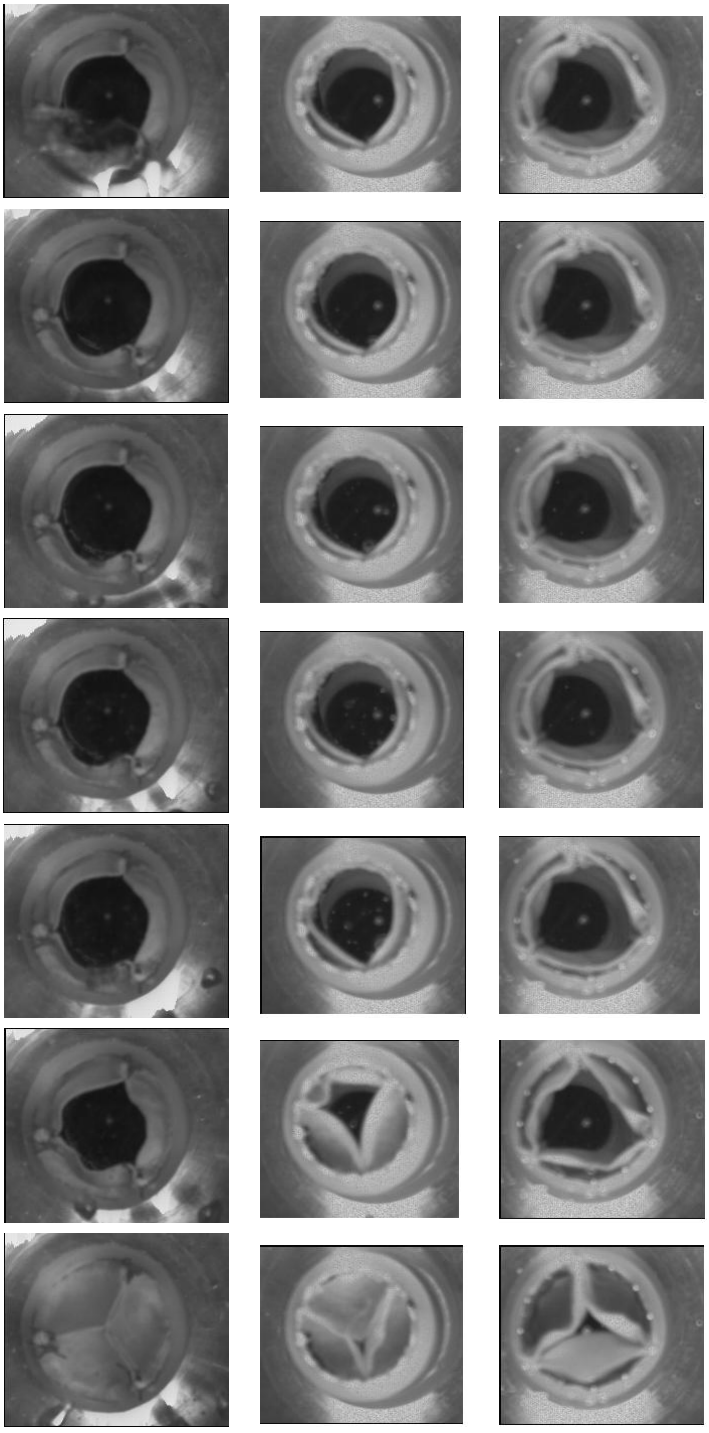

Figure E.1: Visualisation of in-vitro valve tests

E.2 Pressure and flow characteristics

The flow and pressure curves of valves A, B, C and D from Chapter 9 are shown in Figures E.2 through E.5.

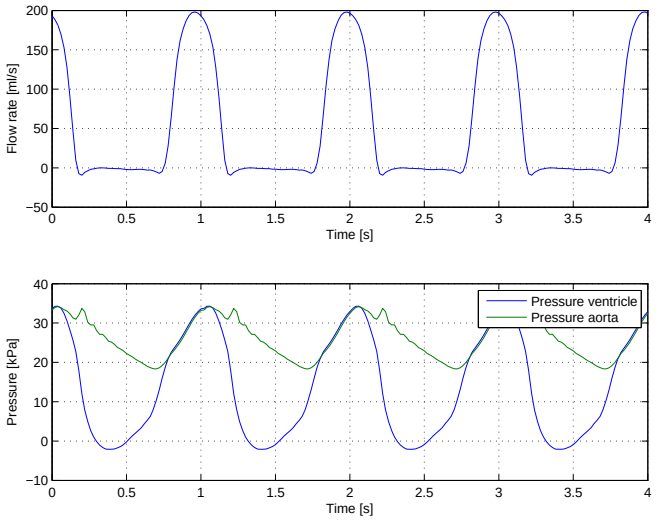

Figure E.2: Pressure and flow characteristics: valve A

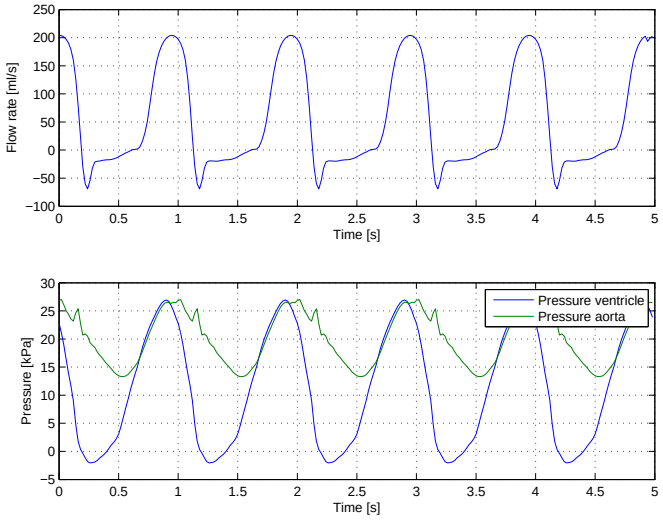

Figure E.3: Pressure and flow characteristics: valve B

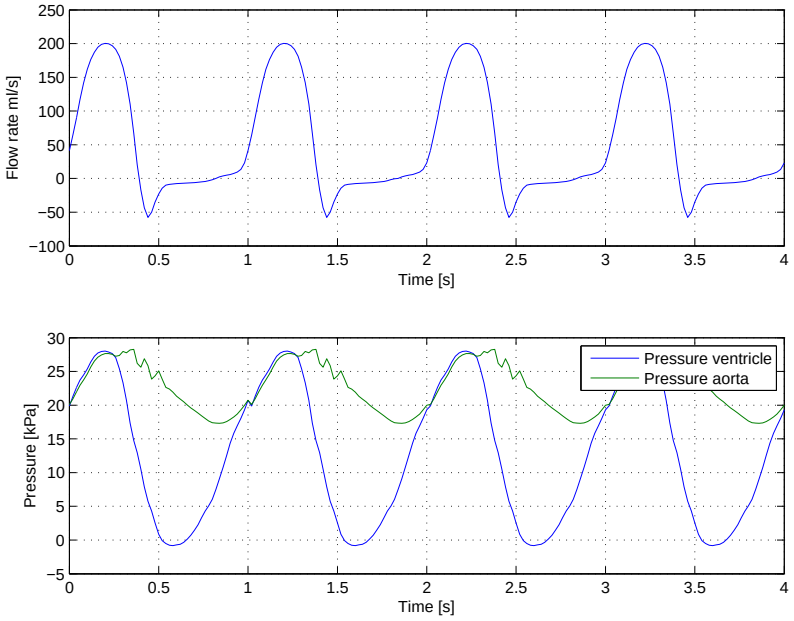

Figure E.4: Pressure and flow characteristics: valve C

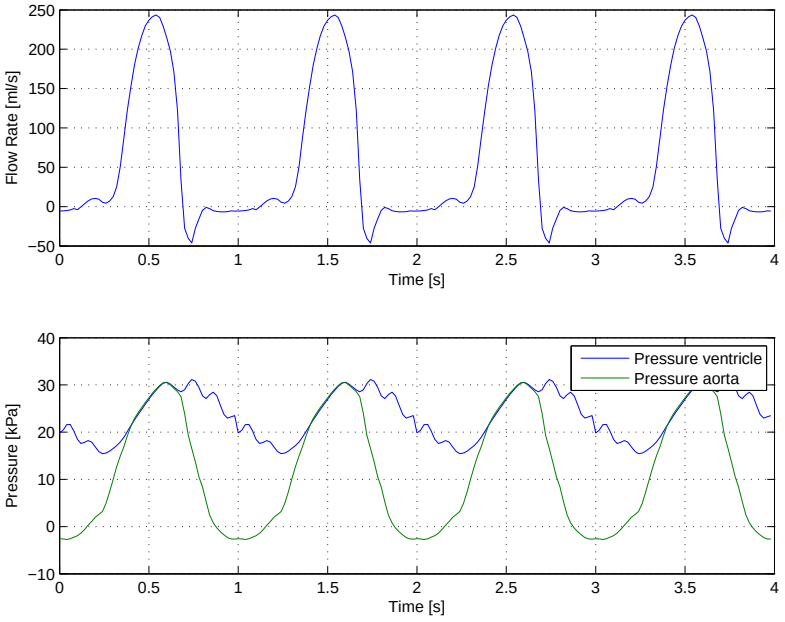

Figure E.5: Pressure and flow characteristics: valve D

Appendix F

Material sensitivity

F.1 Introduction

The materials used for the leaflets in the prototypes are from Bovine and Kangaroo Pericardium. At the time of the in-vitro tests (presented in Chapter 9), a material model for the Kangaroo pericardium was not yet available. A material model for the Bovine pericardium was however created by means of material tests, but MSC.Dytran software did not support the model.

During systole the leaflets offers very little resistance to flow and do not undergo nearly as much strain as during diastole. Therefore it was thought that because of the low strain, systolic movement of the leaflets could be simulated accurately with more than one material model. The goal of this study was to find alternative material models which would still facilitate accurate FSI simulation.

F.2 Material properties

The Bovine pericardium has a non-linear orthotropic behaviour as shown in Figure F.1 as the $X11$ and $X22$ curves. $X11$ and $X22$ are the stress-strain relationship in the circumferential (fibre) and axial (matrix) directions respectively.

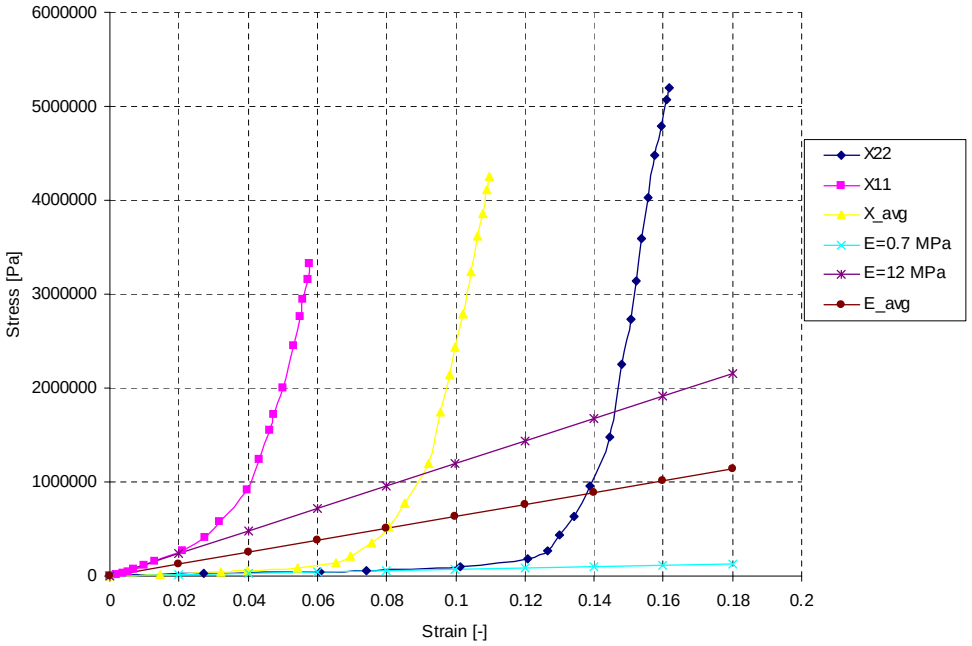

Figure F.1: Stress-strain curves

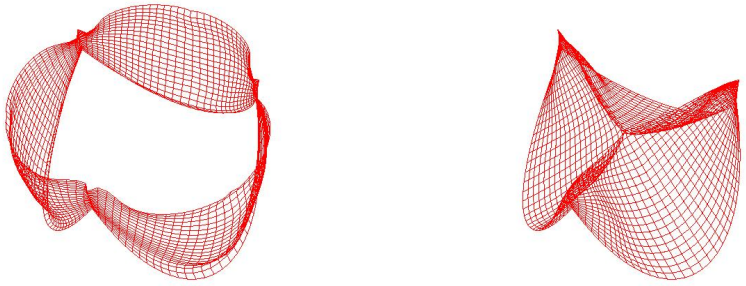

Figure F.2: Orthotropic shell orientation

F.3 Simulation

To perform simulations, the valve shown by Figure F.2 was created. The iso shell orientation in the leaflets allow for an orthotropic simulation. In other words the coordinate systems for all the shells on a leaflet allow for easy definition that would allow the shell local coordinate systems to lie in the same direction. With a paver mesh configuration this would be difficult.

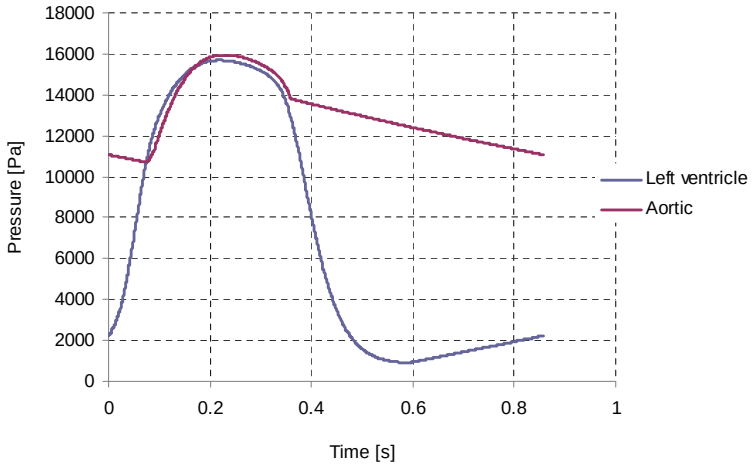

Figure F.3: Pressure vs. time

Setting up the coordinates as explained above allows for easier definition of the orthotropic directions. Figure F.3 shows the boundary pressure that was used in the simulations.

Linear isotropic

Three isotropic models where considered. The first model's E value is derived from the gradient of the non-linear $X11$ curve in Figure F.1:

$$E_1 = \frac{\sigma_x}{\epsilon_x} = 12MPa \tag{F.1}$$

The second model's E value is derived from the gradient of the $X22$ curve in Figure F.1:

$$E_2 = \frac{\sigma_y}{\epsilon_y} = 0.7MPa \tag{F.2}$$

Both these models use the "flatter" part of the non-linear curves. In these regions the strains are still low and this will also be the region where the leaflet operates during systole. The third isotropic model is the average between the first two models with a $E = E_{avg}$ value of 6.35 MPa.

Non-linear isotropic

Three non-linear isotropic models were used. The first model used the $X11(E_x)$ curve, the second model used the $X22(E_y)$ curve and the third model is an average between the two. These non-linear models were inserted into Dytran as true stress-strain relationships.

Linear orthotropic

Only one linear orthotropic model was created. The circumferential direction has an E_x value of 12 MPa which is the same as the first isotropic model. The axial direction has an E_y value of 0.7 MPa, which is the same as the second isotropic model. Because the material is incompressible a uniform Poisson's ratio is used:

$$\nu_{xy} = \nu_{yz} = 0.45 \tag{F.3}$$

As E_x is much greater than E_y the in-plane shear modulus can be derived [28]:

$$G_{xy} = \frac{E_y}{2(1 + \nu_{xy})} = 241kPa \tag{F.4}$$

F.4 Results

From the opening and closing visual results, three material models were eliminated because their leaflets were too stiff, preventing the valves from fully opening.

Figures F.4 - F.7 shows the maximum strain distribution in the leaflets during systole. The orthotropic leaflets show a slightly different distribution than the other valves.

Figure F.8 demonstrates the opening and closing behaviour of the valves for the different material models. The behaviour is summarized in Table F.1. The RVOT, RVCT and ET times for the isotropic valves are very similar, but differs from the orthotropic valve. The strain in the last column is almost identical for all the models.

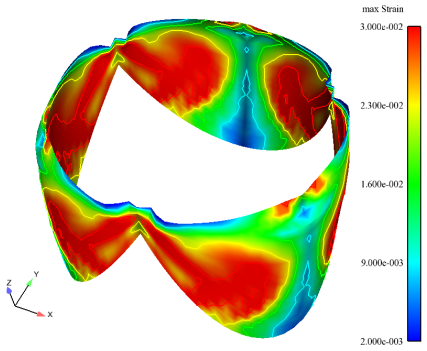

Figure F.4: Linear orthotropic

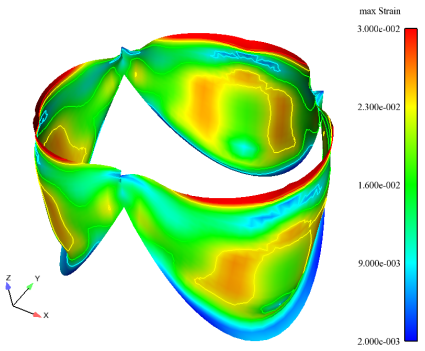

Figure F.5: Linear isotropic E = 0.7 MPa

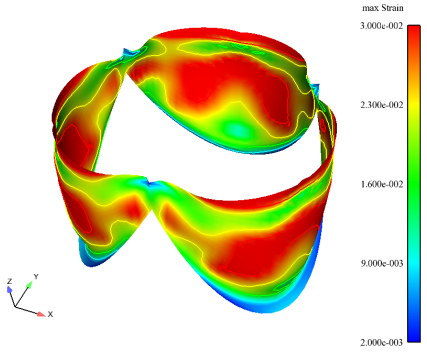

Figure F.6: Non-linear isotropic E_{22}

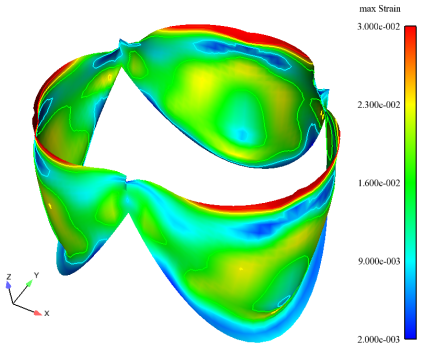

Figure F.7: Non-linear isotropic E_{avg}

Table F.1: Opening and closing characteristics

Material	Open	RVOT [ms]	RVCT [ms]	ET [ms]	Strain [-]
Lin Ortho	Yes	28.5	86	185	0.033
Lin iso (E = 0.7 MPa)	Yes	14.3	43	104	0.037
Lin iso (E = 12 MPa)	No	-	-	-	-
Lin iso (E_{avg})	No	-	-	-	-
Non-lin Iso (E_{11})	No	-	-	-	-
Non-lin Iso (E_{22})	Yes	15.2	54	108	0.034
Non-lin Iso (E_{avg})	Yes	17.8	61	104	0.024

Lin ortho	Lin iso ($E = 0.7$ MPa)	Non-lin iso (E_{22})	Non-lin iso (E_{avg})
Time = 0.000000	Time = 0.0000	Time = 0.00000	Time = 0.0000
Time = 0.010410	Time = 0.0109	Time = 0.00999	Time = 0.0099
Time = 0.020232	Time = 0.0220	Time = 0.02010	Time = 0.0198
Time = 0.030120	Time = 0.0304	Time = 0.03027	Time = 0.0298
Time = 0.070468	Time = 0.0716	Time = 0.06999	Time = 0.0694
Time = 0.080072	Time = 0.0825	Time = 0.08075	Time = 0.0793
Time = 0.090265	Time = 0.0906	Time = 0.08930	Time = 0.0911
Time = 0.100449	Time = 0.1014	Time = 0.10198	Time = 0.1009
Time = 0.109871		Time = 0.00000	Time = 0.0000

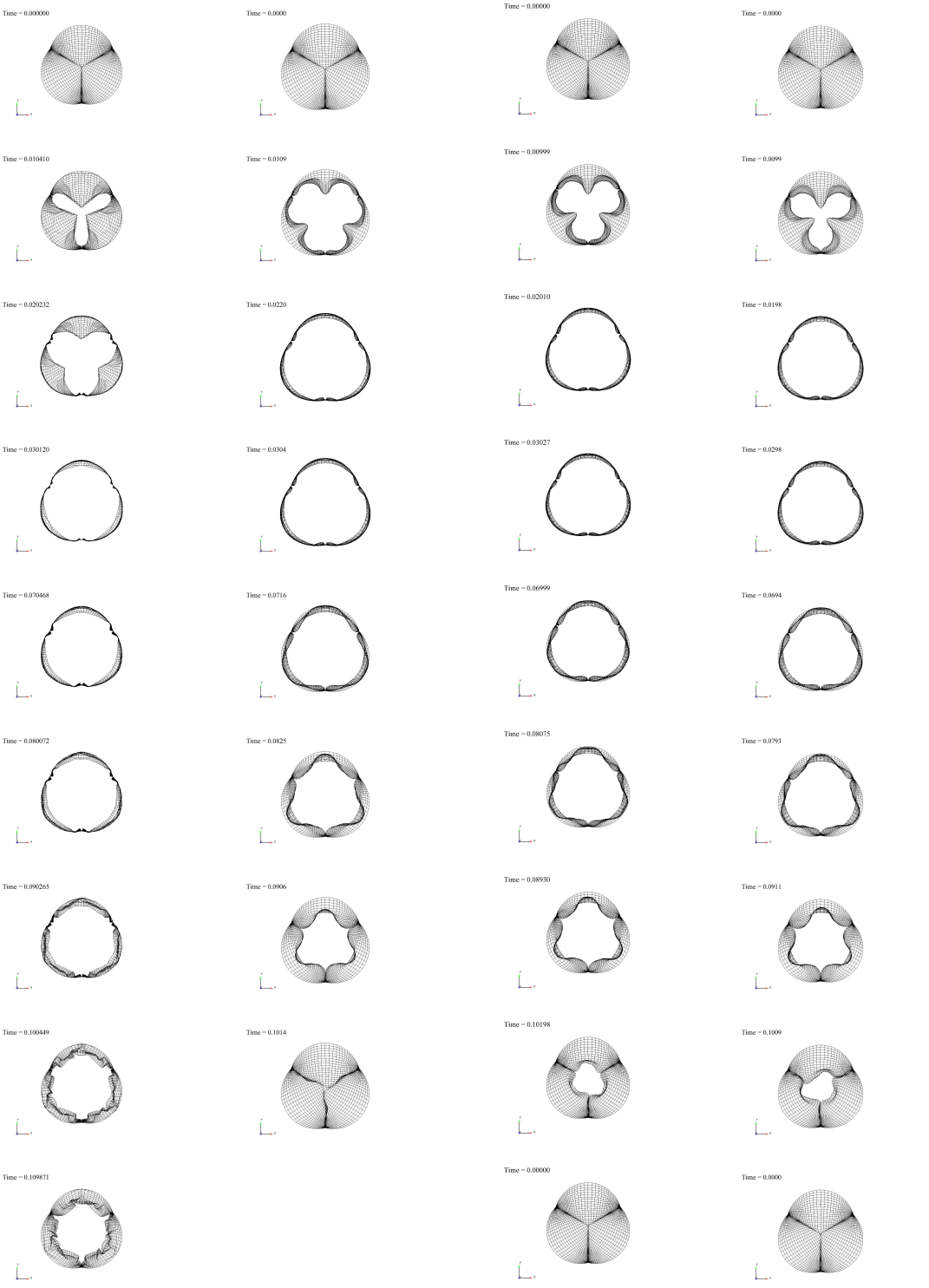

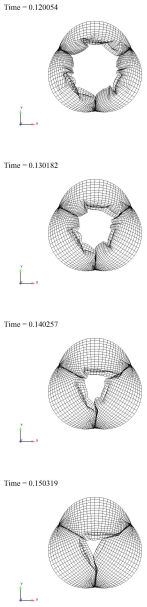

Figure F.8: Opening and closing behaviour

F.5 Conclusion

All the simulations showed similar strain results. This suggests that there is not a significant difference between using a linear isotropic, a non-linear isotropic or a orthotropic material model to simulate the systolic part. This is because the leaflets endure very little strain. The orthotropic model took a little longer to open and close, probably because of the high stiffness in the $X11$ direction.

For comparison of the FSI simulations to in-vitro tests, the linear orthotropic material model would probably be the best approximation, but not necessarily the easiest to implement. The non-linear isotropic model with the E value the same as the $X22$ or matrix direction, would probably be the second best approximation.

Appendix G

Sensor calibration

G.1 Pressure sensor

The specifications for the pressure sensors used in the pulse duplicator are shown in Table G.1. The pressure range for the sensors is 5 psi. This is a relatively low pressure, therefore the sensors were calibrated by measuring the water head in a 3 m vertical column. The column was divided into 15 cm intervals, after which it was filled with water. The voltage output from the sensors was recorded. The actual pressure was calculated with Equation G.1 where $\rho = 1000$ kg/m^3 is water density, $g = 9.81$ m/s^2 is gravitation, h is the head in m and P is the calculated pressure in Pa.

$$P = \rho g h \tag{G.1}$$

The calibration curves for the pressure sensors can be seen in Figure G.1.

Table G.1: Pressure sensor specification

Type	Piezo electric gage pressure sensors
Manufacturer	Honeywell
Model number	26PCBFA1G
Exitation [VDC]	10
Linearity [% Span]	±0.25
Repeatability & hysteresis [% Span]	±0.15
Response time [msec]	1.0
Sensitivity [mV/PSI]	23
Maximum span [mV]	115

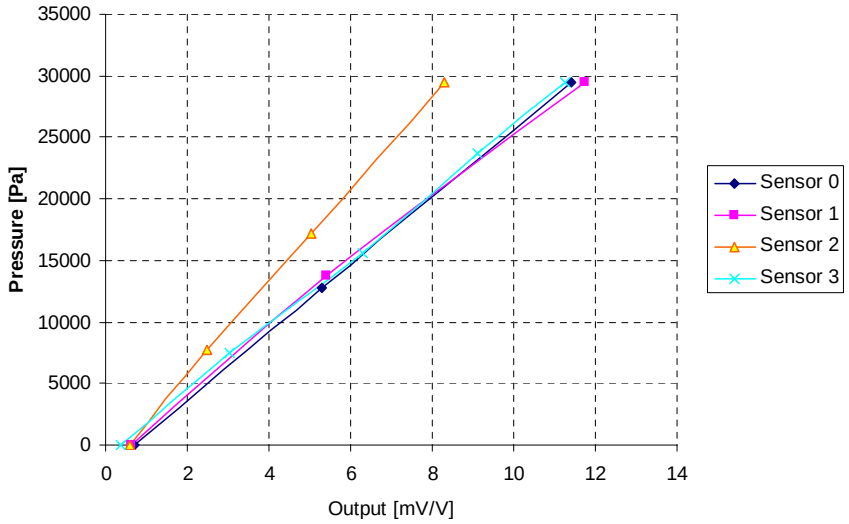

Figure G.1: Pressure sensor calibration curves

G.2 Orifice plate

A diagram of the orifice plate can be seen in Figure G.2 with *Di* and *Do* 18 mm and 8 mm respectively. Equal distance corner taps were used. A pressure vs. flow curve was constructed by simultaneously measuring the differential pressure across the orifice plate and the flow rate. The calibration setup consisted of a water pump with adjustable flow rate, two mercury manometers to measure the pressure at the taps of the orifice plate and a measurement jug to measure water volume. The pump output was changed and the flow rate calculated by measuring the volume of water for a certain time. Figure G.3 shows the calibration curve obtained from the setup that was used to calculate the flow in the pulse duplicator. Although the curve was constructed up to a maximum flow rate of 500 ml/s, the figures obtained from the pulse duplicator (see Appendix E) showed that the maximum flow over the valve never exceeded 200 ml/s for the testing. A flow of 200 ml/s gives a Reynolds number of 12600 for a 20 mm diameter valve and water as test fluid. This definitely suggests turbulent flow but as explained in Chapter 2.3 and as shown in Appendix A a laminar model is sufficient for the FSI simulations.

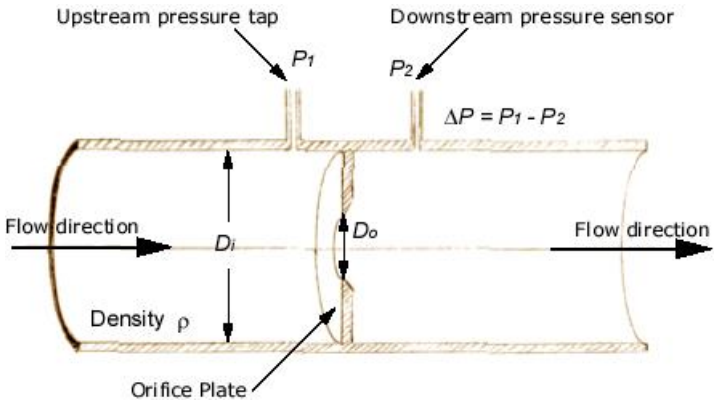

Figure G.2: Orifice plate [64]

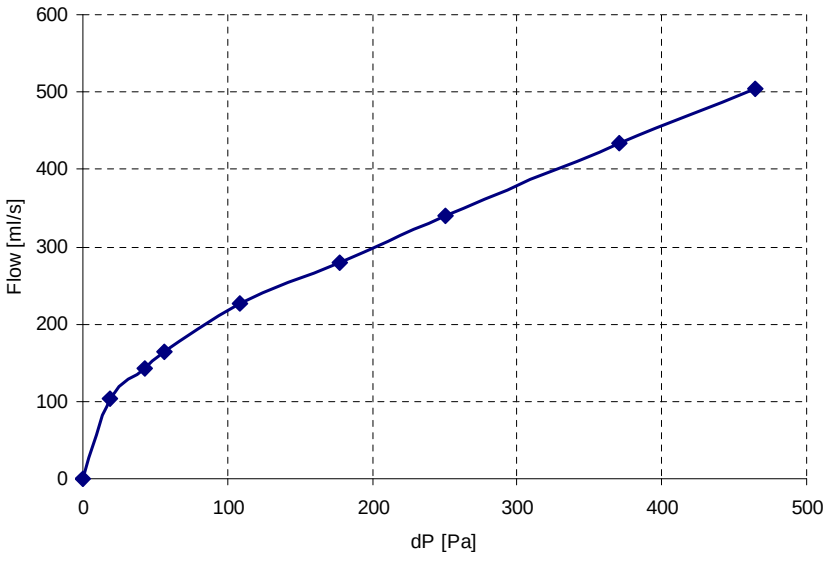

Figure G.3: Calibration curve: orifice plate